



저작자표시-비영리-변경금지 2.0 대한민국

이용자는 아래의 조건을 따르는 경우에 한하여 자유롭게

- 이 저작물을 복제, 배포, 전송, 전시, 공연 및 방송할 수 있습니다.

다음과 같은 조건을 따라야 합니다:



저작자표시. 귀하는 원저작자를 표시하여야 합니다.



비영리. 귀하는 이 저작물을 영리 목적으로 이용할 수 없습니다.



변경금지. 귀하는 이 저작물을 개작, 변형 또는 가공할 수 없습니다.

- 귀하는, 이 저작물의 재이용이나 배포의 경우, 이 저작물에 적용된 이용허락조건을 명확하게 나타내어야 합니다.
- 저작권자로부터 별도의 허가를 받으면 이러한 조건들은 적용되지 않습니다.

저작권법에 따른 이용자의 권리는 위의 내용에 의하여 영향을 받지 않습니다.

이것은 [이용허락규약\(Legal Code\)](#)을 이해하기 쉽게 요약한 것입니다.

[Disclaimer](#)

Synthesis of Cathode and Anode Materials via Top-Down Approach for Li-ion Batteries

Sookyung Jeong

Department of Energy Engineering
(Battery Science and Technology)

Graduate School of UNIST

2014

Synthesis of Cathode and Anode Materials via Top-Down Approach for Li-ion Batteries

Sookyung Jeong

Department of Energy Engineering
(Battery Science and Technology)

Graduate School of UNIST

Synthesis of Cathode and Anode Materials via Top-Down Approach for Li-ion Batteries

A thesis/dissertation

submitted to the Graduate School of UNIST

in partial fulfillment of the

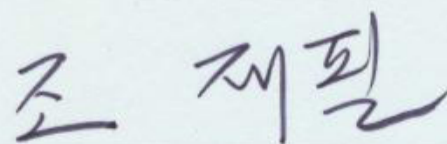
requirements for the degree of

Doctor of Philosophy of Science

Sookyung Jeong

June 20th 2014

Approved by



Advisor

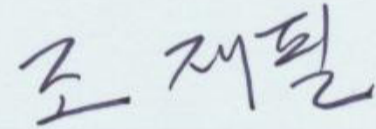
Professor Jaephil Cho

Synthesis of Cathode and Anode Materials via Top-Down Approach for Li-ion Batteries

Sookyung Jeong

This certifies that the thesis/dissertation of Sookyung Jeong is approved.

June 20th 2014



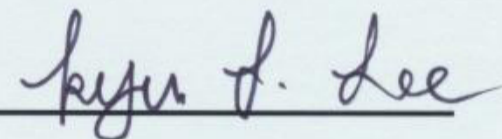
Thesis Advisor:

Prof. Jaephil Cho



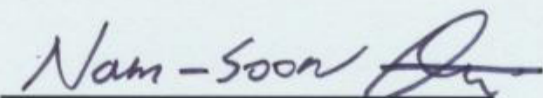
Committee Member:

Prof. Soojin Park

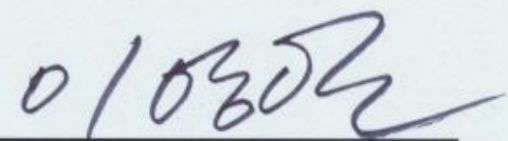


Committee Member:

Prof. Kyu-Tae Lee



Committee Member: Prof. Nam-Soon Choi



Committee Member:

Prof. Youngil Lee

Abstract

Creating green energy solutions has become crucial to society. However, to achieve a clean and renewable energy system, significant developments must be made not only in energy conversion technologies (such as solar panels and wind turbines), but also in the feasibility and capabilities of stationary, electric-energy storage (EES). Many types of EES systems have been considered such as pumped hydroelectric storage, compressed air energy storage (CAES), flywheels, and electrochemical storage. Among them, electrochemical storage such as batteries has the advantage of being more efficient compared to other candidates because it is more suitable in scalability, efficiency, lifetime, discharge time, weight, and/or mobility of the system. Currently, lithium (Li)-ion rechargeable batteries have become very important in recent years due to their great promise as power source, but the batteries are limited by their materials' performance. Accordingly, the development of high performance materials has been main focus in materials science research. Here, the achievements of cathode, anode, and current collector are described that they are synthesized via top-down approach to enhance their performance in Li-ion batteries.

In cathode research, in spite of that there have been many reports dealing with nanostructured cathode materials, none of previous works have been reported the morphology transition of cathode materials via chemical etching. In this study, we found that a selective chemical etching method using PVP and AgNO_3 is very promising for obtaining significantly improved electrochemical performance of the cathode materials even at high voltage range. This etching method spontaneously turns to layered morphology with a layer thickness of 10 nm. Furthermore, we found that the concurrent modification of layered LiCoO_2 with a nanoscale Co_3O_4 coating layer by chemical etching to minimize the capacity loss and to maximize the rate capability of the cathode without the loss of the electrode density.

In anode research, a novel architecture consisting of Si nanowires internally grown from pores in the etched graphite with high electrode density of 1.5 g/cm^3 is introduced. In previous works, various nano-engineering concepts were introduced to overcome a volume related problem of Si during cycling. However, although these strategies exhibited a superior performance such as high capacity and good cycling stability, they cannot be satisfied with electrode density which is highly required to determine high energy density in practical approach. In this point of view, this work provides new strategy to design electrode material with practically required electrode density and high volumetric capacity. Simply, porous graphite as template for Si nanowires growth is designed via hydrogenation and Si nanowires are internally grown from pores in etched graphite via Vapor-Liquid-Solid process. Especially, porous graphite, which first is reported as top-down approach, plays a key role of good electrochemical performance in this work. In this system, not only porous graphite can offer free space

to accommodate the volume change of Si nanowires, but also efficiently improve the electron transport between active materials.

In current collector research, more advanced nanostructure anodes of uniform 3D Cu-Si core shell structured arrays with 250 and 500 nm diameter are produced using top-down processes. This nanostructured anodes improved in cycle stability and rate performance, even at 20 C rate. As a current collector, each Cu nanopillar substrate provides a high surface area for better mass accommodation of Si deposition while the space between them enhances the electrochemical reaction between the electrode and electrolyte and accommodates the volume change during cycling. In addition, because the fabrication of the Cu nanopillar substrate only involves conventional top-down processes, the nanopillars can be generated through a facile and fast process with control of the surface area and simple modulation of the nanopillar density or diameter. Remarkably, the well-patterned nanopillar substrate imparts a significantly enhanced connection between the current collector and active materials without a binder, and also provides free space to accommodate Si expansion without pulverization during cycling.

As an additional part, owing to an introduction of devices that required a flexible energy storage, Li-ion batteries (LIBs) as a leading candidate have been widely considered due to high electrochemical performance. To approach a flexible property in LIBs, the system has highly required an electrode with flexible characteristic, therefore, graphene based composites has been strongly attractive due to the large surface area and electron transport with high mechanical strength. Also, as another field in anode material, vanadium sulfides (VS_4) have been paid much attention due to high specific capacity and rate capability of lithium storage in these days. Accordingly, the composite consisting of grapheme and VS_4 is synthesized and characterized to describe the mechanism for lithium storage and high electrochemical performance in LIBs.

Contents

Contents	i
List of Figures	iv
List of Tables	x
Nomenclature	xi
Chapter I. Stationary Electric Energy Storage – Battery	1
1. Introduction: The need of electric energy storage system	1
2. Battery for EES applications	3
2.1. Lead-acid battery	3
2.2. Na-S battery	5
2.3. Li-ion battery	6
2.4. Redox flow battery: All-vanadium	7
3. Recent progress in battery for EES applications	9
3.1. Metal-Air battery: Zn-Air	9
3.2. Advanced redox flow battery	12
3.3. Aqueous lithium flow battery	14
3.4. Waste-Li-liquid flow battery	16
4. Conclusion	17
Chapter II. The Details in Li-ion Batteries	45
1. Li-ion Batteries' trend in 2014	45
1.1. Electric vehicles	45
1.2. Energy storage system	47

2.	Materials in Li-ion batteries	48
2.1.	Cathode	49
2.2.	Anode	49
2.3.	Separator	50
2.4.	Electrolyte	51
2.5.	Current collector	51
3.	The properties changes at high temperature and voltage in LIB	51

Chapter III. High-Performance, Layered, 3D-LiCoO₂ Cathodes with a Nanoscale Co₃O₄ Coating via Chemical Etching

1.	Introduction	71
2.	Experimental section	72
2.1.	The layered 3D-LiCoO ₂ preparation	72
2.2.	Analysis instrument	72
2.3.	Coin-cell preparation	72
3.	Results and discussion	73
4.	Conclusion	75

Chapter IV. Etched Graphite with Internally Grown Si Nanowires from Pores as an Anode for High Density Li-Ion Batteries

1.	Introduction	87
2.	Experimental section	88
2.1.	The preparation of Si nanowires embedded in porous graphite	88
2.2.	Fabrication of lithium ion half-cell	88
3.	Results and discussion	89
4.	Conclusion	92

Chapter V. 3D Amorphous Silicon on Nanopillar Copper Electrodes as Anodes for High-Rate Lithium-Ion Batteries	115
1. Introduction	115
2. Experimental section	116
2.1. Fabrication of <i>a</i> -Si/3D-Cu electrode	116
2.2. Fabrication of the Li-ion half-cell	116
2.3. Electrochemical characterization of the half-cell	117
2.4. Morphology characterization of the <i>a</i> -Si/3D-Cu nanopillar electrode	117
3. Results and discussion	117
4. Conclusion	119
Chapter VI. Lithium reaction mechanism and high rate capability of VS₄-graphene nanocomposite as an anode material for lithium batteries	136
1. Introduction	136
2. Experimental section	137
2.1. Synthesis of VS ₄ -rGO composites	137
2.2. Characterization of the materials	137
2.3. Electrochemical characterization of the materials	137
3. Results and discussion	138
4. Conclusion	142
Acknowledgment	161

List of Figures

Chapter I. Stationary Electric Energy Storage – Battery

Figure 1. The description of load leveling with the adoption of electric energy storage system	19
Figure 2. Classification of electrical energy storage for large scale stationary applications	20
Figure 3. (a) Configuration of lead-acid battery, and (b) Graphical representation of discharge-charge reaction mechanism	23
Figure 4. Schematic view of the ultra-battery consisting of lead-acid cell and asymmetric supercapacitor	24
Figure 5. Schematic illustration of tubular Na-S battery with the detailed structure	25
Figure 6. The schematic view of Li-ion battery consisting of intercalation compounds during discharge	26
Figure 7. Schematic view of all vanadium redox flow battery during discharge	27
Figure 8. The comparison of theoretical specific energy density of electrochemical energy storage system	28
Figure 9. The general description of metal-air battery system with oxygen reduction reaction phase ...	29
Figure 10. The detailed illustration of zinc-air battery	30
Figure 11. The configuration of aqueous lithium flow battery and the electrochemical reaction process	31
Figure 12. Various candidates of cathode in aqueous lithium flow battery	32
Figure 13. Schematic view of waste Li-liquid flow battery consisting of waste battery material, Li metal, and water	33
Figure 14. (a) Disassembled waste Li-ion battery, (b) Waste battery materials with Li_xC_6 , Li_xFePO_4 , and LiPF_6 in EC/DEC, (c) Charge voltage curve for Li metal harvest from liquid solution with waste materials, (d) Li metal on surface of stainless steel after harvest process of Li, and (e) The comparison of discharge curve between pure Li metal and harvested Li from waste Li-ion battery when using pure DI water as cathode	34

Chapter II. The Details in Li-ion Batteries

Figure 1. (a) The proportion of material cost in Lithium-ion batteries and (b) the scale of LIB material market	54
Figure 2. (a) The proportion of secondary batteries depending on applications, (b, c, and d) the application proportion of cylindrical, prismatic, and pouch type, respectively	56
Figure 3. The market trend of global lithium-ion batteries: shipments depending on a cell type	57
Figure 4. The perspective of NiMH and LIB market for HEV	61
Figure 5. The value-chain configuration between battery and vehicle makers	62
Figure 6. The market share of main companies producing (a) cathode, (b) anode, (c) electrolyte, and (d) separator in 2009	65

Chapter III. High-Performance, Layered, 3D-LiCoO₂ Cathodes with a Nanoscale Co₃O₄ Coating via Chemical Etching

Figure 1. Upper: Schematic view of preparation of the pristine to the layered 3D-LiCoO ₂ cathode material: 1) the loading Ag particle on the surface of PVP-coated LiCoO ₂ by reduction from Ag ⁺ ions, 2) the formation of potholes by chemical etching in HF solution. Lower: a) SEM image of bare LiCoO ₂ , b) SEM image of the layered 3D-LiCoO ₂ and c, d) TEM images of bare LiCoO ₂ and the as-etched LiCoO ₂ , respectively, after etching in HF solution for 1 h, followed by vacuum drying at 120 °C for overnight	76
Figure 2. Powdery X-ray diffraction patterns of a) the pristine, and b) the layered 3D-LiCoO ₂	77
Figure 3. O1s XPS spectra of a) Co ₃ O ₄ and b) the layered 3D-LiCoO ₂	78
Figure 4. Electrochemical evaluation of bare LiCoO ₂ (black) and the layered 3D-LiCoO ₂ (red). a) voltage profiles at 1 (square), 3 (triangle), 5 (circle) and 7 C (diamond) rate between 3 and 4.6 V in coin-type lithium half cells (2016R-type) (inset: average voltage at each C-rate), b) plot of discharging capacity vs. cycle number at a rate of 1 C (triangle: bare LiCoO ₂ , square: the layered 3D-LiCoO ₂)	79
Figure S1. The low magnification SEM images of a) bare LiCoO ₂ and b) as-etched 3D-LiCoO ₂	80
Figure S2. a) The etched LiCoO ₂ without the continuous Ag ⁰ alignment, b) the layered 3D-LiCoO ₂ with the continuous Ag ⁰ alignment	81
Figure S3. TEM image of as-etched LiCoO ₂ and fast-fourier transform (FFT) images of a, b, and c areas	82

Figure S4. The deconvolution of XPS spectrum of Co2p region of 2D-LiCoO₂83

Chapter IV. Etched Graphite with Internally Grown Si Nanowires from Pores as an Anode for High Density Li-Ion Batteries

Figure 1. Top: Schematic view for the synthesis process of Si nanowires internally grown in porous graphite. Bottom: SEM images of (a) bare graphite, (b) loaded polystyrene-b-poly(2-vinylpyridine) micelles bearing Ni ion on graphite surface, (c) porous graphite after hydrogenation at 1000 °C for 1h, and (d) Si nanowires grown from porous graphite after catalyst exchange from Ni to Au, followed by VLS process using SiH₄ at 550 ° C for 30 min (For low magnification images, see Figure S1)93

Figure 2. (a and b) XRD patterns (asterisks: Ni nanoparticles) and Raman spectra of bare graphite and porous graphite, respectively (black: bare graphite, red: porous graphite). (c and d) XRD pattern and XPS C1s spectra of SiNWs-PG. In the XPS analysis, the deconvoluted peaks at 284.1, 284.8, and 285.1 eV indicates Si-C, C in graphite, and C-H bonding, respectively94

Figure 3. (a) Voltage profiles of bare graphite, porous graphite, SiNWs-BG and SiNWs-PG at 0.05C rate and (b) plot of volumetric charge (delithiation) capacity as a function of cycle number and coulomb efficiency at 0.2C rate between 0.005 and 1.4V in coin-type half-cell at 24 °C (1C = 450 mAh/cm³ for bare graphite and porous graphite, 1C = 1050 mAh/cm³ for SiNWs-BG and SiNWs-PG) (c) Rate capability of SiNWs-BG and SiNWs-PG with increasing C rate from 0.1 to 5C rate between 0.005 and 1.4V in coin-type half-cell at 24 °C and (d) voltage profiles of (c) at each C rate (charge and discharge rates were same)95

Figure S1. Cross-sectioned SEM images of (a) bare MCMB and (b) etched MCMB, and low magnified SEM images of (c) bare graphite, (d) loaded polystyrene-b-poly(2-vinylpyridine) micelles bearing Ni ion on graphite surface, (e) porous graphite after hydrogenation at 1000 °C for 1h, and (f and g) Si nanowires grown from porous graphite after catalyst exchange from Ni to Au, followed by VLS process using SiH₄ at 550 °C for 30 min (g is expanded image of (f))96

Figure S2. SEM images of SiC nanowires on porous graphite by VLS process with silane decomposition at (a) 1200 °C, (b) 1300 °C, and (c) XRD pattern of (a) sample. The peak positions corresponding to graphite (green), SiC (pink) and Ni₂Si (blue) are shown97

Figure S3. (a and b) SEM images of Si nanowires from the pores in the controlled experiment with SiH₄ flow with 15 sccm at 550 °C for 30 min and (c) bright-field TEM image of Si nanowires grown in porous graphite. The dark region on the top of Si nanowires indicates the alloy catalyst after VLS

process. (c) highly magnified TEM image of the circled region in (b), and crystalline Si nanowire with an amorphous SiO₂ layer is shown98

Figure S4. (a and b) the low and high magnified SEM images of the directly Si nanowires grown on bare graphite without etching process at the same condition for Si nanowire growth (SiH₄ flow with 25 sccm at 550°C for 30 min)99

Figure S5. (a) Voltage profile of bare graphite, porous graphite, and SiNWs-PG at 0.05C rate, (b) plot of volumetric charge (delithiation) capacity as a function of cycle number and coulomb efficiency at 0.2C rate between 0.005 and 1.4V in coin-type half-cell at 24 °C (1C = 300 mA/g for bare graphite and porous graphite, 1C = 700 mAh/g for SiNWs-BG and SiNWs-PG), (c) Rate capability of SiNWs-BG (black) and SiNWs-PG (red) with increasing C rate from 0.1 to 5C rate between 0.005 and 1.4V in coin-type half-cell at 24 °C, and (d) voltage profiles of (c) at the end cycle of each C rate (charge and discharge rates were same)100

Figure S6. Voltage profiles of bare graphite (black line), etched graphite (blue line), SiNWs-BG (cyan line) and SiNWs-PG (red line) after 10th (dot), 30th (dash), and 100th (solid) cycle101

Figure S7. (a and b) SEM images of Si nanowires grown from porous graphite at different position, and cross-sectional SEM images of SiNWs-PG electrode before (c) and after (d) 100 cycling102

Chapter V. 3D Amorphous Silicon on Nanopillar Copper Electrodes as Anodes for High-Rate Lithium-Ion Batteries

Figure 1. Schematic of the fabrication of 3D amorphous on Si nanopillar Cu electrode. (a) Patterned polyvinyl chloride (PVC) obtained from thermal roll-to-roll processing, (b) Cu nanopillar substrate applied via electroplating, (c) amorphous Si deposited on the Cu nanopillar substrate by low-pressure chemical vapor deposition (LPCVD)120

Figure 2. Electrode configuration of 3D amorphous on Si nanopillar Cu electrode by electron microscopy. Cross-sectional TEM images of the overall configuration of the (a) blanket film, (b) *a*-Si/3D-Cu electrode with 250 nm diameter nanopillars, and (c) *a*-Si/3D-Cu electrode with 500 nm diameter nanopillars. (d, e, and f) Expanded views of each structure at the interface between the Cu and *a*-Si layer (rectangular regions in a, b, and c) (inset: FFT analysis for *a*-Si). (g, h, and i) Energy dispersive X-ray (EDX) elemental mapping images of each electrode121

Figure 3. Electrochemical evaluation of 3D amorphous Si on nanopillar Cu electrode. (a) First cycle voltage profiles of the blanket film and *a*-Si/3D-Cu electrodes with 250 and 500 nm diameter nanopillars at 0.5 C rate, and (b) plot of the discharge capacity as a function of cycle number and

coulomb efficiency at 0.5 C rate between 0.005 and 1.5 V in a 2032 coin-type half-cell (1 C = 2000 mA/g). (c) Rate capability of the blanket film and both *a*-Si/3D-Cu nanopillar electrodes from 0.5 to 20 C rate between 0.005 and 1.5 V followed by recovery at 0.5 C, and the cycle retention plot at 20 C (the charge and discharge rates were same)122

Figure 4. The morphology change before and after electrochemical test. SEM images of the as-fabricated (a) blanket film, (b) *a*-Si/3D-Cu electrode with 250 nm diameter nanopillars, and (c) *a*-Si/3DCu electrode with 500 nm diameter nanopillars, and (d, e, and f) the blanket film and *a*-Si/3D-Cu electrodes with 250 and 500 nm diameter nanopillars after 100 cycles, respectively (inset: top view)123

Figure S1. The description of the deformed pattern when Ni pillar stamp has the aspect ratio more than 9124

Figure S2. SEM images of (a) blanket film and (b and c) Cu nanopillar electrode with 250 and 500 nm diameter after e-beam evaporation and electroformation, respectively125

Figure S3. XRD patterns of the blanket film126

Figure S4. (a and d) Cross-sectional TEM images of the overall configuration of the *a*-Si/3D-Cu electrode with 250 and 500 nm diameter nanopillars after 100 cycles, and (b and e) Expanded views of each structure at the interface between the Cu and *a*-Si layer, respectively (rectangular regions in a and d) (inset: FFT analysis for a-Si). (c and f) Energy dispersive X-ray (EDX) elemental mapping images of each electrode127

Figure S5. Differential capacity curves of (a) blanket film, (b and c) *a*-Si/3D-Cu electrode with 250 and 500 nm diameter nanopillars for 1st and 100th cycle, respectively128

Figure S6. SEM images of the as-fabricated *a*-Si/3D-Cu electrode with 250 and 500 nm diameter nanopillars before (a and b), and after 100 cycles (c and d), respectively129

Figure S7. Voltage profiles of (a) blanket film, (b and c) *a*-Si/3D-Cu electrode with 250 and 500 nm diameter nanopillars at various C rates, respectively130

Figure S8. SEM images of the (a) blanket film, *a*-Si/3D-Cu electrode with (b) 250 and (c) 500 nm diameter nanopillars after 300 cycles at 20 C (inset: top view)131

Chapter VI. Lithium reaction mechanism and high rate capability of VS₄-graphene nanocomposite as an anode material for lithium batteries

Figure 1. (A) Cyclic voltammogram of VS₄-rGO measured in the voltage range of 0-3.0 V (vs. Li⁺/Li) at a scan rate of 0.5 mV/s during the first three cycles. (B) Discharge-charge voltage profiles of VS₄-rGO at a current rate of 0.05 C in coin-type lithium cell (2016R) at 23 °C (1 C = 1000 mA g⁻¹). (C) Corresponding differential capacity curves during the first three cycles143

Figure 2. Ex-situ XRD patterns obtained from VS₄-rGO anodes after discharging or charging to different voltages at 0.1 C: (a) pristine electrode (b-f) discharging to 2.00, 1.80, 1.65, 0.50 and 0.01 V (g) charging to 3 V144

Figure 3. TEM and EDS mapping images of (A) fully discharged electrode (inset: d-spacing of 0.333 and 0.208 nm corresponding to (111) and (220) plane, separately) and (B) fully charged electrode (inset: S-rich regions with amorphous state) of VS₄-rGO at 0.1 C (1 C = 1000 mA g⁻¹)145

Figure 4. (A) Nyquist plot of VS₄-rGO based coin-type lithium ion cell (2016R) before and cycling. (B and C) TOF-SIMS spectra of VS₄-rGO composite electrode before and after discharge-charge146

Figure 5. (A) Voltage profiles of VS₄-rGO at a current rate of 4 C in coin-type lithium cell (2016R) at 23 °C. (B) Cycling performance of VS₄-rGO at 4 C (1 C = 1000 mA g⁻¹). An initial formation cycle at a low current rate of 0.1 C was applied before the discharge-charge cycling at 4 C rate147

Figure 6. (A) Voltage profiles of VS₄-rGO and VS₄-10 wt% CNT at different current rates in coin-type lithium cell (2016R) at 23 °C (solid line: VS₄-rGO, dash line: VS₄-10 wt% CNT). (B) Rate performance with increasing charge rate from 2 to 20 C. The discharge rate is fixed at 0.1 C (1 C = 1000 mA g⁻¹) ..148

Figure 7. (A) Voltage profiles of LiMn₂O₄/VS₄-rGO in a coin-type full-cell (2032R) between 4.3 and 1.0 V at a rate of 0.5 C after the formation cycle at 0.1 C. (B) Corresponding discharge capacity as a function of cycle number149

Figure S1. (A) Powder XRD pattern of the as-prepared VS₄-rGO composite. (B) Structure of linear chained VS₄ with alternating bonding and nonbonding contacts between the octa-coordinated vanadium centers151

Figure S2. (A) SEM (B) TEM, and (C) HR-TEM of VS₄ in the as-prepared VS₄-rGO composite152

Figure S3. EDS mapping images of the VS₄-rGO composite153

Figure S4. Capacity retention of rGO at a rate of 4 C (1 C=1000 mA g⁻¹)154

Figure S5. (A) SEM and (B) TEM images of the as-prepared VS₄-10 wt% CNT composites155

Figure S6. Cycle performance of VS₄-10 wt% CNT composites at 4C and 23 °C156

List of Tables

Chapter I. Stationary Electric Energy Storage – Battery

Table 1. The characteristics of potential and kinetic energy storage system: pumped hydro, compressed air and flywheel	21
Table 2. The chemistry and characteristics of developed electrochemical energy storage system	22

Chapter II. The Details in Li-ion Batteries

Table 1. The characteristics comparison between NiMH and LIB	53
Table 2. Li-ion batteries configuration and characteristics	55
Table 3. The market share and expectation of secondary batteries	58
Table 4. The cell materials in electric vehicles depending on the battery companies	59
Table 5. The specifications of PHEV depending on automobile manufacturers	60
Table 6.1. The classification of ESS	63
Table 6.2. The classification and properties of ESS	63
Table 7. The main companies of LIB materials, parts, and cell makers	64
Table 8. The classification of cathode materials	66
Table 9. The comparison of various graphite	67

Chapter IV. Etched Graphite with Internally Grown Si Nanowires from Pores as an Anode for High Density Li-Ion Batteries

Table. S1. The specification and electrochemical performance of silicon/graphite composites in previous works	103
---	-----

Nomenclature

3D: 3-dimensional	HEV or HEVs: hybrid electric vehicles
AAO: anodic aluminum oxides	HR-TEM: high resolution transmission electron microscopy
Al ₂ O ₃ : alumina	ICE: internal combustion engine
AQDS: 9,10-anthraquinone-2,7-disulphonic acid	ICP-MS: inductively coupled plasma mass spectrometry
BEV: battery electric vehicles	ION-TOF: TOF-SIMS spectrometer
C.E. or CE: coulomb efficiencies	LCO: lithium cobalt oxide, LiCoO ₂
C ₂ H ₅ NS: thioacetamide	LFP: lithium iron phosphate, LiFePO ₄
CAES: compressed air energy storage	LIB: lithium-ion batteries
CH ₃ CN: acetonitrile	LiPF ₆ : lithium hexafluorophosphate
CMC: sodium carboxymethyl cellulose	LMO: lithium manganese oxides, LiMn ₂ O ₄
CV: cyclic voltammogram	LPCVD: low-pressure chemical vapor deposition
DBBB: 2,5-di-tert-butyl-1,4-bis(2-ethoxyethoxy) benzene	LTO: lithium titanium oxide, Li ₄ Ti ₅ O ₁₂
DEC: diethylene carbonate	MCMB: microcarbon microbeads
DMC: dimethyl carbonate	Na ₂ S ₅ : sodium pentasulfide
DOE: department of energy	Na ₃ VO ₄ : sodium orthovanadate
EC: ethylene carbonate	NAS: sodium-sulfur
EDOT: 3,4-ethylenedioxythiophene	NCA: Li(Ni _x Co _y Al _z)O ₂
EDX: energy-dispersive X-ray	NCM: Li(Ni _x Co _y Mn _z)O ₂
EES: electric energy storage	NiMH: nickel metal hydride
EIS: electrochemical impedance spectroscopy	NMP: N-methyl-2-pyrrolidone
EMC: ethyl methyl carbonate	NRFB: non-aqueous redox flow battery
ESS: energy storage system	OCV: open-circuit voltage
EV or EVs: electric vehicles	OEM: original equipment manufacturer
FEC: fluoroethylene carbonate	OER: oxygen evolution reaction
FFT: fast-fourier transform	ORR: oxygen reduction reactions
FIB: focused-ion-beam instrument	PHES: pumped hydro storage
GHG: greenhouse gas	PHEV or PHEVs: plug-in hybrid electric vehicles
GO: graphene oxide	PXRD: powder X-ray diffraction
H ₂ : hydrogen	
H ₂ SO ₄ : sulfuric acid	

RFB: redox flow battery

rGO: reduced graphene

RT: room temperature

SEI: solid electrolyte interface

TEABF₄: tetraethylammonium tetrafluoroborate

TEMPO: 2,2,6,6-tetramethyl-1-piperidinyloxy

TOF-SIMS: time-of-flight secondary ion mass spectrometry

UPS: uninterruptible power supply

VLS: vapour-liquid-solid

VRFB: all vanadium redox flow battery

WLL: waste-Li-liquid

xEV: all kinds of electric vehicles

Chapter I

Stationary Electric Energy Storage – Battery

1. Introduction: The need of electric energy storage system

Current oil- and nuclear-based energy systems have become global issues. Recent news headlines are evidence of this, from the BP-Gulf oil spill and nuclear meltdown at the Fukushima Daiichi nuclear power plant to global demands for reduced Greenhouse Gas (GHG) emissions.¹⁻³ These challenges can be addressed through the introduction of smart cities that are based on using a stable smart grid with a clean energy power system.⁴ Harnessing a green energy from renewable energy sources and storing it in electric energy storage (EES) for electric power has been widely considered an optimal solution for future smart city power system. In this system, energy can be generated from clean and renewable energy resource such as solar, wind, and wave, but it is not constant and reliable due to its dependence on weather, facing a fluctuation in output, unavailability, and unpredictability.⁵ Hence, the use of a large scale stationary EES combined with energy generation system (solar panel, wind turbine, and water turbine) has been also considered to improve a reliability and overall use of the power system, which provides various kinds of grid services such as frequency regulation, spinning reserve, and power quality.⁶

EES can be highly employed for load leveling services that saves an electric energy whenever the renewable system generates too much for a given demand and supply to grid system when there is too little generation, as shown in **Figure 1**.⁷ For the more impact of EES in smart cities, it should provide grid stability through flexibility, fast energy injection and extraction as well as enhance power quality with supply security. To meet the above requirements, many types of ESS systems have been extensively investigated, which are described depending on how the electrical energy is stored (**Figure 2**).⁸⁻⁹

Among them, potential energy storage such as commercial pumped hydro storage (PHES) and compressed air energy storage (CAES) has been conventionally considered because their power can reach up to GW level for bulk energy storage with a low life cycle capital cost (50-200 \$/kWh).¹⁰ In PHES, it uses a stored water at a relatively high elevation (water potential) to produce electricity. During periods when electric demand is low, the extra electric energy is used to pump water back to the upper reservoir, and then the stored water is allowed to activate a turbine generating a high value electricity (a few tens of GW to MW) for peak hour.¹¹ This system has a conversion efficiency of about 65-80%, and its capacity is dependent on height and volume of the stored water. CAES also has been considered as a good candidate for EES system because it stores a large amount of electric energy with more than

100 MW. This system has a fast energy conversion and storage process, so it has been designed for daily working of the partial and quick load conditions.¹²⁻¹³ CAES stores the energy by compressing air as an elastic potential energy. It has a separate compression and expansion process. During low demand, the extra electric energy is stored in the form of compressed air under air storage space. When the demand is high, the compressed air is converted to an electric energy through an energy conversion process using a high pressure turbine. CAES has an eco-friendly system, long storage period (> 1 year), low capital cost (\$50 to \$110 per kWh), and the storage efficiency in the range of 70-89%.

In kinetic energy storage system, flywheel technologies have been attractive over the past few decades for bulk energy storage applications.¹⁴ This system utilizes the energy in the angular momentum of a spinning mass. The energy is stored by spinning of flywheel by motor. When needed, the motor generates electric energy from the rotational energy of the flywheel. The overall system is dependent on the size and speed of the rotor, and the power rating is determined by the motor-generator. The main advantage of flywheel is a long life time with several hundreds of thousands of full cycles, and additionally it has a high efficiency of 90-95%. This system is mainly applied to the high power/short duration EES applications (e.g. 100s of kW/10s of second), which provides a support power during interruption for short time or shifting one power source to another. **Table 1** describes EES technologies that have been commonly considered. Depending on the application of the system, each storage design is more suitable either in efficiency, lifetime, discharge time, weight, and/or mobility of the system. The limitation for each technology is also summarized. For examples, PHES requires an available sites for two large reservoir with different water elevations, long lead-time (> 10 years), and high cost for the construction as well as an environmental consideration.¹⁵ CAES's main barrier is to select a favorable geography and to require gas turbine system containing a combustion process with fossil fuel, resulting in a contaminating emission.¹⁵⁻¹⁶ The disadvantages of the flywheel technology are a high rate of self-discharge caused by a high frictional loss, a high initial cost, and a low energy density.¹⁷ These drawbacks of the above systems make them useful in limited range of applications.

Among these various energy storage systems, electrochemical storage such as batteries has the advantage of being more efficient compared to pumped hydroelectric and CAES storage as described below. It can be located anywhere without a geographical consideration, which allows it to be installed near residential area. Its size can be designed in applications ranging from a few kWh to several MWh. It can be simultaneously applied to both power and energy management applications.^{9, 18} A battery works by directly converting chemical energy to electrical energy by employing different chemical reactions. The many different combinations of anode, cathode and electrolyte materials to produce different cell chemical reactions thereby produces numerous types of batteries such as the Li-ion, lead-acid, Na-S, and vanadium redox batteries. Presently, the Li-ion rechargeable battery is the most common type of battery used in consumer portable electronics due to its high energy density per weight or volume

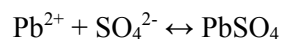
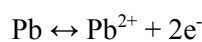
and its good recharge efficiency. However, the Li-ion battery for use in stationary energy storage applications is limited by its high cost (> \$1,000/kWh). For renewable energy to be stored without government subsidy, the storage process must be kept below \$200/kWh.¹⁹ Considering many aspects including cost, life-time, efficiency, power, and energy density, many battery systems have been applied for large-size energy storage applications. In this review, we categorized battery system depending on the degree of development for stationary applications, and offer a comprehensive description on each battery to provide a better understanding. In detail, each system will be demonstrated with principle of operation, its status and challenges in the applied chemistry.

2. Battery for EES applications

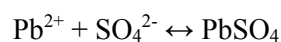
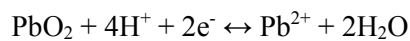
2.1. Lead-acid battery

After the development of an original lead-acid battery by Gaston Planté in 1859, it has been adapted in various applications from engine starting in electric vehicles (EVs) to EES in renewable energy system.²⁰⁻²⁴ This system consists of lead dioxide (PbO₂) as a positive electrode and metallic lead (Pb) with high surface area as a negative electrode. The configuration of lead-acid battery and its discharge/charge mechanism named double-sulfate reaction is illustrated in **Figure 3** [25, 26].²⁵⁻²⁶ It utilizes an electrode reaction of Pb oxidation ($\text{Pb} \rightarrow \text{Pb}^{2+} + 2\text{e}^-$) and of PbO₂ reduction ($\text{Pb}^{4+} + 2\text{e}^- \rightarrow \text{Pb}^{2+}$) during discharging, resulting in the formation PbSO₄ product on both electrodes. This process is reversible on charge state. The overall reaction is described as followings:

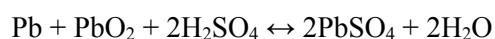
Negative electrode:



Positive electrode:



Overall reaction:



As shown in process, the sulfuric acid (H₂SO₄) in an aqueous electrolyte is consumed to produce PbSO₄ and H₂O products during discharge, and it can be an additional active component that limits the electrochemical performance of the lead-acid battery system. The overall reaction in a cell provides a

standard voltage of 2.1 V, and the acceptable end-voltage on a moderate discharging is 1.75 V per cell. Open circuit voltage changes depending on an electrolyte concentration, which indicates that the state of charge in the lead-acid battery system can be determined by measuring a relative density of sulfuric acid. However, when the cell is overcharged at the higher value than ~2.39 V, the aqueous electrolyte decomposes by evolution of hydrogen ($2\text{H}^+ + 2\text{e}^- \rightarrow \text{H}_2$) and oxygen ($\text{H}_2\text{O} - 2\text{e}^- \rightarrow 1/2\text{O}_2 + 2\text{H}^+$) at the negative and positive electrode, respectively. This leads to loss of water in electrolyte, requiring maintenance by additional supplement. Lead-acid battery has been introduced in various electronic power applications due to its advantage of ease manufacturing in 1 Ah to ~1000 Ah-sized products. This battery can also provide a moderate value of power and energy rating with kW to a few ten's MWs, a good electrical efficiency (>70%), and a long lifetime (3-12 yrs.) as well as a relative low-cost range.^{21, 27} In addition, the cell components (especially lead) can be efficiently recycled at high rate with 97% from used batteries. However, the cycle-life of the lead acid battery can be limited. Lead sulfate layer can be formed on the surface of negative electrode during high discharge rate, which is not completely reversible during recharging process.²⁸⁻²⁹ This eventually reduces the electrode area for the electrochemical reactions, resulting in poor cycle life performance. In addition, charging of the cell at a high current rate produces a hydrogen generation, which also causes a poor round-trip efficiency and explosion hazard.^{21, 30}

To improve cycle-life extension of a lead acid battery, carbon is attempted to be used in negative electrodes because its small content (0.15-0.25 wt%) on the negative electrode was reported to reduce the PbSO_4 accumulation on the electrode's surface.³¹⁻³³ When the negative lead electrode is completely replaced by high-surface-area carbon, called lead-carbon (PbC) asymmetric system, the nucleation and growth of PbSO_4 are eliminated by no chemical reaction on the negative electrode, which greatly enhances a cycle-life performance.³⁴ On the other hands, as an advanced lead acid system, the split design of the negative electrode (known as ultra-battery) is demonstrated as shown in **Figure 4**. This system uses Pb being parallel connected with the modified carbon as the negative one with one PbO_2 positive electrode, in which provides a high capacity and significantly long cycle-life.³⁵ Compared to the traditional lead acid battery, the split design of the ultra-battery system exhibits an improvement with 50% discharge power, 60% charge power, and ~17000 cycles.

Despite of such improvements in in lead acid ultra-battery system, the low cost and high durations are still further required for stationary EES applications. In the case of capital cost, the value of ultra-battery system (\$500/kWh) is higher than that of valve-regulated lead-acid system (\$200/kWh), but it is possible to reduce a cost by increasing production's scale. For now, the lead acid battery system is only applied in EES applications that require relatively short discharge duration. If the main barriers of the lead acid batteries can be overcome, it can be available for a large scale energy storage with a high power and energy.

2.2. Na-S battery

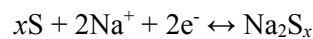
As an introduction of sodium-sulfur (NAS) battery system in 1970s, this technology has been considered to be an attractive candidate for a large-scale EES application due to the abundant sodium (Na) with its low redox potential, high theoretical specific energy ($\sim 760 \text{ Wh kg}^{-1}$), and cycling flexibility.^{9, 36-37} The NAS system is constructed in a tubular design, as shown in **Figure 5**. This system is composed of Na as an anode, S as a cathode, and beta-alumina (Al_2O_3) as a solid electrolyte and separator. The cell needs to be operated at high temperatures between 300 and 350 °C, which are required to maintain Na and S in molten states and make efficient Na ion transportation through the ceramic solid electrolyte.³⁸

During discharge process, Na at a negative electrode is oxidized, giving a Na^+ ions. These Na^+ ions move through the solid electrolyte and react with S at a positive electrode, forming a sodium pentasulfide (Na_2S_5). The Na_2S_5 is separated from the remaining S and yields two-phase liquid mixture. However, the two-phase liquid mixture is gradually transformed to the single phase sodium polysulfide with high sulfur content ($\text{Na}_2\text{S}_{5-x}$) when the remaining S is completely consumed. The above chemical reactions are reversible during the charge process, and the overall reactions are as follows:

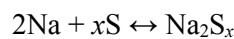
Negative electrode:



Positive electrode:



Overall reaction:



At the temperature of 350 °C, the NAS battery exhibits the constant voltage of 2.07 V until 60 ~ 75 % of discharge process, representing two phase mixture of S and Na_2S_5 . After that, the voltage starts to linearly decrease (corresponding to the formation of single Na_2S_x), and approach to 1.78 V at the end of discharge.³⁹ In this battery system, the solid state electrolyte based on beta-alumina ceramic ($\beta\text{-Al}_2\text{O}_3$ or $\beta''\text{-Al}_2\text{O}_3$) has been mainly used due to its adequate ionic conductivity of $0.2\sim 0.4 \text{ Scm}^{-1}$ at 300 °C.⁴⁰⁻⁴² The crystal structure and electrochemical behavior of the $\beta''\text{-Al}_2\text{O}_3$ has been further stabilized and improved by introducing Li^+ or Mg^{2+} ions into the structure with ideal composition.⁴³ The solid electrolyte is one of the key elements determining a battery performance and cost. The sealing material for the solid electrolyte is also very important elements for the NAS battery system. If the both electrodes with liquid state are in direct contact with each other at a high temperature, it causes severe fire and explosion. For instance, NAS battery incident occurred in 2011 because the molten active

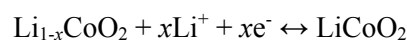
materials flowed over sealing material between block, causing a continuous short-circuit between battery cells.⁴⁴ Glass-ceramic sealants based on borosilicate have been widely considered to prevent the direct contact between two molten electrodes. These have high strength and chemical stability, no phase transformation, little stress variation during thermal operation, and controllable thermal expansion displaying a favorable performance.⁴⁵⁻⁴⁶ Bi-doped borosilicate is also introduced for an attractive sealant due to its well-matched thermal expansion between glasses and solid electrolyte.⁴⁷ Another main issue for NAS batteries is that the discharged products such as sodium polysulfide are electronic insulator. Hence, the discharge products should be presented in carbon source materials as electronic conductor to provide an efficient electron-transport, and additionally, highly corrosive behavior of the molten cathodes requires anti-corrosive current collector.^{43, 48}

The use of NAS battery has been considered for load-leveling or peak shaving in large scale EES applications with ~65% market share.⁴⁹ However, this system still further requires the safety and initial cost-reduction (~\$350/kWh) along with cell engineering.¹⁰ Moreover, one of the main issue is to reduce the operation temperature, which allows one to select more cost-effective materials in a cell with better materials' durability and to handle efficient thermal management. To solve this problem, extensive works have been performed to decrease the operating temperature by the use of polymers or organic solvents as the catholytes.⁵⁰⁻⁵⁴ For example, the utilization of a solid electrolyte with a catholyte solvent enhanced the interfacial conduction and the mobility of components in the cathode.⁵⁵ At present, since NAS battery has been widely applied in a large scale EES application, the advanced technology can provide a reduction of battery cost and improvement of its reliability for large scale EES if the above problems are solved.

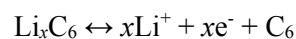
2.3. Li-ion battery

At the present, Li-ion batteries (LIBs) have been considered for the use in a large scale EES market. Conventionally, this battery system uses Li transitional metal oxides as the cathodes, carbons as the anodes, and non-aqueous carbonated liquids as the electrolytes as shown in **Figure 6**.⁵⁶ During charge process, Li ion is transferred across the electrolyte from the anode host structure to the cathode electrode, and this chemical reactions is very reversible. The overall reaction is described as followings:

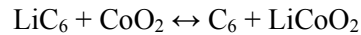
Positive electrode:



Negative electrode:



Overall reaction:



The Li-ion battery system can operate at ~ 3.7 V with exhibiting high specific energy densities of ~ 150 Wh kg^{-1} and ~ 400 Wh l^{-1} . This high energy density performance makes it attractive for the use in weight or volume sensitive applications.⁵⁷ Also, the Li-ion battery exhibits a low self-discharge of below 8% per month, a long cycle-life of greater than 1000 cycles, and wide operation temperature ranges ($-20 \sim 60$ °C for charge / $-40 \sim 65$ °C for discharge).⁵⁸ Its main drawbacks are high cost, low temperature tolerance, and the protective system for cell degradation and thermal runaway from electrolyte decomposition.⁵⁶ Although the use of a solid polymer as the electrolyte in Li-ion battery system become enhancing a safety and more flexibility, but the design cost is increased with a decreased scalability.

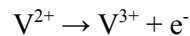
Nowadays, although Li-ion batteries took a large possession of area in portable electronic devices, but there are several kinds of challenges for stationary EES applications. The first consideration is its high energy cost ($> \$600/\text{kWh}$) that is 2~5 times higher than the required cost for stationary applications.^{10, 59-60} Also, thermal management should be efficiently operated in a large scale application with MW levels, which is closely related to a safety and extended cycle-life. The generated heat from the Li-ion battery has induced a thermal instability of a flammable organic electrolyte, and this issue would be more important in a large scale EES application.⁶¹ Recently, to meet cost and safety requirements for EES applications, Li-ion batteries is designed with using LiFePO_4 as the cathode and $\text{Li}_4\text{Ti}_5\text{O}_{12}$ as the anode.⁶²⁻⁶⁴ $\text{Li}_4\text{Ti}_5\text{O}_{12}$ is well known to have zero straining Li-intercalation/de-intercalation behavior with a specific capacity of 175 mAh g^{-1} , exhibiting a voltage plateau at 1.55 V vs. Li. Although the voltage of $\text{Li}_4\text{Ti}_5\text{O}_{12}$ is relatively high for anode applications, it shows an excellent cycling stability and safety compared to those of the commercially used carbon anode (0.2 V vs. Li) because the $\text{Li}_4\text{Ti}_5\text{O}_{12}$'s operating voltage is beyond the electrolyte decomposition voltage (< 0.8 V vs. Li). As the cathode, LiFePO_4 has been considered to be a promising candidate due to its low cost, plentiful, and environmentally benign elements. In addition, LiFePO_4 has a durable crystal structure composed of bonding between iron and oxygen, which leads to a stable and reversible electrochemical performances for many cycles of Li intercalations into its structure as well as a thermal runaway at high temperature [65-68].⁶⁵⁻⁶⁸ Its capacity is good (~ 170 mAh g^{-1}), but its working voltage is relatively low (~ 3.45 V vs. Li) The Li-ion battery system can be enabled as a large scale EES system if the further requirements are well combined within in cost-effective range.

2.4. Redox flow battery: All-vanadium

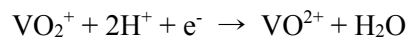
For a large scale EES system with the range from 10 kW to 10 MW, redox flow battery (RFB) is an attractive candidate when considering its cost, mobility, depth of discharge, fast response and safety and comparing them to those of LIBs and NAS system.⁶⁹ RFB has exhibited a high energy efficiency

that is induced by redox couples' electrochemical reactions in liquid solutions. Among a variety of redox couples, all vanadium redox flow battery (VRFB) provides an excellent electrochemical performance.⁷⁰ A typical VRFB system consists of two external reservoirs containing a soluble electroactive species (V^{4+}/V^{5+} as the positive chemicals and V^{2+}/V^{3+} as the negative chemicals) and two stacked electrodes. These two sections are separated by an ion-exchange membrane and have pumping circulation system (**Figure 7**). The electrochemical reaction is as followings during discharge:

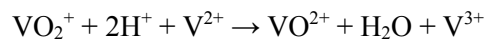
Negative electrode:



Positive electrode:



Overall reaction:



The standard open circuit voltage (OCV) is 1.26 V, and the voltage is increased to 1.6 V at the fully charged state in the cell system with 2 M $VOSO_4$ in 2.5 M H_2SO_4 electrolyte.⁷¹ The VRFB system can be applied in a temperature range of 10~40 °C.⁷² Since the same vanadium species with different oxidation states are used in each cell, the VRFB system doesn't have cross contamination problems. It enables the electrolyte to be recycled in the cell, leading to a long cycle-life and the reduction cost of the battery system. Also, the fast electrochemical reaction of vanadium redox couples allow the VRFB to be highly discharged/charged at a short time.⁷⁰ However, VRFB has several drawbacks for practical applications. The main problem is its lower specific energy density (25~30 Wh kg^{-1}). The energy density of the VRFB is highly related to the concentration of vanadium ions in the liquid H_2SO_4 solution, and its maximum concentration is limited by the precipitation of solid vanadium compound.⁷³⁻⁷⁶ Several approaches have been tried to increase the solubility of vanadium in the liquid solution. However, the vanadium concentrations in the electrolyte and its effects on the electrochemical performances (state of charge, energy density) are still remains as main challenge in VRFB. The highly oxidizing ability of V^{5+} should be addressed to maintain overall system in fully charged positive electrolyte because it easily degrades membrane and positive electrode materials.^{18,77} The V^{5+} oxidizing ability limits the choice of materials for membrane and positive electrode; New Selemon anion exchange membrane or Nafion cation exchange membrane are used, and carbon or graphite felt is used as the electrodes.

At the present, although all-VRFB system has been widely used in applications for load-leveling and uninterruptible power supply (UPS) due to its excellent electrochemical reversibility, its cost reduction is still essential for stationary EES applications. Vanadium is still expensive (\$7 - \$14 per

pond). Moreover, the membrane is the highest price component of the VRFB system, which should be considered with low-cost alternatives.³⁸ It is reported that a modified perfluorinated membrane is developed to reduce the cost, and its performance demonstrates an energy efficiency of 80 % in 5~10 kW battery stacks.⁷⁸ If the ion exchange membrane is continuously developed with enhanced electrochemical properties such as low vanadium ion permeability, good chemical stability, and oxidation resistance toward V^{5+} , it can further reduce the cost of VRFB and improve its performance. Another issue for the further development of VRFB is carbon-based electrode materials [79-81].⁷⁹⁻⁸¹ The current electrode materials can generate a current density up to 100 mA cm^{-2} with a good energy efficiency, but further improvement is needed to increase stack power density with the reduction of stack cost per kW power output.⁸² In addition to the electrode/membrane materials, the design of overall system is also important to improve electrochemical performance and build cost-effective system.³⁸ In the present design, the parasitic current appears because the electrodes in stacks cell are fed with pumped electrolyte in parallel, which leads to self-discharge and energy loss. The shunt current is also existed due to the voltage difference between stack cells, inducing a corrosion of materials of cell stack with capacity loss.⁸³ Accordingly, if VRFB system is designed to eliminate electrical leakage currents with the improvements of other components, it can further improve the electrochemical performances as well as cost reductions for stationary EES applications.

3. Recent Progress in Battery for EES applications

Although the commercialized batteries are widely installed in stationary applications, their energy density is still insufficient for a large scale EES due to the intrinsic limitations in the current electrode materials for the batteries. Major research trend has moved to potentially high capacity electrodes such as metal anodes and air cathodes. Additionally, to be competitive EES systems, the cost of batteries should be reduced with keeping or enhancing their electrochemical performances. Therefore, the new battery technology is highly required to provide successful EES requirement parameters such as high energy density, low cost, increased safety, and environmental compatibility. In next chapter, we will review the suggested technologies with principles and developed components for stationary EES systems.

3.1. Metal-Air battery: Zn-Air

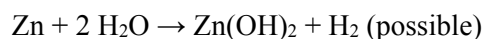
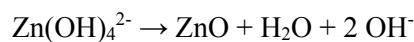
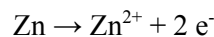
Metal-air batteries have attracted attention due to their higher energy density than other battery systems mentioned in previous chapters (**Figure 8**). Metal-air batteries generally consist of a metal anode, air-cathode, a separator, and metal-ion conducting electrolyte (**Figure 9**). During discharge

process, metal anode is oxidized with providing free electrons, and the oxygen accepts the released electrons at the cathode electrode, forming an oxygen-containing species as reduction products. The oxidized metal ions and oxygen-reduced species migrate through electrolyte, and they are combined to form metal oxides. These reactions are reversible with forming metal at the anode and oxygen generation at the cathode, respectively, when charging of the battery. The main considerations of metal-air batteries are a low efficiency of the anode utilization and a slow kinetics of the cathode [84, 85].⁸⁴⁻⁸⁵ For the air cathode, the use of a catalyst is required to improve an oxygen reduction reaction (ORR) at the liquid-gas-solid interface. Due to a low solubility of oxygen in liquid electrolyte, the degree of oxygen transport in electrolyte also plays a key role of improving an electrochemical performance.⁸⁶⁻⁸⁷ For the metal anode, the precipitated metal oxides, hydroxides, or other species on the metal anode surface impedes a discharge process due to a retardance of electrolyte contact.⁸⁴

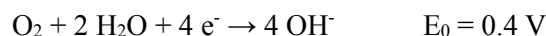
Recently, among various metal-air batteries, zinc (Zn)-air battery system has been considered for the stationary EES application due to high abundance, low cost, and environmental compatibility of Zn. In Zn-air battery, the air cathode electrode consists of a catalytic active layer and gas diffusion layer as schematically illustrated in **Figure 10**.

When oxygen is introduced into the porous electrode, the catalyst of the electrode accelerates ORR to form hydroxyl ions in alkaline electrolyte. The hydroxyl ions move to zinc anode and contribute to the formation of zinc oxides (final product) during discharge process. The additional chemical reaction possibly occurs, leading to the evolution of a hydrogen gas in negative electrode, and the suppression of hydrogen evolution is needed to increase the capacity of this system.⁸⁸⁻⁸⁹ The overall reactions are described below:

Negative electrode:



Positive electrode:



Overall reaction:



The theoretical specific energy density of Zn-air battery is 1350 Wh kg^{-1} , but the operating voltage is less than theoretical value due to the internal polarization of cell.⁹⁰⁻⁹¹ There are several challenges such as the electrochemical stability of the cathode electrode during charge, dendrite formation at zinc electrode, zinc dissolution, limited oxygen solubility in electrolyte, and higher value of charge polarization than that of discharge one.⁹² Therefore, these challenges should be addressed to apply Zn-air battery system into EES applications. Each challenge part and its solution will be discussed below.

Negative Electrode: Pure Zn metal is utilized as the negative electrode in Zn-air battery system, where Zn metal is oxidized and transformed to zinc oxide when discharging. The morphology of Zn electrode is transformed during cycling of the battery due to the uncontrolled dissolution of Zn in electrolyte. This continuous precipitation creates and grows a dendrite that eventually touch the positive electrode, which results in a short-circuit.⁹³ In order to efficiently utilize zinc electrode, the modification of its surface area has been mainly considered to optimize reaction rate with an alkaline electrolyte.⁹⁴⁻⁹⁶ In addition to Zn's precipitation problem, the evolution of hydrogen (H_2) gas caused by the corrosion of Zn is also a major drawback, resulting in an increase pressure of the battery during cycling. To overcome these problems, zinc alloy with other metals has been attempted.⁹⁷⁻⁹⁸ However, because the introduced metals such as Hg and Pb are toxic and can cause the environmental problem, Ni or In based alloy have been used to efficiently utilize zinc electrode with high electrochemical performance.⁹⁹ Also, the method of coating Zn surface with other materials has been introduced to prevent a direct contact between Zn and electrolyte, which increase discharge capacity with a low gas evolution.¹⁰⁰⁻¹⁰¹

Separator: A separator plays a key role of transporting a sole hydroxyl ion (OH^-) from air electrode to zinc electrode. It should have a high ionic conductivity, proper porosity, non-electronic conductivity, high adsorption of electrolyte, stability in alkaline solution, and retardance of Zn dendrite formation. Among the various kinds of separator candidates, polyethylene oxide and polyvinyl alcohol have been widely used due to their appropriate properties in alkaline based applications. Mesoporous membrane (MCM-41) is recently developed.^{92, 102-105} This new membrane enables Zn-air cell to increase power density and volumetric energy density, which are comparable to the commercial value such as Duracell's DA 675 model.

Electrolyte: Potassium hydroxide (KOH) is widely used as the electrolyte for Zn-air battery due to its high ion-conductivity, and its conductivity can be further improved by the increase in concentration of KOH.¹⁰⁶ However, the use of more than critical concentration ($\sim 30\%$ of KOH) can lead to viscosity increase of the electrolyte and ZnO formation. The hydroxyl ions in the electrolyte are very sensitive and reactive with carbon dioxide, which contributes to the formation of carbonate. This results in a capacity loss of the battery. Hence, the use of absorbents in a cell has been considered to reduce CO_2 concentration,¹⁰⁷⁻¹⁰⁹ which leads to significant reduction of CO_2 below 20 ppm with compact device design.¹⁰⁶⁻¹⁰⁸

Positive Electrode: Air cathode of Zn-air cell is comprised of a catalyst for ORR and porous carbon structure. The porous structure of the electrode can provide a high diffusion pathway for oxygen in air and house catalyst materials. However, when cell operates, the porous electrode structure can be clogged or collapsed by discharged or decomposed products such as potassium carbonate, resulting in capacity loss.⁹³ For air electrode substrate, a variety of carbon materials have been investigated. Carbon black is widely considered as the most conventional support. Carbon nanostructures such as 1D-nanotubes or nanofibers, 2D-graphene nanosheets are also introduced due to their efficient electron transport, structural integrity with the well-dispersed catalyst, and facile diffusion of oxygen.¹⁰⁹⁻¹¹¹ It is also known that electrode kinetics is dependent of the degree of defect site of the electrode materials. For example, the structure with large number of edge-plane site such as pyrolytic graphite and multi-walled carbon nanotubes exhibits a high activity toward ORR.¹¹² Furthermore, the surface treatment or doping process on carbon can also improve the electrochemical behavior.¹¹³⁻¹¹⁶ Especially, for nitrogen doping on carbon, this dopant can increase the degree of defect with more exposure of edge site in graphitic carbon, influencing a highly stable and active ORR catalyst. Based on DFT calculation for high performance induced by doping, it is suggested that edge site of carbon can lower the barrier of oxygen adsorption and electron transport.¹¹⁷

Catalyst: Catalyst is an essential element in air electrode. This reduces an oxygen reduction polarization for the sluggish ORR. For potential catalysts, noble metal such as Pt and Pt-alloy has played a role of contributing a high ORR activity. However, due to the high cost of noble metals, carbon based catalyst has been investigated.¹¹⁸⁻¹²⁰ In addition, the transition metal oxides with various structure such as spinel and perovskite has been also widely investigated for the potential catalysts.¹²¹⁻¹²³ Among those candidates, Mn-based oxides with thin-film type produces an improved ORR activity that is comparable to that of noble metal catalysts, but they exhibits the low electric conductivity and instability in alkaline solution, especially at 2 V for oxygen evolution reaction (OER) during charge.¹²⁴ To overcome these problems, the addition of nitrogen-doped carbon nanotubes is introduced, which leads to 96% of retention in OER current density after 50 cycles as well as an increase of electric conductivity.¹²⁵

3.2. Advanced redox flow battery

Although there has been a continuous attention on redox flow battery for stationary EES applications, its poor electrochemical performances (low voltage and low energy density) has been remained as one of the main challenges. To overcome this problem, the advanced RFB systems have been researched, which is discussed in this section.

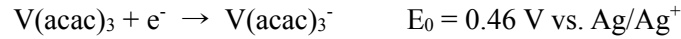
Organic-Inorganic Aqueous System: The scalability and cost of active materials are one of main issues for their use in EES applications. For this reason, a metal-free organic-inorganic aqueous flow

battery system is recently proposed.¹²⁶ This system is comprised of 9,10-anthraquinone-2,7-disulphonic acid (AQDS) in sulfuric acid as the negative electrode, Br₂ in HBr as the positive electrode, and Nafion 212 membrane between Toray carbon paper. This battery system exhibits a relatively low open-circuit potential with 0.92 V at 90% of state of charge. However, it shows not only highly reversible electrochemical performances, but also an excellent galvanic discharge maintained with > 99% over long time scale even at 0.5 A cm⁻². These remarkable results are attributed to the high reversibility of AQDS with aromatic π -system, high rate kinetic properties, and stability. Moreover, the addition of hydroxyl group can increase cell voltage and solubility as well as density.¹²⁷ Therefore, metal free flow system can provide a low capital cost of storage chemicals per kWh with enhanced electrochemical performances, which is attractive for cost-effective and large-scale energy storage applications.

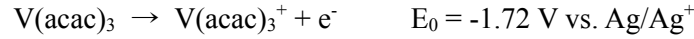
Non-Aqueous System: Conventional aqueous-based RFB systems have a low energy density due to the low electrochemical window of aqueous electrolytes and the low concentration of redox species in electrolytes. When the electrolyte has wider electrochemical windows, the choices of redox couples would be more open, including high voltage redox couples and multi-electron transfer redox species. This would be possible in non-aqueous RFB (NRFB) system.¹²⁸ The main difference between aqueous and non-aqueous RFB system is the electrolyte and supporting ions. In aqueous RFB, strong acids such as H₂SO₄ and HCl are used as the electrolyte, and proton is migrated across the membrane to balance electrical neutrality. In non-aqueous RFB system, organic solvent is utilized to dissolve redox species (metal-ligand complex), and ionic liquids are added to increase the ionic conductivity of the electrolyte in NRFB [129-131].¹²⁹⁻¹³¹ In general, NRFB exhibits higher operating voltages (> 2V) than aqueous-based RFB. However, since the solubility of redox species in non-aqueous electrolyte is lower (< 0.1M) than that of the aqueous-based electrolytes, the NRFB's other electrochemical performances such as capacity and coulombic efficiency are not satisfactory even at small current density. To overcome these drawbacks of the NRFB system, many research works have been performed. Among them, major two approaches are discussed below.

The first approach is to use metal-ligands complex as the electrolyte in NRFB. In a complex, metal takes part in a redox reaction, and ligand determines its solubility in organic solvent. Thus, if the combination of metal and ligands is well optimized, it can provide a high operating voltage with efficient solubility, resulting in higher energy density. Among various candidates, vanadium complex redox system has been widely studied.¹³²⁻¹³³ Single vanadium metal is coordinated with acetylacetonate (V(acac)₃) in the electrolyte that consists of acetonitrile (CH₃CN) as the organic solvent and tetraethylammonium tetrafluoroborate (TEABF₄) as the supporting electrolyte. Since the same electrolytes are used in both electrodes in the above system, its energy efficiency can be improved. The redox reaction is as follows during discharge:

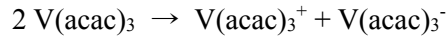
Negative electrode:



Positive electrode:

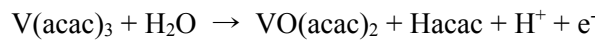


Overall reaction:



The theoretical operating voltage is 2.18 V, which is ~60% higher than that of aqueous vanadium RFB that use 2M H₂SO₄. If either charged complex is migrated to the opposite electrode, this cross-over can induce a self-discharge by a neutral intermediate, leading to the loss of charge-efficiency. However, it is not required to regenerate electrolyte solution in this battery system. However, the water and oxygen contaminations are critical for the battery performances.¹³⁴

When the system contains oxygen, the reduction ability of V(acac)₃ is decreased accompanying by a degradation of solvent and supporting electrolyte. Moreover, because V³⁺ center is easily converted to VO double bond in water, V(acac)₃ transfers to vanadyl acetylacetonate (VO(acac)₂), as following equation:



where Hacac is a protonated acetylacetonate.

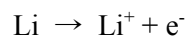
Therefore, the membrane should be immersed in the electrolyte for long time to remove water and oxygen before cell fabrication.

The second approach to overcome the limitations of non-aqueous system such as complex preparation and low solubility of redox species is all organic redox system.¹³⁵ This system is comprised of 2,2,6,6-tetramethyl-1-piperidinyloxy (TEMPO) as the catholyte, N-methylphthalimide as the anolyte, and NaClO₄ as the charge carrier dissolved in acetonitrile, respectively. As a result, the electrochemical window is evaluated to be ~1.60 V, and the coulombic efficiency (C.E.) is ~90% in the 20 cycles. Another all-organic RFB is also reported, which consists of 2,5-di-tert-butyl-1,4-bis(2-methoxyethoxy) benzene (DBBB) as the catholyte, the derivatives from quinoxaline as the anolyte, and lithium salt in organic solvent as the electrolyte.¹³⁶ The both systems provide a moderate voltage of < 2.0 V, but the value still remains with the solubility of active materials as limitations in all-organic system.

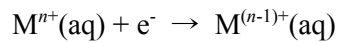
3.3. Aqueous lithium flow battery

Because Li metal has still highest specific capacity (3860 mAh g⁻¹), it is the most attractive anode for the batteries, but the efficient utilization of Li is still main challenge to obtain a high energy density in battery. Instead of using oxygen as the cathode for Li-air battery, the use of water as the cathode in Li-water battery system has been also considered. However, the Li-water battery is not rechargeable because the water loss occurred by evolution of H₂ and O₂ during discharge and charge process, respectively. Recently, aqueous Li-flow battery has been introduced, which use water-soluble redox couples in the positive electrode, as shown in **Figure 11**.¹³⁷ The electrochemical reaction is as followings during discharge:

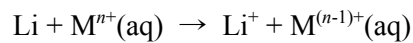
Negative electrode:



Positive electrode:



Overall reaction:



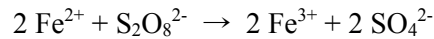
where M is transition metal ion.

In positive electrode, the dissolved redox species in water are circulated in the flow-through mode, which can be individually stored in a tank. To achieve high working voltages in a cell, it is required to select high redox potentials for positive electrode. The possible candidates in positive electrode are suggested in **Figure 12**.¹³⁸

Among the various candidates of water soluble redox species, Fe(CN)₆³⁻/Fe(CN)₆⁴⁻(aq) redox couple has been tested as the cathode for aqueous Li flow battery.¹³⁹ This battery system uses Li super ionic conductor ceramic as the solid-electrolyte, which physically separate anode part (containing Li metal and non-aqueous liquid electrolyte) and aqueous liquid catholyte but allow Li-ion transportation between them. This configuration provides a working voltage of ~3.40 V at the current density of 0.5 mA cm⁻². Its cycle retention is maintained with 99 % coulombic efficiency after 20 cycles, indicating a good reversibility with high charge/discharge efficiency. However, the cell performance is limited by solid electrolyte at high current density, which is attributed to a relatively low Li ion conductivity (1 × 10⁻⁴ S cm⁻¹) of the solid ceramic electrolyte compared to mass transport rate of aqueous cathode species.

Fe³⁺/Fe²⁺(aq) redox couple in aqueous solutions has been also investigated for its use for the cathode in aqueous Li flow battery system.¹⁴⁰ This battery system has the working voltage of ~3.35 V at a current density of 0.2 mA cm⁻². However, the working voltage is gradually dropped to below 3 V

at the end of discharge because the insufficient reduction of Fe^{3+} appeared, which was caused by the formation of $\beta\text{-FeOOH}$ via slow hydrolysis of dilute FeCl_3 aqueous in fuel tank.¹⁴¹⁻¹⁴² To overcome this problem, HCl is added to adjust the acidity with initial value ($\text{pH} = 1.7$) in stock solution, and $(\text{NH}_4)_2\text{S}_2\text{O}_8$ as oxidizing agent is added to easily oxidize Fe^{2+} to Fe^{3+} with fast time, as following reaction:



As a result, the working voltage and capacity are significantly recovered.

Aqueous Li flow battery is promising for stationary EES applications due to its high voltage and flexibility of a large-scale design, but there remains the selection of solid-electrolyte as main key challenge. If the solid electrolyte possesses high conductivity, stability, and scalability with low cost, this system can be more attractive for future large-scale EES applications.

3.4. Waste-Li-liquid flow battery

For stationary EES applications, a cost reduction of battery system is critical, which requires below \$150 per kWh in long term consideration. To respond this request, a new battery system, named the Waste-Li-Liquid (WLL) flow battery, is recently proposed as shown in **Figure 13**.¹⁴³ This is a system where Li metal is harvested from waste Li-ion batteries, and the harvested Li metal (anode) is discharged with the liquid solutions (cathodes) to produce electric energy. In the WLL battery system, the charge cathode and discharge cathode sections are separated by a solid/liquid hybrid electrolyte to extend the choices for electrode materials including liquid phase, solid phase, or a combination of both liquid and solid phases. In the charge cathode section, there are three options for supplying the Li metal to the anode section: (a) using waste Li-ion battery materials containing Li ions such as the graphite anode- Li_xC_6 , cathodes made of Li_xFePO_4 , or the organic liquid electrolyte, 1M LiPF_6 in EC:DEC, (b) using the discharged products such as LiOH (aq) created by discharging the battery, or (c) collecting Li from both sources simultaneously. As for the discharge cathode section, by using the harvested lithium metal as the anode, water and other liquid solutions containing aqueous, non-aqueous, and mixed solvents can be used as cathodes to produce electric energy.

It was reported that by using a hybrid electrolyte strategy, Li metal was harvested by charging the liquid solutions containing waste Li-ion battery materials, and the harvested Li metal was discharged with water as the cathode, producing 2.7 V vs. Li^+/Li^0 at 0.1 mA cm^{-2} (**Figure 14**). The discharged product, LiOH , can be re-cycled for Li metal harvest. Various liquid solutions can be used as the cathodes for the WLL battery system, and their voltage versus Li metal can be tuned by combining various solvents, solutes, redox couples, and counter anions. The cell performances can be limited by

the low Li-ion conductivity of the solid electrolyte. $\text{Li}_{1+x+y}\text{Ti}_{2-x}\text{Al}_x\text{P}_{3-y}\text{Si}_y\text{O}_{12}$ is commercially available solid electrolyte that provides Li-ion conductivity in the range of $10^{-4} \text{ S cm}^{-1}$.¹⁴³ The further development of the solid electrolyte is required not only for WLL battery system but also for other batteries such as Li-Ni,¹⁴⁴ Li-liquid,^{137, 139-140, 145-146} and Li-air.¹⁴⁷⁻¹⁴⁹ When used the Li metal as the anode, the formation of Li dendrite and its chemical instability has been issued, which causes a safety problem in batteries system. To address this point, Li metal anode in WLLB can be replaced by Li intercalation compounds such as graphite and $\text{Li}_4\text{Ti}_5\text{O}_{12}$ (LTO).¹⁵⁰ When LTO is adapted as the anode in the WLL battery, the working voltage is relatively low of $\sim 1.8 \text{ V}$, but it exhibits good cycle retention with 91.2% of coulombic efficiency. This is due to the LTO's high electrochemical potential of $\sim 1.5 \text{ V}$ vs. Li, which eliminate the possibility of the organic electrolyte decomposition.

The proposed WLL battery system is enable the harvesting of Li metal from waste Li-ion batteries at room temperature and produce electricity by using the harvested metal as the anode and the liquid solution as the cathode. In addition, particular liquid chemistries to be used as cathodes found to be most effective (higher discharge voltage at higher current rate) for the proposed battery system can be selected from the combination of solvents, redox couples, and counter anions. Furthermore, if this type of batteries are successful in terms of using liquid phases as cathodes, one can eliminate the complicated, expensive solid electrode processes that are required when using solid state materials as electrodes for Li-ion batteries. Hence, this approach would be cost effective and could easily make its entry into the large-scale battery market for stationary electric energy storage devices. It would be challenged, but along with the fundamental study of liquid solutions as cathodes, the results of the other studies in the WLL battery system, including the solid electrolyte, the cell components, overall system design, and the battery prototype, would demonstrate the effectiveness of the Waste-Li-Liquid (WLL) flow battery for stationary energy storage applications.

4. Conclusion

A clean and renewable energy system that is completely independent of fossil fuels may not be possible within 20 or 30 years, but society must move in this direction in order for future generations to inherit a cleaner Earth. Achieving successful stationary EES technology is essential for a renewable energy system. Among many candidates for EES system, batteries are attractive technology because it more suitable in geographical location, power and energy density, efficiency, weight, and mobility of the system. To commercialize batteries in stationary EES market, the key parameter is the capital cost that is defined as the cost per unit energy divided by the cycle life. Additionally, the long cycle performance of the battery is another key parameter for successful EES applications. The required EES parameters for many types of battery systems are summarized in **Table 2**. Unfortunately, there is no

single battery technology that meets all of the EES requirements. There always exists trade-off between one parameter and another one. Hence, the detail analysis of the candidates should be accompanied to select the appropriate energy storage system in terms of being mature, lifetime, cost, energy density and cycle efficiency. The appropriate selection of the batteries for EES applications can be mainly determined by the scale. For example, LIB is proper for the small-size EES application such as mobile phone, while RFB is more appropriate for a large-scale application. Department of Energy (DOE) in U.S.A reported the cost and performance targets for near-term and long-term EES system for the large electricity applications. In near term, the developed battery technologies such as RFB, Na-S, lead-carbon, and LIB are needed to be further developed with a capital cost of $< \$250/\text{kWh}$ and over system efficiency of $> 75\%$. In long term, the new battery technologies based on advanced system and materials are required to be developed with the cost of $< \$150/\text{kWh}$ and efficiency of $> 80\%$. Also, abundance of the electro-active materials that are used in batteries is another key factor for its applications in stationary EES system. For example, when considering the present estimate of global extractable Li reserve, the amount of Li may be enough to produce LIB for the whole fleet of electric vehicle cars. However, when LIB starts to be applied in stationary EES system, tremendous amounts of Li sources need to be spent, which makes it less available. Furthermore, it is also essential to understand and identify the electronic and chemical properties of the electro-active materials and their effects on the battery performances for the realization batteries in stationary EES applications.

In conclusion, large scale batteries have been gradually implemented in stationary EES application area. However, the increased use of the batteries in EES system has been limited by their high cost and unsatisfactory electrochemical performances. If new battery systems or further development of present battery systems can be introduced with suitable characteristics for large scale EES system, it will bring society one step closer to achieving successful stationary energy storage technology for a renewable energy system.

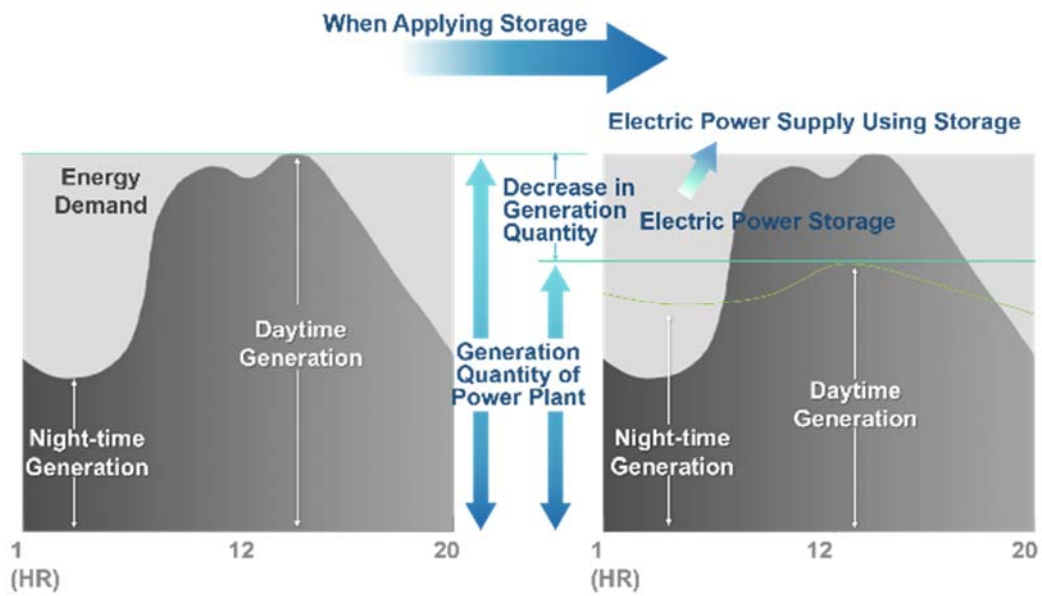


Figure 1. The description of load leveling with the adoption of electric energy storage system.

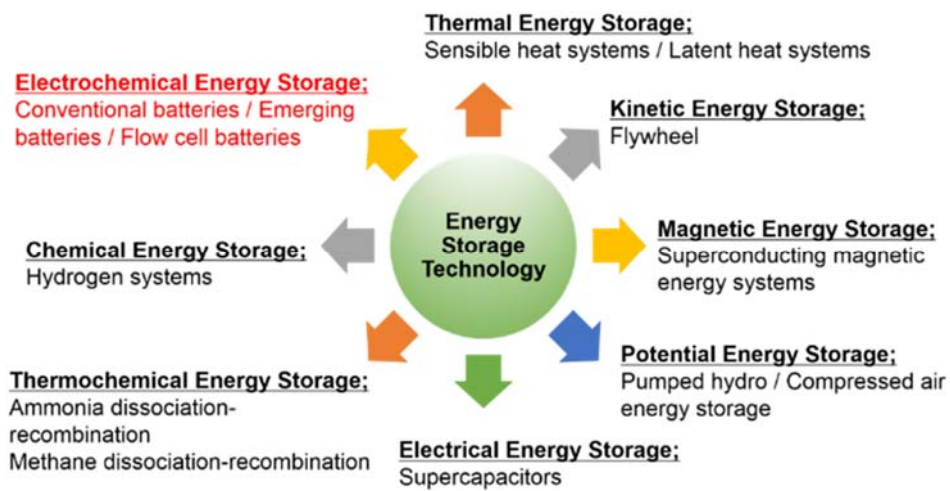


Figure 2. Classification of electrical energy storage for large scale stationary applications

Table 1. The characteristics of potential and kinetic energy storage system: pumped hydro, compressed air and flywheel. Ref. [9, 10, 18]

Energy storage technology	Power rating (MW)	Discharging duration (h)	Efficiency (%)	Capital cost (\$/kWh)	Cycle cost output (\$/kWh)	Life (yrs.)	Maturity	Safety issues	Limitations
Pumped hydro	10's MW to GW	>8	65-80	80-200	0.001-0.02	30	Commercial	Exclusion area	Location limited / long lead-time (>10 yrs.)
Compressed air	100's MW to GW	0.1-15	60-79	50-110	0.03-0.06	30	Demonstration stage with limited commercial	Pressure vessels	Location limited / need gas turbine system / contaminant emission
Flywheel	1-100kW	0.1-1	>90	300-5000	0.05-0.4	20	Commercial	Containment	Low energy density and efficiency / high initial cost / high-self discharge

Table 2. The chemistry and characteristics of developed electrochemical energy storage system. Ref. [18, 151]

Battery system	Redox reaction		Cell voltage (V)	Efficiency (%)	Lifetime (yrs.)	Cycle life (yrs.)	Energy and power density		Energy and power cost		Limitation
	Positive electrode	Negative electrode					Wh/kg	W/kg	\$/kWh	S/kW	
Lead-acid	PbO ₂	Pb	2.1	>70%	3-12	500-1000	30-50	75-300	200-400	300-600	Limited cycle-life Toxic
Na-S	S	Na	~2	75-90	5-15	2500	150-240	150-230	300-500	1000-3000	High operating temperature
Li-ion	LiCoO ₂	C ₆	3.6	85-98	5-15	1000-10000	75-200	150-315	500-2500	175-4000	High cost
Redox flow (all V)	V ⁴⁺ /V ⁵⁺	V ²⁺ /V ³⁺	1.26	75-85	10	12000	10-30	-	150-1000	600-1500	Low energy density

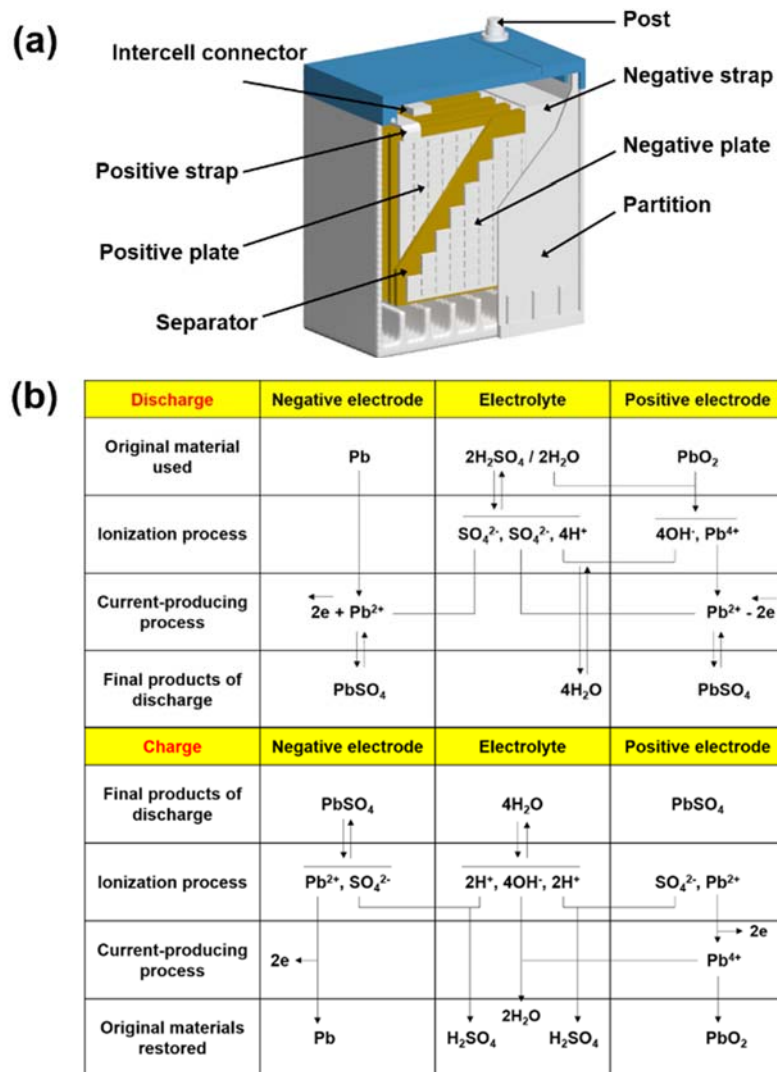


Figure 3. (a) Configuration of lead-acid battery, and (b) Graphical representation of discharge-charge reaction mechanism. Redrawn based on ref. [21]

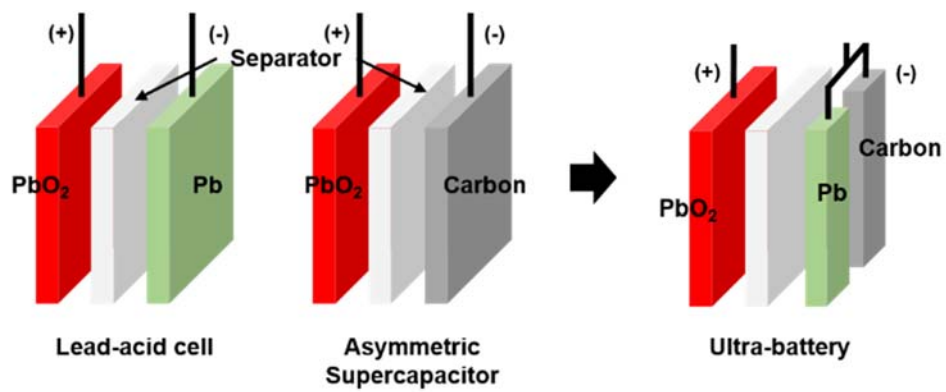


Figure 4. Schematic view of the ultra-battery consisting of lead-acid cell and asymmetric supercapacitor. Redrawn based on ref. [35]

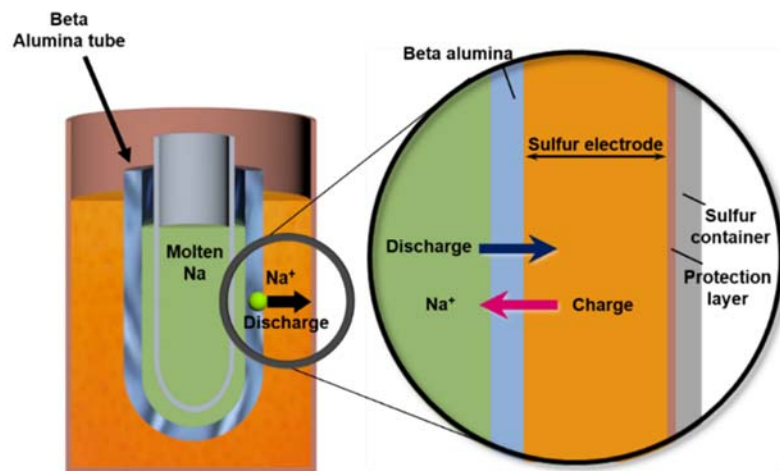


Figure 5. Schematic illustration of tubular Na-S battery with the detailed structure. Redrawn based on ref. [9]

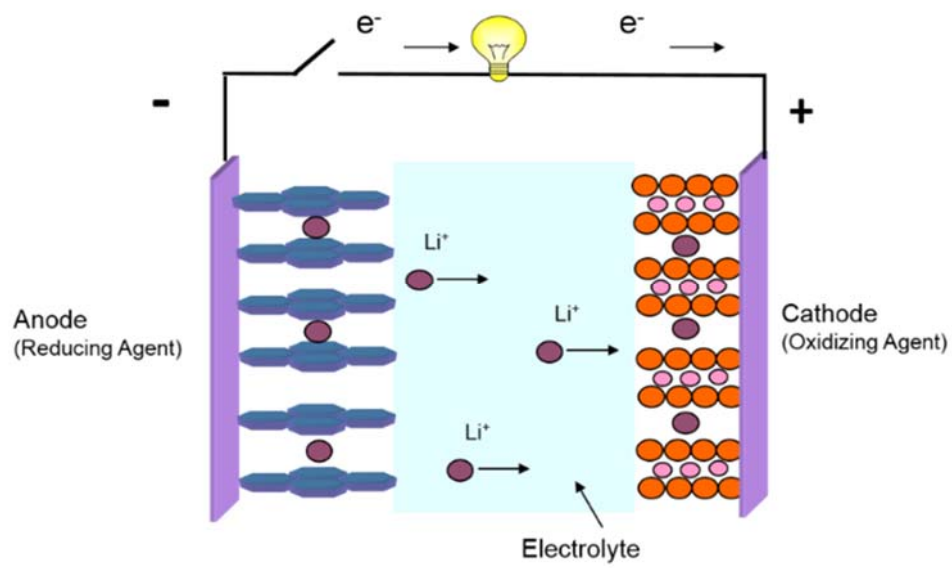


Figure 6. The schematic view of Li-ion battery consisting of intercalation compounds during discharge.

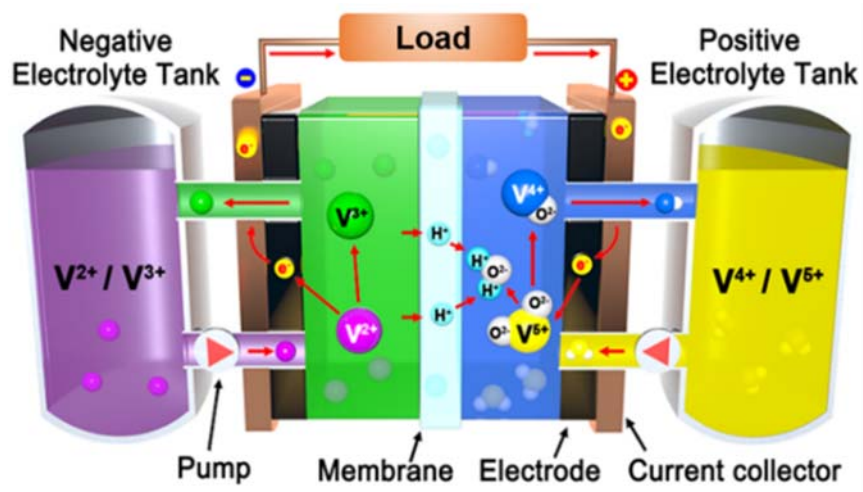


Figure 7. Schematic view of all vanadium redox flow battery during discharge.

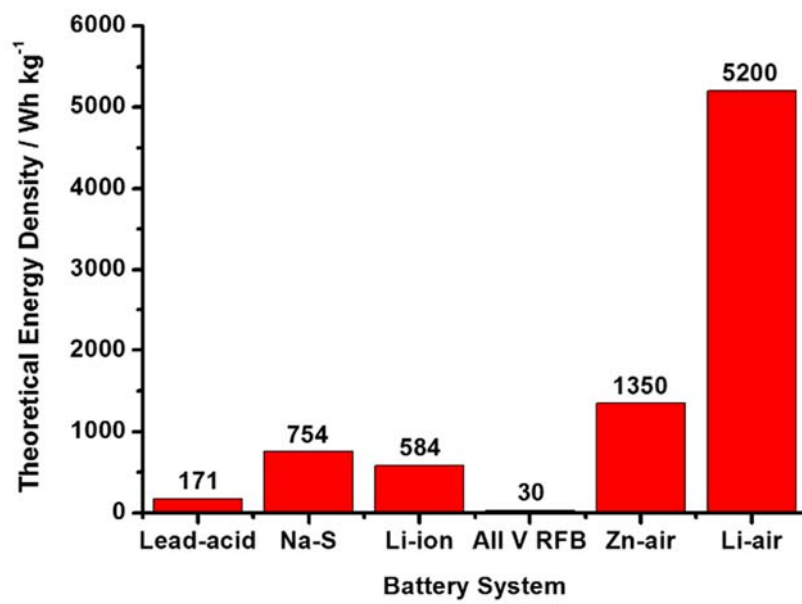


Figure 8. The comparison of theoretical specific energy density of electrochemical energy storage system.

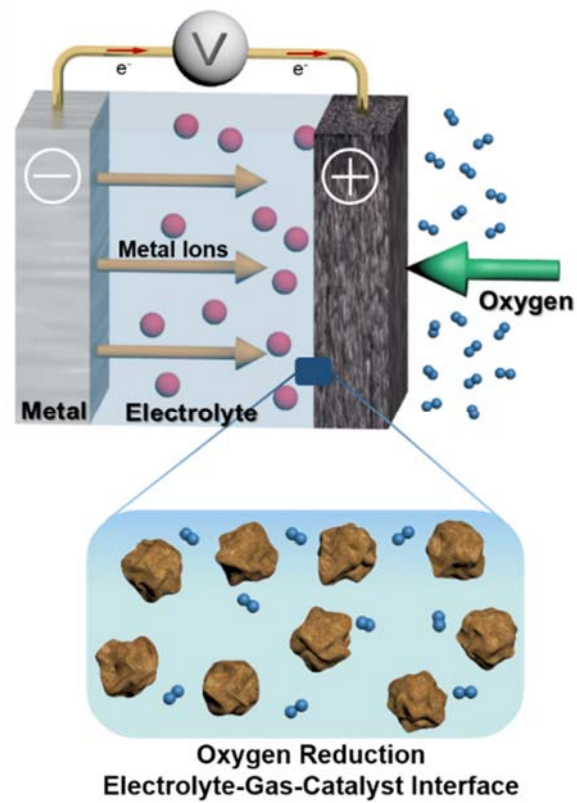


Figure 9. The general description of metal-air battery system with oxygen reduction reaction phase.

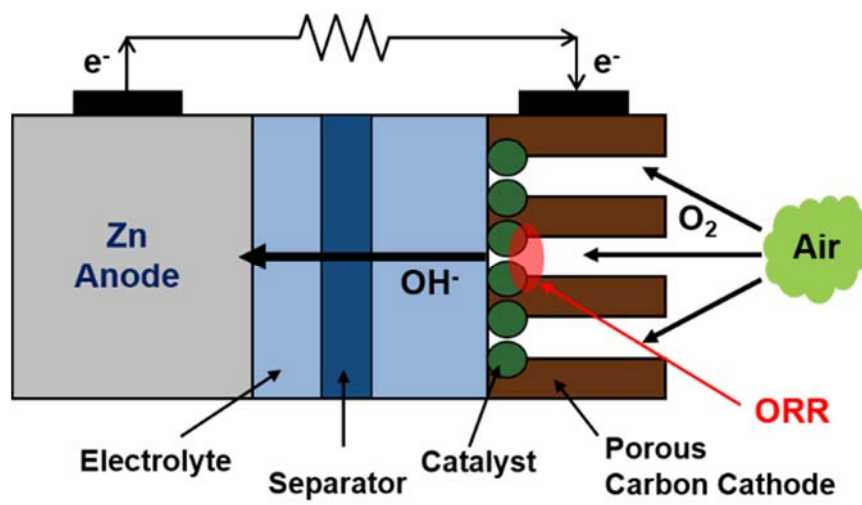


Figure 10. The detailed illustration of zinc-air battery.

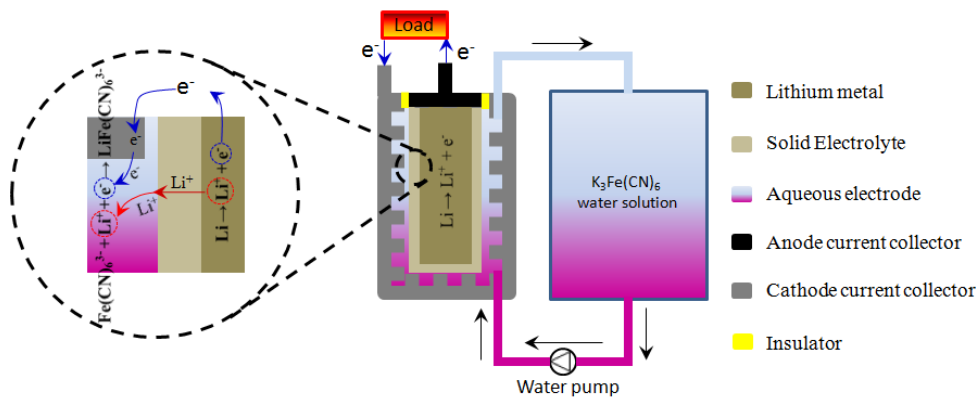


Figure 11. The configuration of aqueous lithium flow battery and the electrochemical reaction process.

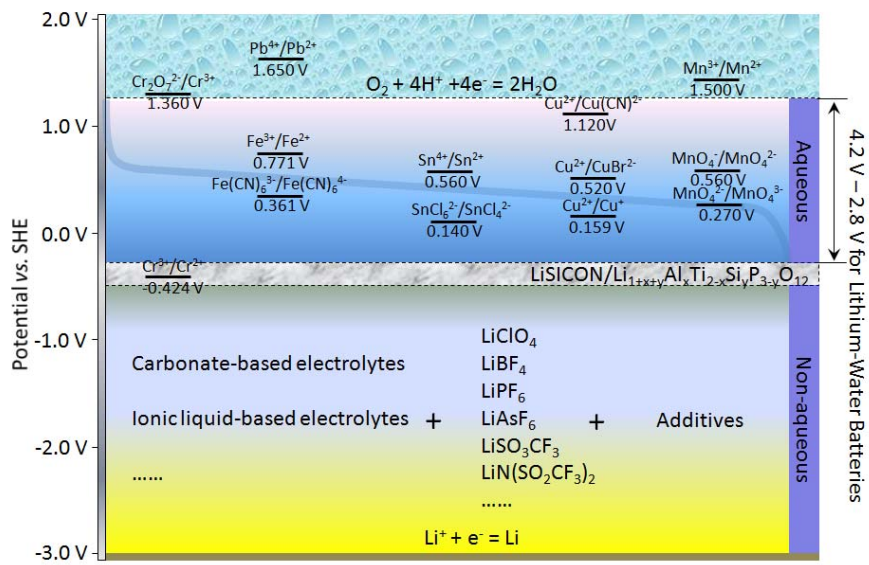


Figure 12. Various candidates of cathode in aqueous lithium flow battery.

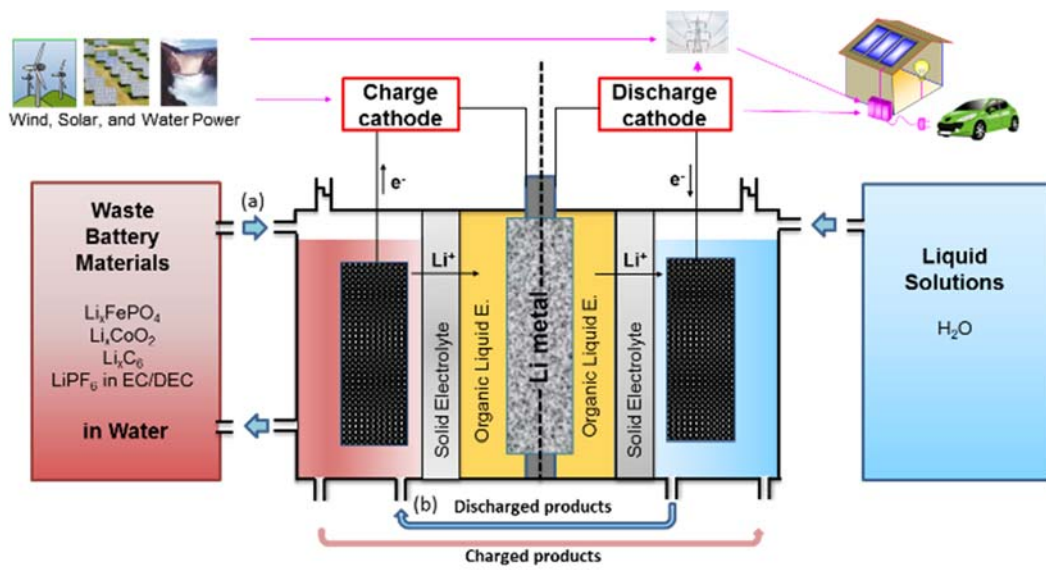


Figure 13. Schematic view of waste Li-liquid flow battery consisting of waste battery material, Li metal, and water.

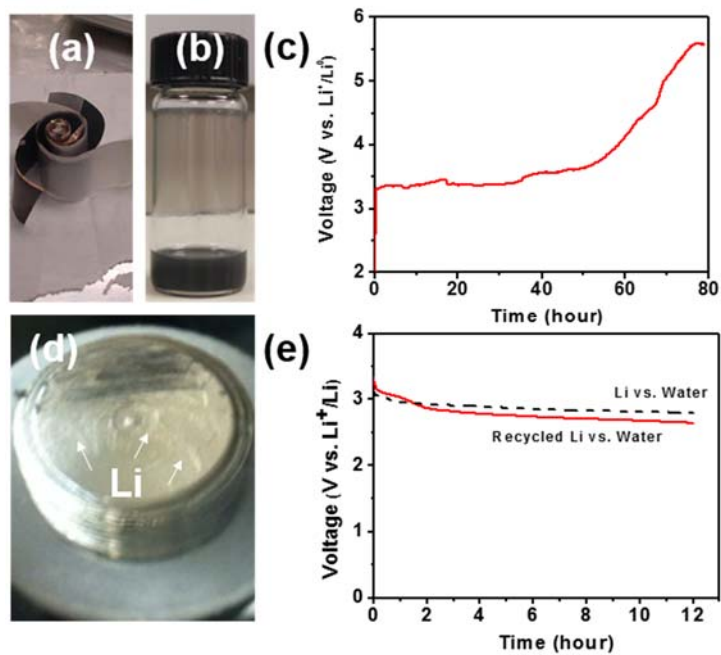


Figure 14. (a) Disassembled waste Li-ion battery, (b) Waste battery materials with Li_xC_6 , Li_xFePO_4 , and LiPF_6 in EC/DEC, (c) Charge voltage curve for Li metal harvest from liquid solution with waste materials, (d) Li metal on surface of stainless steel after harvest process of Li, and (e) The comparison of discharge curve between pure Li metal and harvested Li from waste Li-ion battery when using pure DI water as cathode.

Reference

1. Deepwater Horizon Accident and Response. <http://www.bp.com/en/global/corporate/gulf-of-mexico-restoration/deepwater-horizon-accident-and-response.html>.
2. Fukushima Accident. <http://www.world-nuclear.org/info/safety-and-security/safety-of-plants/fukushima-accident/>.
3. Greenhouse Gas Emissions. <http://www.epa.gov/climatechange/ghgemissions/>.
4. Chourabi, H.; Taewoo, N.; Walker, S.; Gil-Garcia, J. R.; Mellouli, S.; Nahon, K.; Pardo, T. A.; Scholl, H. J. In *Understanding Smart Cities: An Integrative Framework*, System Science (HICSS), 2012 45th Hawaii International Conference on, 4-7 Jan. 2012; **2012**; pp 2289-2297.
5. Ahmed, N. A.; Miyatake, M.; Al-Othman, A. K., Power fluctuations suppression of stand-alone hybrid generation combining solar photovoltaic/wind turbine and fuel cell systems. *Energ. Convers. Manage.* **2008**, *49* (10), 2711-2719.
6. Paul Denholm, E. E., Brendan Kirby, and Michael Milligan, The Role of Energy Storage with Renewable Electricity Generation. **2010**.
7. Whittingham, M. S., Materials Challenges Facing Electrical Energy Storage. *MRS Bull.* **2008**, *33* (04), 411-419.
8. Ibrahim, H.; Ilinca, A.; Perron, J., Energy storage systems—Characteristics and comparisons. *Renew. Sust. Energy Rev.* **2008**, *12* (5), 1221-1250.
9. Dunn, B.; Kamath, H.; Tarascon, J.-M., Electrical Energy Storage for the Grid: A Battery of Choices. *Science* **2011**, *334* (6058), 928-935.
10. Chen, H.; Cong, T. N.; Yang, W.; Tan, C.; Li, Y.; Ding, Y., Progress in electrical energy storage system: A critical review. *Prog. Nat. Sci.* **2009**, *19* (3), 291-312.
11. Bueno, C.; Carta, J. A., Wind powered pumped hydro storage systems, a means of increasing the penetration of renewable energy in the Canary Islands. *Renew. Sust. Energy Rev.* **2006**, *10* (4), 312-340.
12. van der Linden, S., Bulk energy storage potential in the USA, current developments and future prospects. *Energy* **2006**, *31* (15), 3446-3457.
13. Kondoh, J.; Ishii, I.; Yamaguchi, H.; Murata, A.; Otani, K.; Sakuta, K.; Higuchi, N.; Sekine, S.; Kamimoto, M., Electrical energy storage systems for energy networks. *Energ. Convers. Manage.* **2000**, *41* (17), 1863-1874.
14. Ribeiro, P. F.; Johnson, B. K.; Crow, M. L.; Arsoy, A.; Liu, Y., Energy storage systems for advanced power applications. *P. IEEE* **2001**, *89* (12), 1744-1756.
15. Denholm, P.; Kulcinski, G. L., Life cycle energy requirements and greenhouse gas emissions from large scale energy storage systems. *Energ. Convers. Manage.* **2004**, *45* (13-14), 2153-2172.

16. Denholm, P.; Holloway, T., Improved Accounting of Emissions from Utility Energy Storage System Operation. *Environ. Sci. Technol.* **2005**, *39* (23), 9016-9022.
17. Bolund, B.; Bernhoff, H.; Leijon, M., Flywheel energy and power storage systems. *Renew Sust. Energy Rev.* **2007**, *11* (2), 235-258.
18. Skyllas-Kazacos, M.; Chakrabarti, M. H.; Hajimolana, S. A.; Mjalli, F. S.; Saleem, M., Progress in Flow Battery Research and Development. *J. Electrochem. Soc.* **2011**, *158* (8), R55-R79.
19. Energy Storage Industry Grows To Intergrate Wind and Solar. <http://www.renewableenergyworld.com/rea/news/article/2011/08/energy-storage-industry-grows-to-integrate-wind-solar>.
20. Winter, M.; Brodd, R. J., What Are Batteries, Fuel Cells, and Supercapacitors? *Chem. Rev.* **2004**, *104* (10), 4245-4270.
21. Salkind, A. J.; Cannone, A. G.; Trumbure, F. A. In Handbook of Batteries, 3rd ed.; Linden, D.; Reddy, T. B., Ed.; McGraw-Hill: New York, **2002**; p 23.1-2
22. Salkind, A. J.; Hammel, R. O.; Cannone, A. G.; Trumbure, F. A. In Handbook of Batteries, 3rd ed.; Linden, D.; Reddy, T. B., Ed.; McGraw-Hill: New York, **2002**; p 24.1.
23. Perrin, M.; Saint-Drenan, Y. M.; Mattera, F.; Malbranche, P., Lead–acid batteries in stationary applications: competitors and new markets for large penetration of renewable energies. *J. Power Sources* **2005**, *144* (2), 402-410.
24. Parker, C. D., Lead–acid battery energy-storage systems for electricity supply networks. *J. Power Sources* **2001**, *100* (1–2), 18-28.
25. Treptow, R. S., The Lead-Acid Battery: Its Voltage in Theory and in Practice. *J. Chem. Educ.* **2002**, *79* (3), 334.
26. C. Mantell, Batteries and Energy Systems, 2d ed., McGraw-Hill, New York, **1983**.
27. D. Pavlov. Lead-Acid Batteries: Science and Technology. Amsterdam: Elsevier; **2011**, p. 3-28.
28. Lam, L. T.; Haigh, N. P.; Phyland, C. G.; Urban, A. J., Failure mode of valve-regulated lead-acid batteries under high-rate partial-state-of-charge operation. *J. Power Sources* **2004**, *133* (1), 126-134.
29. Lam, L. T.; Haigh, N. P.; Phyland, C. G.; Huynh, T. D., Novel technique to ensure battery reliability in 42-V PowerNets for new-generation automobiles. *J. Power Sources* **2005**, *144* (2), 552-559.
30. Chih-Chiang, H.; Meng-Yu, L. In *A study of charging control of lead-acid battery for electric vehicles*, Industrial Electronics, 2000. ISIE 2000. Proceedings of the 2000 IEEE International Symposium on, 2000; **2000**; pp 135-140 vol.1.
31. Moseley, P. T.; Nelson, R. F.; Hollenkamp, A. F., The role of carbon in valve-regulated lead–acid battery technology. *J. Power Sources* **2006**, *157* (1), 3-10.

32. Shiomi, M.; Funato, T.; Nakamura, K.; Takahashi, K.; Tsubota, M., Effects of carbon in negative plates on cycle-life performance of valve-regulated lead/acid batteries. *J. Power Sources* **1997**, *64* (1–2), 147-152.
33. Nakamura, K.; Shiomi, M.; Takahashi, K.; Tsubota, M., Failure modes of valve-regulated lead/acid batteries. *J. Power Sources* **1996**, *59* (1–2), 153-157.
34. Razoumov, S.; Klementov, A.; Litvinenko, S.; Beliakov, A. U.S. Patent 6,222,723, 2001.
35. Cooper, A.; Furakawa, J.; Lam, L.; Kellaway, M., The UltraBattery—A new battery design for a new beginning in hybrid electric vehicle energy storage. *J. Power Sources* **2009**, *188* (2), 642-649.
36. J. T. Kummer, N. Weber, U.S. Patent 1968, 3413150.
37. Dufo-López, R.; Bernal-Agustín, J. L.; Domínguez-Navarro, J. A., Generation management using batteries in wind farms: Economical and technical analysis for Spain. *Energ. Policy* **2009**, *37* (1), 126-139.
38. Yang, Z.; Zhang, J.; Kintner-Meyer, M. C. W.; Lu, X.; Choi, D.; Lemmon, J. P.; Liu, J., Electrochemical Energy Storage for Green Grid. *Chem. Rev.* **2011**, pp 3577-3613.
39. Jeffrey W, Braithwaite, William L Auxer. A. In Handbook of batteries, 3rd ed.; Linden, D.; Reddy, T. B., Ed.; McGraw-Hill: New York, **2002**; p/ 40.2.
40. Oshima, T.; Kajita, M.; Okuno, A., Development of Sodium-Sulfur Batteries. *Int. J. Appl. Ceram. Tec.* **2004**, *1* (3), 269-276.
41. Virkar, A. V.; Miller, G. R.; Gordon, R. S., Resistivity-Microstructure Relations in Lithia-Stabilized Polycrystalline β'' -Alumina. *J. Am. Ceram. Soc.* **1978**, *61* (5-6), 250-252.
42. Youngblood, G. E.; Miller, G. R.; Gordon, R. S., Relative Effects of Phase Conversion and Grain Size on Sodium Ion Conduction in Polycrystalline, Lithia-Stabilized β -Alumina. *J. Am. Ceram. Soc.* **1978**, *61* (1-2), 86-87.
43. J. L. Sudworth, A. R. Tilley, The Sodium Sulphur Battery, Chapman and Hall Ltd., New York **1985**.
44. NAS Battery Fire Incident and Response. <http://www.ngk.co.jp/english/announce/>.
45. Song, S.; Wen, Z.; Zhang, Q.; Liu, Y., A novel Bi-doped borosilicate glass as sealant for sodium sulfur battery. Part 1: Thermophysical characteristics and structure. *J. Power Sources* **2010**, *195* (1), 384-388.
46. Song, S.; Wen, Z.; Liu, Y.; Lin, J.; Xu, X.; Zhang, Q., New glass-ceramic sealants for Na/S battery. *J. Solid State Electrochem.* **2010**, *14* (9), 1735-1740.
47. Song, S.; Wen, Z.; Liu, Y., The effect of substitution of Bi₂O₃ for alkali oxides on thermal properties, structure and wetting behavior of the borosilicate glass. *Mater. Lett.* **2010**, *64* (9), 1025-1027.
48. Tischer, R. P. The Sulphur Electrode; Academic Press: New York, **1983**.
49. Wen, Z.; Hu, Y.; Wu, X.; Han, J.; Gu, Z., Main Challenges for High Performance NAS Battery: Materials and Interfaces. *Adv. Funct. Mater.* **2013**, *23* (8), 1005-1018.

50. Park, C.-W.; Ryu, H.-S.; Kim, K.-W.; Ahn, J.-H.; Lee, J.-Y.; Ahn, H.-J., Discharge properties of all-solid sodium–sulfur battery using poly (ethylene oxide) electrolyte. *J. Power Sources* **2007**, *165* (1), 450-454.
51. Park, C.-W.; Ahn, J.-H.; Ryu, H.-S.; Kim, K.-W.; Ahn, H.-J., Room-Temperature Solid-State Sodium/Sulfur Battery. *Electrochem. Solid St.* **2006**, *9* (3), A123-A125.
52. Kim, J.-S.; Ahn, H.-J.; Kim, I.-P.; Kim, K.-W.; Ahn, J.-H.; Park, C.-W.; Ryu, H.-S., The short-term cycling properties of Na/PVdF/S battery at ambient temperature. *J. Solid State Electrochem.* **2008**, *12* (7-8), 861-865.
53. Wang, J.; Yang, J.; Nuli, Y.; Holze, R., Room temperature Na/S batteries with sulfur composite cathode materials. *Electrochem. Commun.* **2007**, *9* (1), 31-34.
54. Ryu, H.; Kim, T.; Kim, K.; Ahn, J.-H.; Nam, T.; Wang, G.; Ahn, H.-J., Discharge reaction mechanism of room-temperature sodium–sulfur battery with tetra ethylene glycol dimethyl ether liquid electrolyte. *J. Power Sources* **2011**, *196* (11), 5186-5190.
55. Lu, X.; Kirby, B. W.; Xu, W.; Li, G.; Kim, J. Y.; Lemmon, J. P.; Sprenkle, V. L.; Yang, Z., Advanced intermediate-temperature Na-S battery. *Energ. Environ. Sci.* **2013**, *6* (1), 299-306.
56. Choi, N.-S.; Chen, Z.; Freunberger, S. A.; Ji, X.; Sun, Y.-K.; Amine, K.; Yushin, G.; Nazar, L. F.; Cho, J.; Bruce, P. G., Challenges Facing Lithium Batteries and Electrical Double-Layer Capacitors. *Angew. Chem. Int. Ed.* **2012**, *51* (40), 9994-10024.
57. Tarascon, J. M.; Armand, M., Issues and challenges facing rechargeable lithium batteries. *Nature* **2001**, *414* (6861), 359-367.
58. Grant ME. In Handbook of batteries, 3rd ed.; Linden, D.; Reddy, T. B., Ed.; McGraw-Hill: New York, **2002**; p. 35.1.
59. Howell, D. DOE Progress Report for Energy Storage Research and Development; US Department of Energy: Washington, DC, **2008**.
60. Gaines, L.; Cuenca, R. Costs of Lithium-Ion-Batteries for Vehicles; Argon National Laboratory: Argonne, IL, **2000**.
61. Viswanathan, V. V.; Choi, D.; Wang, D.; Xu, W.; Towne, S.; Williford, R. E.; Zhang, J.-G.; Liu, J.; Yang, Z., Effect of entropy change of lithium intercalation in cathodes and anodes on Li-ion battery thermal management. *J. Power Sources* **2010**, *195* (11), 3720-3729.
62. Wang, W.; Choi, D.; Yang, Z., Li-Ion Battery with LiFePO₄ Cathode and Li₄Ti₅O₁₂ Anode for Stationary Energy Storage. *Metall. Mater. Trans. A* **2013**, *44* (1), 21-25.
63. Jaiswal, A.; Horne, C. R.; Chang, O.; Zhang, W.; Kong, W.; Wang, E.; Chern, T.; Doeff, M. M., Nanoscale LiFePO₄ and Li₄Ti₅O₁₂ for High Rate Li-Ion Batteries. *J. Electrochem. Soc.* **2009**, *156* (12), A1041-A1046.

64. Zaghib, K.; Dontigny, M.; Guerfi, A.; Charest, P.; Rodrigues, I.; Mauger, A.; Julien, C. M., Safe and fast-charging Li-ion battery with long shelf life for power applications. *J. Power Sources* **2011**, *196* (8), 3949-3954.
65. Wang, Y.; Wang, Y.; Hosono, E.; Wang, K.; Zhou, H., The Design of a LiFePO₄/Carbon Nanocomposite With a Core–Shell Structure and Its Synthesis by an In Situ Polymerization Restriction Method. *Angew. Chem. Int. Ed.* **2008**, *47* (39), 7461-7465.
66. Sun, C.; Rajasekhara, S.; Goodenough, J. B.; Zhou, F., Monodisperse Porous LiFePO₄ Microspheres for a High Power Li-Ion Battery Cathode. *J. Am. Chem. Soc.* **2011**, *133* (7), 2132-2135.
67. Caballero, A.; Cruz-Yusta, M.; Morales, J.; Santos-Peña, J.; Rodríguez-Castellón, E., A New and Fast Synthesis of Nanosized LiFePO₄ Electrode Materials. *Eur. J. Inorg. Chem.* **2006**, *2006* (9), 1758-1764.
68. Gu, H.-B.; Jun, D.-K.; Park, G.-C.; Jin, B.; Jin, E. M., Nanosized LiFePO₄ Cathode Materials for Lithium Ion Batteries. *J. Nanosci. Nanotechnol.* **2007**, *7* (11), 3980-3984.
69. S. Eckroad, Handbook of Energy Storage for Transmission or Distribution Applications, Electric Power Research Institute Report 1007189, California, USA, **2002**.
70. Leung, P.; Li, X.; Ponce de Leon, C.; Berlouis, L.; Low, C. T. J.; Walsh, F. C., Progress in redox flow batteries, remaining challenges and their applications in energy storage. *RSC Adv.* **2012**, *2* (27), 10125-10156.
71. Kazacos, M.; Skyllas-Kazacos, M., Performance Characteristics of Carbon Plastic Electrodes in the All-Vanadium Redox Cell. *J. Electrochem. Soc.* **1989**, *136* (9), 2759-2760.
72. Kazacos, M.; Cheng, M.; Skyllas-Kazacos, M., Vanadium redox cell electrolyte optimization studies. *J. Appl. Electrochem.* **1990**, *20* (3), 463-467.
73. Skyllas-Kazacos, M.; Menictas, C.; Kazacos, M., Thermal Stability of Concentrated V(V) Electrolytes in the Vanadium Redox Cell. *J. Electrochem. Soc.* **1996**, *143* (4), L86-L88.
74. Rahman, F.; Skyllas-Kazacos, M., Solubility of vanadyl sulfate in concentrated sulfuric acid solutions. *J. Power Sources* **1998**, *72* (2), 105-110.
75. Skyllas-Kazacos, M.; Peng, C.; Cheng, M., Evaluation of Precipitation Inhibitors for Supersaturated Vanadyl Electrolytes for the Vanadium Redox Battery. *Electrochem. Solid St.* **1999**, *2* (3), 121-122.
76. Rahman, F.; Skyllas-Kazacos, M., Vanadium redox battery: Positive half-cell electrolyte studies. *J. Power Sources* **2009**, *189* (2), 1212-1219.
77. Rychcik, M.; Skyllas-Kazacos, M., Evaluation of electrode materials for vanadium redox cell. *J. Power Sources* **1987**, *19* (1), 45-54.
78. Li, X.; Zhang, H.; Mai, Z.; Zhang, H.; Vankelecom, I., Ion exchange membranes for vanadium redox flow battery (VRB) applications. *Energ. Environ. Sci.* **2011**, *4* (4), 1147-1160.

79. Sun, B.; Skyllas-Kazacos, M., Modification of graphite electrode materials for vanadium redox flow battery application—I. Thermal treatment. *Electrochim. Acta* **1992**, *37* (7), 1253-1260.
80. Zhu, H. Q.; Zhang, Y. M.; Yue, L.; Li, W. S.; Li, G. L.; Shu, D.; Chen, H. Y., Graphite-carbon nanotube composite electrodes for all vanadium redox flow battery. *J. Power Sources* **2008**, *184* (2), 637-640.
81. Shao, Y.; Wang, X.; Engelhard, M.; Wang, C.; Dai, S.; Liu, J.; Yang, Z.; Lin, Y., Nitrogen-doped mesoporous carbon for energy storage in vanadium redox flow batteries. *J. Power Sources* **2010**, *195* (13), 4375-4379.
82. Park, M.; Jung, Y.-j.; Kim, J.; Lee, H. i.; Cho, J., Synergistic Effect of Carbon Nanofiber/Nanotube Composite Catalyst on Carbon Felt Electrode for High-Performance All-Vanadium Redox Flow Battery. *Nano Lett.* **2013**, *13* (10), 4833-4839.
83. Xing, F.; Zhang, H.; Ma, X., Shunt current loss of the vanadium redox flow battery. *J Power Sources* **2011**, *196* (24), 10753-10757.
84. Linden, D.; Reddy, T. B., Handbook of Batteries 3rd ed., McGraw-Hill: New York, **2002**.
85. K. Kinoshita, Electrochemical Oxygen Technology, Wiley, New York, **1992**.
86. Ian Kowalczyk, J. R., Mark Salomon, Li-air batteries: A classic example of limitations owing to solubilities. *Pure Appl. Chem.* **2007**, *79*, 851-860
87. McCloskey, B. D.; Bethune, D. S.; Shelby, R. M.; Girishkumar, G.; Luntz, A. C., Solvents' Critical Role in Nonaqueous Lithium-Oxygen Battery Electrochemistry. *J. Phys. Chem. Lett.* **2011**, *2* (10), 1161-1166.
88. Chakkaravarthy, C.; Waheed, A. K. A.; Udupa, H. V. K., Zinc-air alkaline batteries - A review. *J. Power Sources* **1981**, *6* (3), 203-228.
89. Lee, C. W.; Sathiyarayanan, K.; Eom, S. W.; Kim, H. S.; Yun, M. S., Novel electrochemical behavior of zinc anodes in zinc/air batteries in the presence of additives. *J. Power Sources* **2006**, *159* (2), 1474-1477.
90. Goldstein, J.; Brown, I.; Koretz, B., New developments in the Electric Fuel Ltd. zinc/air system. *J. Power Sources* **1999**, *80* (1-2), 171-179.
91. Sapkota, P.; Kim, H., Zinc-air fuel cell, a potential candidate for alternative energy. *J. Ind. Eng. Chem.* **2009**, *15* (4), 445-450.
92. Drillet, J.-F.; Adam, M.; Barg, S.; Herter, A.; Koch, D.; Schmidt, V.; Wilhelm, M., Development of a Novel Zinc/Air Fuel Cell with a Zn Foam Anode, a PVA/KOH Membrane and a MnO₂/SiOC-Based Air Cathode. *ECS Trans.* **2010**, *28* (32), 13-24.
93. Toussaint, G.; Stevens, P.; Akrou, L.; Rouget, R.; Fourgeot, F., Development of a Rechargeable Zinc-Air Battery. *ECS Trans.* **2010**, *28* (32), 25-34.
94. Shaigan, N.; Qu, W.; Takeda, T., Morphology Control of Electrodeposited Zinc from Alkaline Zincate Solutions for Rechargeable Zinc Air Batteries. *ECS Trans.* **2010**, *28* (32), 35-44.

95. Yang, C.-C.; Lin, S.-J., Improvement of high-rate capability of alkaline Zn–MnO₂ battery. *J. Power Sources* **2002**, *112* (1), 174-183.
96. Zhang, X. G., Fibrous zinc anodes for high power batteries. *J. Power Sources* **2006**, *163* (1), 591-597.
97. Devyatkina, T. I.; Gun'ko, Y. L.; Mikhalenko, M. G., Development of Ways To Diminish Corrosion of Zinc Electrode. *Russ. J. Appl. Chem.* **2001**, *74* (7), 1122-1125.
98. Müller, S.; Holzer, F.; Haas, O., Optimized zinc electrode for the rechargeable zinc–air battery. *J. Appl. Electrochem.* **1998**, *28* (9), 895-898.
99. Lee, C. W.; Sathiyarayanan, K.; Eom, S. W.; Yun, M. S., Novel alloys to improve the electrochemical behavior of zinc anodes for zinc/air battery. *J. Power Sources* **2006**, *160* (2), 1436-1441.
100. Cho, Y.-D.; Fey, G. T.-K., Surface treatment of zinc anodes to improve discharge capacity and suppress hydrogen gas evolution. *J. Power Sources* **2008**, *184* (2), 610-616.
101. Zhu, L.; Zhang, H.; Li, W.; Liu, H., New modification procedure of zinc powder in neodymium nitrate solution for improving the electrochemical properties of alkaline zinc electrodes. *J. Phys. Chem. Solids* **2009**, *70* (1), 45-54.
102. Appleby, A. J.; Jacquier, M., The C.G.E. circulating zinc/air battery: A practical vehicle power source. *J. Power Sources* **1976**, *1* (1), 17-34.
103. Fauvarque, J. F.; Guinot, S.; Bouziri, N.; Salmon, E.; Penneau, J. F., Alkaline poly(ethylene oxide) solid polymer electrolytes. Application to nickel secondary batteries. *Electrochim. Acta* **1995**, *40* (13–14), 2449-2453.
104. Lewandowski, A.; Skorupska, K.; Malinska, J., Novel poly(vinyl alcohol)–KOH–H₂O alkaline polymer electrolyte. *Solid State Ionics* **2000**, *133* (3–4), 265-271.
105. Saputra, H.; Othman, R.; Sutjipto, A. G. E.; Muhida, R., MCM-41 as a new separator material for electrochemical cell: Application in zinc–air system. *J. Membrane Sci.* **2011**, *367* (1–2), 152-157.
106. Mohamad, A. A., Zn/gelled 6M KOH/O₂ zinc–air battery. *J. Power Sources* **2006**, *159* (1), 752-757.
107. Jörissen, L., Bifunctional oxygen/air electrodes. *J. Power Sources* **2006**, *155* (1), 23-32.
108. Cheng, H.-H.; Tan, C.-S., Reduction of CO₂ concentration in a zinc/air battery by absorption in a rotating packed bed. *J. Power Sources* **2006**, *162* (2), 1431-1436.
109. Deiss, E.; Holzer, F.; Haas, O., Modeling of an electrically rechargeable alkaline Zn–air battery. *Electrochim. Acta* **2002**, *47* (25), 3995-4010.
110. Müller, S.; Striebel, K.; Haas, O., La_{0.6}Ca_{0.4}CoO₃: a stable and powerful catalyst for bifunctional air electrodes. *Electrochim. Acta* **1994**, *39* (11–12), 1661-1668.

111. Lee, J.-S.; Lee, T.; Song, H.-K.; Cho, J.; Kim, B.-S., Ionic liquid modified graphene nanosheets anchoring manganese oxide nanoparticles as efficient electrocatalysts for Zn-air batteries. *Energ. Environ. Sci.* **2011**, *4* (10), 4148-4154.
112. Gara, M.; Compton, R. G., Activity of carbon electrodes towards oxygen reduction in acid: A comparative study. *New J. Chem.* **2011**, *35* (11), 2647-2652.
113. Wang, X.; Lee, J. S.; Zhu, Q.; Liu, J.; Wang, Y.; Dai, S., Ammonia-Treated Ordered Mesoporous Carbons as Catalytic Materials for Oxygen Reduction Reaction. *Chem. Mater.* **2010**, *22* (7), 2178-2180.
114. Yang, W.; Fellingner, T.-P.; Antonietti, M., Efficient Metal-Free Oxygen Reduction in Alkaline Medium on High-Surface-Area Mesoporous Nitrogen-Doped Carbons Made from Ionic Liquids and Nucleobases. *J. Am. Chem. Soc.* **2010**, *133* (2), 206-209.
115. Shanmugam, S.; Osaka, T., Efficient electrocatalytic oxygen reduction over metal free-nitrogen doped carbon nanocapsules. *Chem. Commun.* **2011**, *47* (15), 4463-4465.
116. Kannan, R.; Bipinlal, U.; Kurungot, S.; Pillai, V. K., Enhanced electrocatalytic performance of functionalized carbon nanotube electrodes for oxygen reduction in proton exchange membrane fuel cells. *Phys. Chem. Chem. Phys.* **2011**, *13* (21), 10312-10317.
117. Kim, H.; Lee, K.; Woo, S. I.; Jung, Y., On the mechanism of enhanced oxygen reduction reaction in nitrogen-doped graphene nanoribbons. *Phys. Chem. Chem. Phys.* **2011**, *13* (39), 17505-17510.
118. Cao, R.; Thapa, R.; Kim, H.; Xu, X.; Gyu Kim, M.; Li, Q.; Park, N.; Liu, M.; Cho, J., Promotion of oxygen reduction by a bio-inspired tethered iron phthalocyanine carbon nanotube-based catalyst. *Nat. Commun.* **2013**, *4*.
119. Lee, J.-S.; Park, G. S.; Kim, S. T.; Liu, M.; Cho, J., A Highly Efficient Electrocatalyst for the Oxygen Reduction Reaction: N-Doped Ketjenblack Incorporated into Fe/Fe₃C-Functionalized Melamine Foam. *Angew. Chem. Int. Ed.* **2013**, *52* (3), 1026-1030.
120. Lee, J.-S.; Park, G. S.; Lee, H. I.; Kim, S. T.; Cao, R.; Liu, M.; Cho, J., Ketjenblack Carbon Supported Amorphous Manganese Oxides Nanowires as Highly Efficient Electrocatalyst for Oxygen Reduction Reaction in Alkaline Solutions. *Nano Lett.* **2011**, *11* (12), 5362-5366.
121. Wang, X.; Sebastian, P. J.; Smit, M. A.; Yang, H.; Gamboa, S. A., Studies on the oxygen reduction catalyst for zinc-air battery electrode. *J. Power Sources* **2003**, *124* (1), 278-284.
122. Neburchilov, V.; Wang, H.; Martin, J. J.; Qu, W., A review on air cathodes for zinc-air fuel cells. *J. Power Sources* **2010**, *195* (5), 1271-1291.
123. Wei, Z.; Huang, W.; Zhang, S.; Tan, J., Carbon-based air electrodes carrying MnO₂ in zinc-air batteries. *J. Power Sources* **2000**, *91* (2), 83-85.
124. Gorlin, Y.; Jaramillo, T. F., A Bifunctional Nonprecious Metal Catalyst for Oxygen Reduction and Water Oxidation. *J. Am. Chem. Soc.* **2010**, *132* (39), 13612-13614.

125. Chen, Z.; Yu, A.; Ahmed, R.; Wang, H.; Li, H.; Chen, Z., Manganese dioxide nanotube and nitrogen-doped carbon nanotube based composite bifunctional catalyst for rechargeable zinc-air battery. *Electrochim. Acta* **2012**, *69* (0), 295-300.
126. Huskinson, B.; Marshak, M. P.; Suh, C.; Er, S.; Gerhardt, M. R.; Galvin, C. J.; Chen, X.; Aspuru-Guzik, A.; Gordon, R. G.; Aziz, M. J., A metal-free organic-inorganic aqueous flow battery. *Nature* **2014**, *505* (7482), 195-198.
127. Song, Y.; Buettner, G. R., Thermodynamic and kinetic considerations for the reaction of semiquinone radicals to form superoxide and hydrogen peroxide. *Free Radical Bio. Med.* **2010**, *49* (6), 919-962.
128. Weber, A.; Mench, M.; Meyers, J.; Ross, P.; Gostick, J.; Liu, Q., Redox flow batteries: a review. *J. Appl. Electrochem.* **2011**, *41* (10), 1137-1164.
129. Matsuda, Y.; Tanaka, K.; Okada, M.; Takasu, Y.; Morita, M.; Matsumura-Inoue, T., A rechargeable redox battery utilizing ruthenium complexes with non-aqueous organic electrolyte. *J. Appl. Electrochem.* **1988**, *18* (6), 909-914.
130. Mun, J.; Lee, M.-J.; Park, J.-W.; Oh, D.-J.; Lee, D.-Y.; Doo, S.-G., Non-Aqueous Redox Flow Batteries with Nickel and Iron Tris(2,2-bipyridine) Complex Electrolyte. *Electrochem. Solid St.* **2012**, *15* (6), A80-A82.
131. Liu, Q.; Shinkle, A. A.; Li, Y.; Monroe, C. W.; Thompson, L. T.; Sleightholme, A. E. S., Non-aqueous chromium acetylacetonate electrolyte for redox flow batteries. *Electrochem. Commun.* **2010**, *12* (11), 1634-1637.
132. Liu, Q.; Sleightholme, A. E. S.; Shinkle, A. A.; Li, Y.; Thompson, L. T., Non-aqueous vanadium acetylacetonate electrolyte for redox flow batteries. *Electrochem. Commun.* **2009**, *11* (12), 2312-2315.
133. Zhang, D.; Liu, Q.; Shi, X.; Li, Y., Tetrabutylammonium hexafluorophosphate and 1-ethyl-3-methyl imidazolium hexafluorophosphate ionic liquids as supporting electrolytes for non-aqueous vanadium redox flow batteries. *J. Power Sources* **2012**, *203* (0), 201-205.
134. Shinkle, A. A.; Sleightholme, A. E. S.; Griffith, L. D.; Thompson, L. T.; Monroe, C. W., Degradation mechanisms in the non-aqueous vanadium acetylacetonate redox flow battery. *J. Power Sources* **2012**, *206* (0), 490-496.
135. Li, Z.; Li, S.; Liu, S.; Huang, K.; Fang, D.; Wang, F.; Peng, S., Electrochemical Properties of an All-Organic Redox Flow Battery Using 2,2,6,6-Tetramethyl-1-Piperidinyloxy and N-Methylphthalimide. *Electrochem. Solid St.* **2011**, *14* (12), A171-A173.
136. Brushett, F. R.; Vaughey, J. T.; Jansen, A. N., An All-Organic Non-aqueous Lithium-Ion Redox Flow Battery. *Adv. Energy Mater.* **2012**, *2* (11), 1390-1396.
137. Lu, Y.; Goodenough, J. B.; Kim, Y., Aqueous Cathode for Next-Generation Alkali-Ion Batteries. *J. Am. Chem. Soc.* **2011**, *133* (15), 5756-5759.

138. Speight, J. G. Lange's Handbook of Chemistry, 16th ed.; McGraw-Hill: New York, **2005**; pp 1.3801.395.
139. Lu, Y.; Goodenough, J. B., Rechargeable alkali-ion cathode-flow battery. *J. Mater. Chem.* **2011**, *21* (27), 10113-10117.
140. Wang, Y.; Wang, Y.; Zhou, H., A Li-Liquid Cathode Battery Based on a Hybrid Electrolyte. *ChemSusChem* **2011**, *4* (8), 1087-1090.
141. Musić, S.; Krehula, S.; Popović, S., Effect of HCl additions on forced hydrolysis of FeCl₃ solutions. *Mater. Lett.* **2004**, *58* (21), 2640-2645.
142. Wolf, R. H. H.; Wrischer, M.; Šipalo-Žuljević, J., Electron-microscopic investigation of the formation of colloidal beta FeOOH during slow hydrolysis of an aqueous ferric chloride solution at room temperature. *Colloid Polym. Sci.* **1967**, *215* (1), 57-60.
143. Asl, N. M.; Cheah, S. S.; Salim, J.; Kim, Y., Lithium-liquid battery: harvesting lithium from waste Li-ion batteries and discharging with water. *RSC Adv.* **2012**, *2* (14), 6094-6100.
144. Li, H.; Wang, Y.; Na, H.; Liu, H.; Zhou, H., Rechargeable Ni-Li Battery Integrated Aqueous/Nonaqueous System. *J. Am. Chem. Soc.* **2009**, *131* (42), 15098-15099.
145. Wang, Y.; Zhou, H., A new type rechargeable lithium battery based on a Cu-cathode. *Electrochem. Commun.* **2009**, *11* (9), 1834-1837.
146. Wang, Y.; Li, H.; He, P.; Zhou, H., Controllable Hydrogen Generation from Water. *ChemSusChem* **2010**, *3* (5), 571-574.
147. Zhang, T.; Imanishi, N.; Shimonishi, Y.; Hirano, A.; Xie, J.; Takeda, Y.; Yamamoto, O.; Sammes, N., Stability of a Water-Stable Lithium Metal Anode for a Lithium-Air Battery with Acetic Acid-Water Solutions. *J. Electrochem. Soc.* **2010**, *157* (2), A214-A218.
148. Zhang, T.; Imanishi, N.; Takeda, Y.; Yamamoto, O., Aqueous Lithium/Air Rechargeable Batteries. *Chem. Lett.* **2011**, *40* (7), 668-673.
149. Li, L.; Zhao, X.; Manthiram, A., A dual-electrolyte rechargeable Li-air battery with phosphate buffer catholyte. *Electrochem. Commun.* **2012**, *14* (1), 78-81.
150. Chun, J.; Chung, M.; Lee, J.; Kim, Y., Using waste Li ion batteries as cathodes in rechargeable Li-liquid batteries. *Phys. Chem. Chem. Phys.* **2013**, *15* (19), 7036-7040.
151. Thackeray, M. M.; Wolverton, C.; Isaacs, E. D., Electrical energy storage for transportation-approaching the limits of, and going beyond, lithium-ion batteries. *Energ. Environ. Sci.* **2012**, *5* (7), 7854-7863.

*Chapter I is submitted to "Progress in Energy Combustion Science" in 2014.

Chapter II

The Details in Li-ion Batteries

1. Li-ion Batteries' Trend in 2014

Commercial Li-ion batteries (LIB) is currently operated at 3.6~3.7V, which are comprised of cathode, which is generally designed with transition metal oxides, and anode such as graphite and hard/soft carbon.¹⁻² The performance of LIB is dependent on the type of cathode materials, and lithium cobalt oxides (LiCoO₂, LCO) is usually used in mobile application,³ while lithium manganese oxides (LiMn₂O₄, LMO) or lithium iron phosphate (LiFePO₄, LFP) has been applied to electric vehicle (EV) due to fluent resource, and low manufacture cost.⁴⁻⁵ For a cell configuration, the laminate type of cell has been developed to use in practical application due to high thermal stability and capacity with low internal resistance.⁶ The electromotive force of LIB is ~3 times higher than that of Ni-based rechargeable batteries such as nickel metal hydride (NiMH) system (**Table 1**).⁷ At present, the cost of cathode material accounts for 30~40% in LIB production, as shown in **Figure 1a**,⁸ and their specific capacity is around 150 mAh/g in the present system. However, the development of cathode materials with > 250 mAh/g is still needed to be developed for smaller LIB system with high capacity. Also, in anode part, graphite has been mainly used due to superior stability and reversibility in various applications, but the development of alternative anode with 500~800 mAh/g is needed to balance the cell when increasing the capacity of cathode materials is considered.

LIB can be categorized depending on the cell type: 1) prismatic, 2) cylindrical, 3) polymer cell. (**Table 2**),⁹ and their application fields are described in **Figure 2**. In case of Li-ion polymer cell, it is expected that considering its growth rate with 34.6% per year, the value is superior to cylindrical (-2.6%) and prismatic (-2.4%) value, expecting 51.4% in 2016 (**Figure 3**).¹⁰

1.1. Electric vehicles

In world battery market, mobile applications exhibit the market formation with \$645 billion in 2012, and secondary batteries account for 24.3% of the market share.¹¹ Also, energy storage system (ESS) and EV market enable an market expansion of the secondary batteries to approach \$1,046 billion in 2017, and the portion of LIB is expected to rapidly increase with 39.5% (**Table 3**).¹¹ Elon Musk (CEO in Tesla) has suggested 35,000 units of sales target for electric vehicles (EVs), but the supply of secondary batteries is difficult to meet the highly growing demand of Tesla EVs at present.¹² Accordingly, to solve this problem, Tesla has a plan to establish Giga-factory for secondary batteries production via \$2 billion investment, and Panasonic company will invest 50% of total fund.¹³ Also,

because of a strategic corporation between Tesla and Panasonic, various kinds of global EV companies may have a strategic alliance with secondary batteries suppliers to expand their investment toward EV market.

Among main problems – cost, mileage, charge – that obstructs the market expansion of EV, the solutions of cost and mileage have been expected to gradually increase in 2014, and the EV sales is expected to increase from 1.62 million units in 2012 to 10.25 million units in 2018 with 36% of average annual increase.¹¹ Also, because of the release of Tesla model S and BMW i3, the global sales of EV will be continuously grown. Recently, with an additional plant establishment for plug-in hybrid electric vehicle (PHEV) in General Motors,¹⁴ the activation of LIB market is positively expected because PHEV have started to adapt LIB as a main source of power supply. In addition, the enhanced environmental regulation in USA and Europe will be a positive factor for the expansion of EV market from 2015. In other words, the supply of environmental vehicles such as EV can be an urgent task due to limitation of mileage increase in gasoline system. Global automobile supplier has drawn attention to secondary batteries suppliers because the improvement of battery performance becomes an important factor to dominate EV market in advance and helps to increase a mileage of electric vehicles.

In hybrid electric vehicle (HEV) market, NiMH has been verified as a reliable power resource, but LIB has been taken into account as more suitable alternative due to long cycle-life, high energy density, little self-discharge, and negligible memory effect. Also, LIB has 60% of lighter than that of NiMH. Despite of these advantages, a main reason for slow progress in commercialization is short mileage. In case of vehicles with internal combustion engine (ICE), they can travel more than 500 km, while EV, for example, Leaf in Nissan and Model S in Tesla, is possible to drive up to 120 km and 426 km after full charge, respectively.¹⁵⁻¹⁶ In other words, the short-mileage in EV means that a regular charge is highly required, giving problems such as a shortage of EV charge infrastructure and fast charging within a few minutes. If there exists constraints of time and space for charging a battery, the estimates of EV can be devaluated for customers. Accordingly, EV companies should devise various solutions such as a fast battery replacement and battery charge-only system with a standardization of high voltage and current supply. Also, in a view of production cost, the value of EV is about 2.5 times higher than that of ICE vehicle.¹⁷ In turn, it is difficult to satisfy the growing demand from customers for a short period. In order to solve this problem, it is basically required that a cost for manufacture system and charging a battery should be reduced.

With a rapid increase of EV market, a battery price is expected to gradually decline, according to the report that 11.1% of annual decline rate is achieved for LIB cost from 2003 to 2011.¹⁷ In 2011, Department of Energy (DOE) in U.S.A. has suggested that a cost of EV/PHEV is needed to reduce from \$700~950/kWh to \$300/kWh for 1 million sales until 2015.¹⁸ For the reduction of battery cost, it is necessary to deal with an efficient battery pack design, the use of high energy materials as well as low

manufacturing cost. Also, according to DOE report of battery manufacture, the manufacturing cost can be efficiently reduced up to 30~40% when annual battery production is increased from 10,000 to 100,000 units.¹⁹ In real, because a proportion of battery cost have occupied with 30~40% of total price in EV, battery suppliers should have a certain level of economic of scale to reduce a total battery cost, which includes a fluent resource of electrode materials as well as good economic feasibility. Currently, NiMH battery has still influenced on EV system, but LIB influence will be greater due to its good performances if a release of PHEV is gradually increased (**Figure 4**).

Nowadays, automotive OEM suppliers continues forming various value chains for materials and parts through a diversity of secondary batteries suppliers (**Figure 5**).²⁰ The global companies producing a mid-to large sized battery will continue to expand their occupancy until 2015 to follow a growing EV market. General focus of mid-to large sized battery market is still demand rather than supply at present, which is also induced by a fast development of ESS.

According to a guideline in battery manufacturers, they recommend that the working condition of EV batteries (LMO/graphite) should be controlled in the range of -20~55 °C for discharge and 0~45 °C for charge, respectively. Especially, LIB containing $\text{Li}_4\text{Ti}_5\text{O}_{12}$ (LTO) as anode can be discharged even at -30 °C condition. The driving voltage windows of LIB is generally operated within a range of 1.5~4.2V (LCO/graphite, $\text{Li}(\text{Ni}_x\text{Co}_y\text{Al}_z)\text{O}_2$ (NCA)/graphite, $\text{Li}(\text{Ni}_x\text{Co}_y\text{Mn}_z)\text{O}_2$ (NCM)/graphite, LMO/graphite: 2.5~4.5V, LMO/LTO: 1.5~2.7V, LFP/graphite: 2.0~3.7V).²¹ **Table 4** describes the cell materials depending on EV type and battery companies. At present, a blend strategy such as LMO/NCM has been currently applied to meet EV's requirements in cathode system, and anode is also same tendency as cathode. Also, the specification of battery pack, which is currently adapted in PHEV companies, is demonstrated in **Table 5**.¹¹

1.2. Energy storage system

The trend transition in LIB market from IT application to medium/large size application will be accelerated with the growing ESS market which will be grown from 23 GWh in 2013 to 90.9 GWh in 2020 with 21.7% of annual growth rate.²² In turn, a demand of ESS is expected to surge under the increased demand for energy efficiency and expansion of renewable energy. Also, the subsidy policy in U.S.A, Germany, and Japan will drive the growth of an initial ESS market. Accordingly, based on these tendency, ESS market utilizing LIB is expected to record the highest growth with 2,020 GWh from 1.4 GWh in 2013 (46.8% of annual growth rate).²³

In detail, ESS system is strongly required to meet the following reasons; 1) an efficient load management at power peak, 2) a stable power supply in electrical grid, 3) a management of black-out,

4) an efficient electricity supply for customers' requirement, and 5) a good power quality from renewable energy. The representative field of ESS adapting LIB will be an uninterruptible power supply (UPS) which has formed \$ 10 billion market,²⁴ because of LIB's cost-competitiveness. Existing UPS has utilized a lead-acid battery, but the market situation starts to change. This is induced by an establishment of LIB production line for EV because LIB design applied to EV can have a possibility to cover the required specifications in UPS system. The price of lead-acid battery is \$300/kWh which is 40% higher than \$500/kWh of LIB.¹¹ However, when considering the price per 1kW, which assumes that its value corresponds to maintain UPS system for 30 min, lead-acid battery requires \$360/kW, but LIB does \$263/kW.²⁴ In turn, LIB can be sufficiently considered in existing UPS market due to 27 % of cost reduction. Also, LIB weight per capacity is 1/3 of lead-acid battery, and LIB can be 1/5 lighter than that of lead-acid batteries with 1/3 of space reduction.²⁴ Finally, because of long life-cycle of LIB (10 years) compared to lead acid battery (5 years), lead-acid batteries in UPS can be replaced by LIB, which the exchange speed will be faster than expected.

ESS can be classified in terms of time, output and techniques. A product having a response within 1h is named as short period ESS, and long period ESS is referred for a product with > 2h response (**Table 6.1 and 2**).²⁴ LIB, a lead-acid battery, supercapacitor and flywheel are used in short period ESS, while LIB, flow battery, sodium-sulphur battery, compressed-air, and pump-hydro energy storage are applied to long period ESS. Currently, only LIB can be applicable to both conditions, and the market perspectives of ESS equipped with LIB can be positively expected to increase due to little limitation of capacity design and installation. Also, the effect of cost saving can be expected because LIB can be efficiently adapted in ESS through the technologies that has been currently utilized in IT and EV applications. Moreover, an electricity project will be accelerated in smart grid via an increase of electric charge. Therefore, the demand of LIB will increase exponentially because it is recognized as an essential energy storage in ESS.

2. Materials in Li-ion Batteries

The market of LIB materials in ESS and small IT application is expected to grow faster from \$83 billion in 2013 to \$205 billion in 2020. The proportion of LIB components is 36% of cathode, 13% of anode, 14% of separator, 9% of electrolyte, 12% of copper foil, 4% of aluminum foil, 12% of others.⁸ For LIB cost, materials account for 50~60%, and the capacity, cycle-life, and stability can be determined depending on how materials are combined.¹⁷ **Table 7** describes the main companies producing each materials, LIB parts, and cell makers with their market share (**Figure 6**).²⁵

2.1. Cathodes

Cathode materials has the highest proportion in the LIB material cost, as shown in **Figure 1b**, and they are classified into layered, spinel, and olivine depending on a structure (**Table 8**). The representative material in layered structure is LiCoO_2 , $\text{Li}(\text{Ni}_x\text{Co}_y\text{Mn}_z)\text{O}_2$ (NCM), and $\text{Li}(\text{Ni}_x\text{Co}_y\text{Al}_z)\text{O}_2$ (NCA),²⁶ which metal oxide slabs and lithium ion are alternatively stacked. Cobalt, nickel, and manganese element in this structure are generally regarded as a characteristic of high energy density, capacity, and structure stability for material design, respectively. For example, NCA and NCM are well-constructed through each element combination. The NCM price is cheaper than that of NCA, and its side reactions do not occur even at high-voltage charge ($> 4.3\text{V}$), showing an excellent life characteristics. However, the electronic conductivity of NCM is lower than that of LCO, resulting in poor rate capability.²⁷ Cathode materials with layered structure have different characteristics depending on the type of metal and ratio in crystal structure. For spinel structure, LMO, which has been proposed by Thackeray et al. in 1983,²⁸ is a representative, and its oxygen framework is the same as that of layered structure. Unlike layered structure, the collapse of crystal structure is not shown when Li ion is extracted during cycling. Also, not only it can be operated at $\sim 4\text{V}$ with high power density induced by 3-dimensional pathway of Li-ion, but also LMO has a cost competitiveness due to low Mn price. Despite of these advantages, it has a shortcoming of the capacity reduction at high temperatures.^{26, 29} In olivine structure, LFP is a representative, and has been attractive due to its low cost, high thermal stability and environment friendliness.³⁰ LFP describes excellent electrochemical properties due to a unique structure stability. However, its discharge voltage exhibits 3.45 V whose value is lower than that of spinel and layered based cathode material,⁵ giving a decrease of electric power and restriction on the use in practical application. Recently, carbon coating and the addition of Mn in LFP structure have been tried to increase an electrical conductivity and discharge voltage, respectively.³¹⁻³² Depending on the characteristic of cathode materials, LCO and NCA is mainly applicable to small IT devices and electrically-drive tools, respectively, while NCM and LMO has been used in ESS or EV applications.

2.2. Anodes

Like cathode, anode is also an important part to determine a capacity, power, and safety in battery. Especially, the energy density of LIB is mainly determined by the degree of irreversible capacity of anode. Natural and artificial graphite, which are largely used in a practical use, have been mainly applied to general-purpose product and high-end products such as smart phone. Generally, artificial graphite describes higher capacity than that of natural one (**Table 9**).⁸ Also, artificial graphite has cost-profitability because its manufacturing process is relatively difficult. Anode materials account for 18% in LIB material cost, which has \$0.68 billion of scale in 2012. Graphite occupies 96% of possession in

anode materials, and 62% of total use is natural graphite.¹⁷ The price of artificial graphite, natural graphite, soft carbon, silicon is \$25, \$12, \$15, \$30 per kg, respectively, and natural graphite is most competitive in terms of a price.³³ For a trend of LIB cost reduction, natural graphite has continuously occupied anode market due to its low cost, but artificial graphite has been slightly expanded to EV market due to its stability and longevity. HEV has utilized a mixture consisting of 80% of an amorphous carbon (hard carbon or soft carbon) and 20% of graphite for high power, while a mixture with 80% of graphite and 20% of an amorphous carbon is applied to high energy requirement.¹⁷ Accordingly, the demand of graphite market is judged to lead to the increase.

However, because a practical capacity of graphite is not high value, new electrode material should be studied to solve low capacity of graphite. As a result, alloy materials such as silicon, germanium, and tin have been suggested, but it is difficult to drive a cycle due to a desorption phenomenon caused by volume expansion/contraction during cycling. Nowadays, with various strategies of volume exchange, silicon/carbon composite has been considered as a commercially available solution to increase battery capacity, but the amount of silicon contained is extremely limited in practical approach.

In addition to the mentioned anode materials, $\text{Li}_4\text{Ti}_5\text{O}_{12}$ (LTO) with 1.5V operating voltage has been currently studied, showing little decomposition of the electrolyte. With the combination with 5V cathode electrode, the 3V-cell based studies have been conducted for the realization of high power and energy density.³⁴ In case of metal oxide, it has high cycle stability and power density, but is difficult to commercialize due to low electric conductivity and large initial irreversible capacity. To address these problems, carbon coating and morphology control have made attempts to improve a battery performance.³⁵

2.3. Separator

Separator has a function to separate cathode and anode electrode for a prevention of electrical contact between the electrodes. Also, it enables lithium ion to penetrate through the pores during electrochemical reaction, and accounts for 15% in LIB material cost. Depending on how separator is produced, it can be classified into dry- and wet-based process.¹⁷ IT devices adapt a separator from a mixed process, while EV system utilizes one from dry-process due to an excellent high-temperature stability. Generally, separator has a thickness of $\sim 20 \mu\text{m}$, which is porosity film based on polyolefin.⁸ Also, the very small pores are produced to pass through lithium ions only, and the separator porosity has greatly influenced on the output characteristics of the battery.³⁶ For existing small applications, separator is mainly comprised of polyethylene or polypropylene, and the research of increasing porosity has been studied to enhance a cycle-life and high power characteristics in automobiles' LIB. Importantly, separator is critical component to influence on stability in battery, i.e., induces rapid thermal shrinkage

when batteries are exposed to heat above 150 °C, finally, resulting in an internal short-circuit. Therefore, in order to prevent explosion of the battery, the thermal contraction is also required for cell stability, and the surface coating with inorganic materials has been applied to realize the required thermal property.³⁷ Recently, because smart device such as tablet PC have required thinner characteristic, a level of 16 μm is needed to follow the growing demand.

2.4. Electrolyte

Electrolyte can be considered as an intermediate allowing a transport of lithium ion during charge/discharge. It consists of co-solvent, which is mixed with a low viscosity solvent and a high permittivity solvent, and a lithium salt prepared by dissolving a predetermined concentration.³⁸ Lithium hexafluorophosphate (LiPF₆) is generally used as lithium salt due to high ionic conductivity and good stability. To stabilize an interface between electrode and electrolyte, the additives is added, and a fluorine-based electrolytes is currently being used to improve an electrolyte stability with poor flame retardancy.³⁹ For the development of advanced electrolyte, it is strongly considered that electrolyte should be designed with i) non-fluorine-based flame retardant property, ii) electrochemical stability within operating voltage, iii) thermal stability at high operating temperature, and iv) securing the ion conductivity at low temperature. Additionally, a polymer electrolyte is considered due to little leakage and high stability, but its ion conductivity is low. Therefore, to address this problem, a plasticizer is added to make gel condition which can improve a rate of ionic conductivity in polymer electrolyte.⁴⁰

2.5. Current collector

Current collector is thin metal foil which receives electrons from or to external circuit, and is a substrate for electrode slurry coating. An aluminum and copper are generally used in cathode and anode, respectively. The main characteristics of the current collector are surface roughness and thickness. In case of thickness, its value is normally in the range of 8~10 μm, but the thickness under 6 μm is gradually required to meet the growing demand of thinner characteristic in various applications.

3. The properties changes at high temperature and voltage in LIB

When the operating temperature approach the range of 90~120 °C in LIB, SEI film starts to exothermically decompose.⁴¹ If the temperature approach 120 °C, the combustion gas begins to occur by the additional reaction between carbon electrode and organic electrolyte. Finally, at above 200 °C, electrolyte starts to decompose with large amount of combustion gas, resulting in a flame reaction

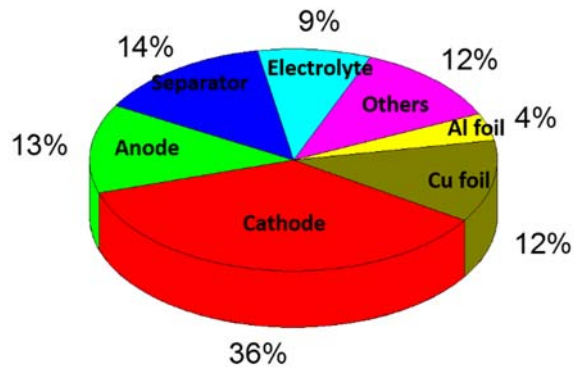
produced by disturbance reaction with oxygen produced by cathode decomposition. If LIB is charged at less than 0 °C, lithium metal is accumulated on the surface of carbon electrode. As the temperature is further lowered, the battery is on short-circuit state.²¹

In a view of cathode, if the operating voltage is too low or batteries are over-discharged, the battery performance is negatively influenced by structure collapse of cathode material. In addition, if extremely low-voltage or over-discharge state is reached, the combustion gas is generated in the electrolyte reduction, posing a potential safety risk in battery system. When batteries are operated at high voltage or extremely overcharged condition, a significant amount of heat is generated by cathode decomposition. In addition, battery capacity is gradually reduced by the accumulation of lithium metal on anode, finally safety problems are caused by internal short circuit and electrolyte decomposition, which occurs at > 4.5 V charge.²¹

Table 1. The characteristics comparison between NiMH and LIB.

	NiMH	LIB
Operating voltage (V)	1.2	3.6
Power density (kW/kg)	1.0~1.5	3.0~4.0
Energy density (Wh/kg)	40~50	60~100
Life (years)	5	10
Self-discharge/memory effect	O / O	Little / X
Stability	Normal	Need a protection circuit
Relative cost	1	3

(a) The proportion of material cost in LIB parts



(b) The scale of LIB material market

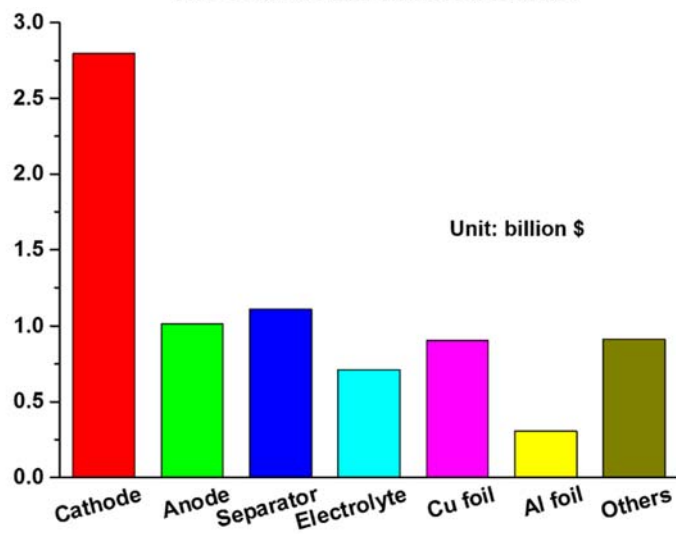


Figure 1. (a) The proportion of material cost in Lithium-ion batteries and (b) the scale of LIB material market.⁸

Table 2. Li-ion batteries configuration and characteristics

	Prismatic cell	Cylindrical cell	Li-ion polymer cell
Main purpose	Mobile phone, PDA, Digital camera	Laptop PC, Camcorder, Electric-drive tool, Electric bicycles	Mobile phone, PDA, Audio, Bluetooth, Tablet PC
Capacity	91~107 mAh/cm ²	27~143 mAh/cm ²	94~117 mAh/cm ²
Characteristics	<ul style="list-style-type: none"> - Variety type - Easy compatibility with communication devices 	<ul style="list-style-type: none"> - Stable discharge - Long cycle-life 	<ul style="list-style-type: none"> - Shape flexibility - High energy density with light weight
Main manufacturer	Sanyo, Sony, BYD, Samsung SDI, LG Chem.	Sanyo, Sony, Panasonic, Samsung SDI, LG Chem.	Sanyo, Sony, Panasonic, Samsung SDI, LG Chem.

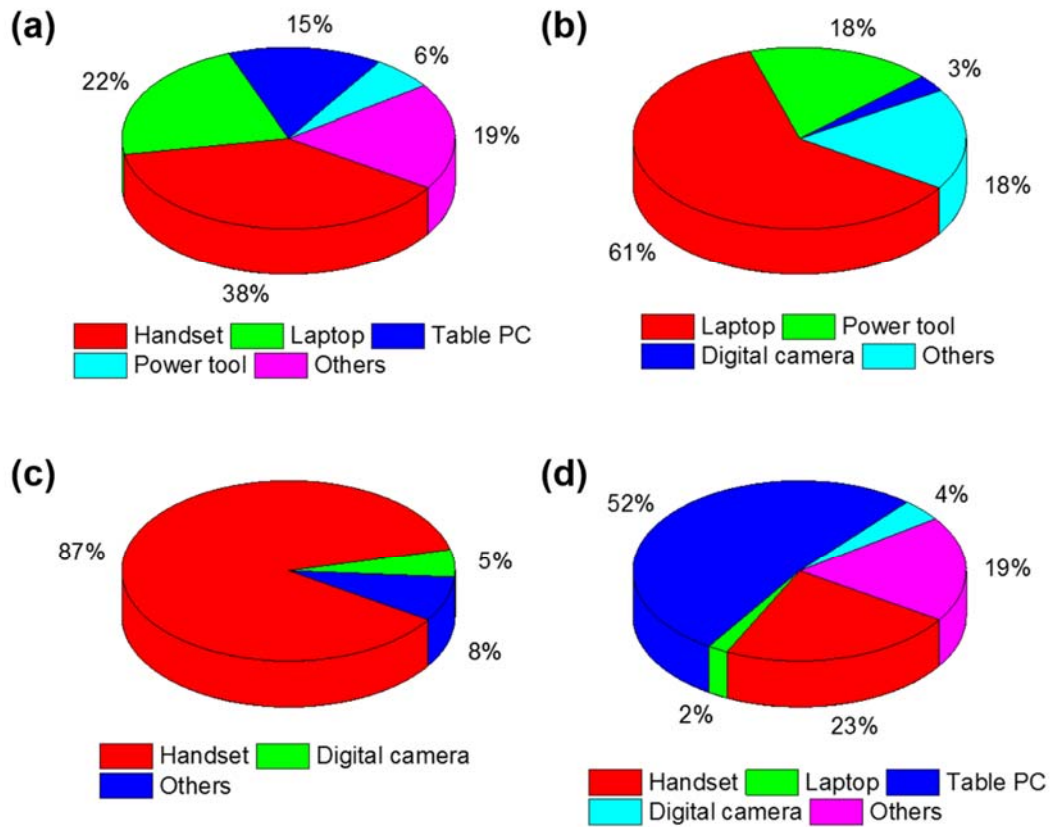


Figure 2. (a) The proportion of secondary batteries depending on applications, (b, c, and d) the application proportion of cylindrical, prismatic, and pouch type, respectively.

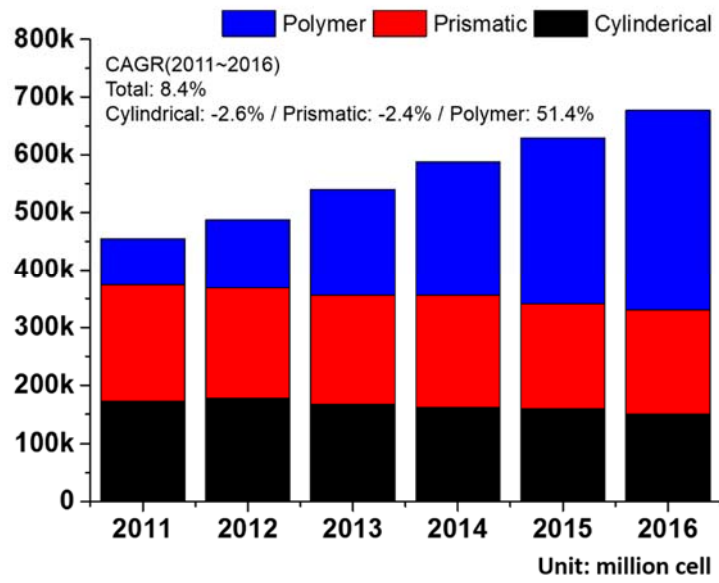


Figure 3. The market trend of global lithium-ion batteries: shipments depending on a cell type.²²

Table 3. The market share and expectation of secondary batteries.¹¹

		2012	2013	2014	2015	2016	2017	'07~'12 CAGR
World total		645	698	765	832	928	1,046	10.2%
LIB		157	202	251	301	359	414	21.4%
LIB Applications	Mobile IT	128	136	139	145	150	148	2.9%
	Electric vehicles	12	17	25	37	54	80	46.1%
	Energy storage	17	49	87	119	155	186	61.4%
Lead-acid		444	450	455	461	467	472	1.2%
Capacitor		4	5	13	28	61	121	97.8%
Ni based system		34	33	37	32	31	28	-3.8%
Others		6	8	9	10	10	11	12.9%

(Unit. $\times 10^2$ million dollars)

Table 4. The cell materials in electric vehicles depending on the battery companies.²²

EV type	Film pouch					Can prismatic								
	HEV		PHEV	BEV		HEV				PHEV		BEV		xEV
Company	LG Chem	AESC	LG Chem	AESC	LG Chem	Panasonic	BEC	HVE	Toshiba	PEVE	Panasonic	LEJ	BYD	Samsung SDI
Cathode	LMO NCM	LMO LNO	LMO NCM	LMO LNO	LMO NCM	NCM	NCM	NCM KMO	LNMO	LNO	NCM	LMO NCM	LFP	NCM LMO
Anode	GP HC	SC	GP HC	GP	GP HC	GP	HC	HC SC	LTO	GP	GP SC	GP Mix	GP	GP
Separator	PP dry	3Layer	PP dry	PP dry	PP dry	3Layer	PE wet	3Layer	Celrose	3Layer	3Layer	PE wet	PP dry	PE wet 3Layer
OEM	Hyundai Kia	Nissan	GM	Nissan	Renault Ford	Toyota	Hoda	Nissan	Toyota	Toyota	Toyota	Mitsubishi	BYD	BMW

Table 5. The specifications of PHEV depending on automobile manufacturers.¹¹

Manufacturer	Model	Cell			Pack	Energy kWh	Capacity Ah	Voltage V
		Supplier	Cathode	Capacity	Supplier			
			Chemistry	Ah				
Fisker	Karma	A123	LFP	20	A123	20	60	333
GM	Volt	LG	LMO/NCM	15	GM	16	45	356
Mitsubishi	Outlander	LEJ	LFP	21	LEJ	12	42	286
Volvo	V60	LG	LMO/NCM	15	LG	11	30	367
Porsche	Panamera	Samsung	NCM/LMO	26	Bosch	9.4	26	362
BMW	i8	Samsung	NCM/LMO	26	BMW	8.5	26	327
Ford	C-Max	Sanyo	NCM	24	Ford	7.6	24	317
Ford	Fusion	Sanyo	NCM	24	Ford	7.6	24	317
Audi	A3	Sanyo	NCM	24	Sanyo	7.5	24	313
Honda	Accord	Blue Energy	NCM	21	Honda	6.6	21	314
Daimler	S class	LEJ	LFP	21	Magna	6.5	21	310
Toyota	Prius	Sanyo	NCM	22	Toyota	4.5	21.5	209

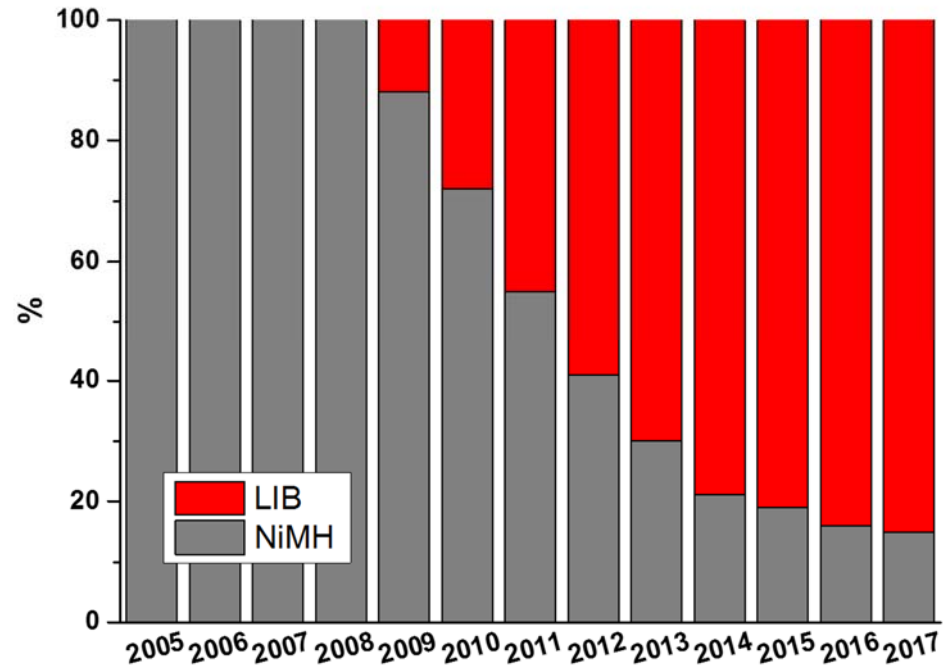


Figure 4. The perspective of NiMH and LIB market for HEV.

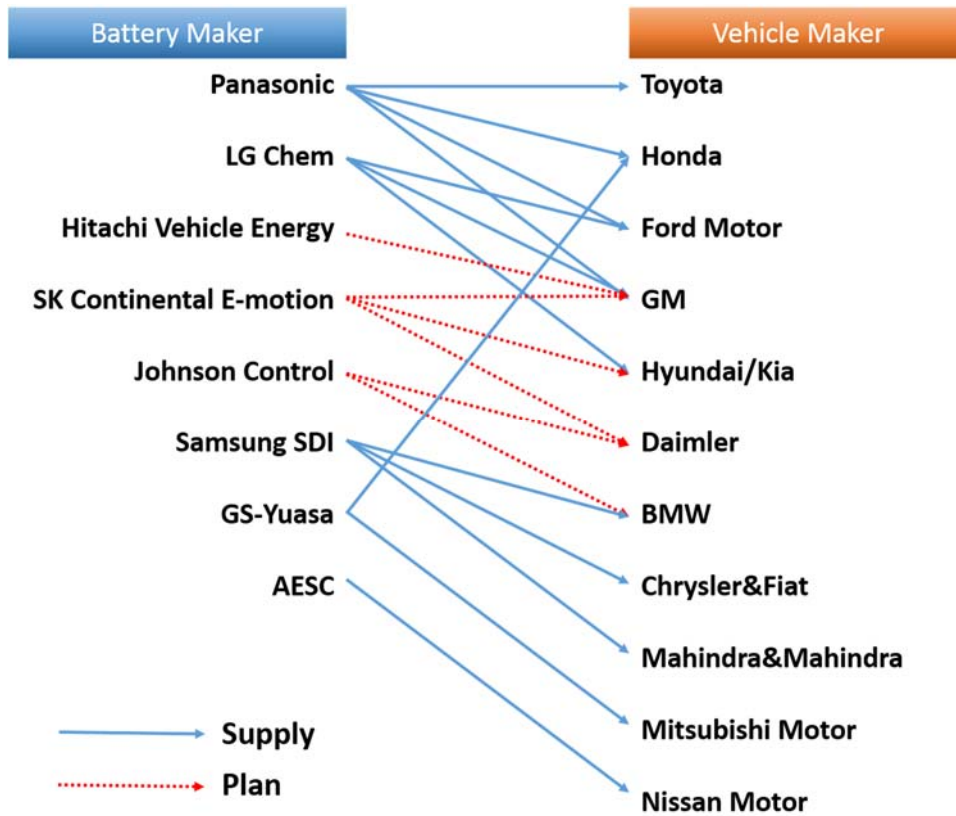


Figure 5. The value-chain configuration between battery and vehicle makers.²⁰

Table 6.1. The classification of ESS

	Less than 10 kW	10~100 kW	100 kW ~ 1 MW	1~10 MW	10 ~ 100 MW
30 min	UPS (lead-acid battery, LIB, supercapacitor, flywheel)		UPS for industry (lead-acid battery, LIB)	Utility frequency control (LIB)	
1 ~ 2h	The quality improvement of renewable energy and ESS for back-up (lead-acid battery, LIB)				
More than 5h	Smart grid for home use (LIB)	Smart grid for industry (LIB)	Correspondence of industrial electricity peak (LIB)	Utility load-leveling [pump-hydro (> 100MW), compressed-air (>20 MW), sodium-sulphur battery, flow battery]	
			Off-grid renewable energy supply (LIB)		

Table 6.2. The classification and properties of ESS

	Type	Principle	Advantages	Disadvantages	Efficiency (%)
Short period ESS	LIB	Redox reaction	High energy density and efficiency	High cost	95
	Lead-acid		Low cost	Toxicity	70
	Supercapacitor	Adsorption of ions	High power density, stability, long cycle-life	Low energy density and high cost	95
	Flywheel	Rotation	High power density, large capacity, long cycle-life	Low energy density, high cost, sensitive to vibration	90
Long period ESS	Flow battery	Redox reaction	Low cost, large capacity, long cycle-life	Low energy density, low efficiency	60~80
	Sodium-sulphur		High power density, low cost	High operating temperature, low efficiency	75~85
	Compressed-air	Pressure	Large capacity	High cost, limited location	60

Table 7. The main companies of LIB materials, parts, and cell makers.¹⁷

	South Korea	International
Cathode	L&F / Ecopro / Hanwha Chemical Daejung Chemicals & Metals / Phoenix Materials Wooree ETI / Elbatek / Samsung Fine Chemicals	Umicore / Nichia / Toda Kogyo
Anode	Poscochemtech / GS Caltex / Aekyung Petrochemical Co.	Hitachi Chemical / BTR Energy / Mitsubishi Chemical Total Carbon / Nippon Carbon / SEC Carbon
Electrolyte	Panaxetec / Soulbrain / Foosung / Leechem	Mitsubishi Chemical / Ube Industries / Stella Chemifa Kanto Denka
Separator	SK Innovation / CS Tech Co. / TopTech	Asahi Kasei / Celgard / Toray Tonen
Cell makers	Samsung SDI / LG Chem / SK Innovation	Panasonic / AESC / Hitachi Vehicle Energy / B456 BYD / GS Yuasa / PEVE / Lithium Energy Japan JCS
Instrument	PNE Solution / CIS / KapJin / ETH / PNT	-
Parts	Protection circuit: Powerlogics / Nexcontech / Seowon Intech Copper foil: Iljin Materials / Furukawa Electric / Nippon Foil Mfg / Nippon Denkai Others: Elentec / Wisepower / Snag-A Frontec / Sangsin EDP	

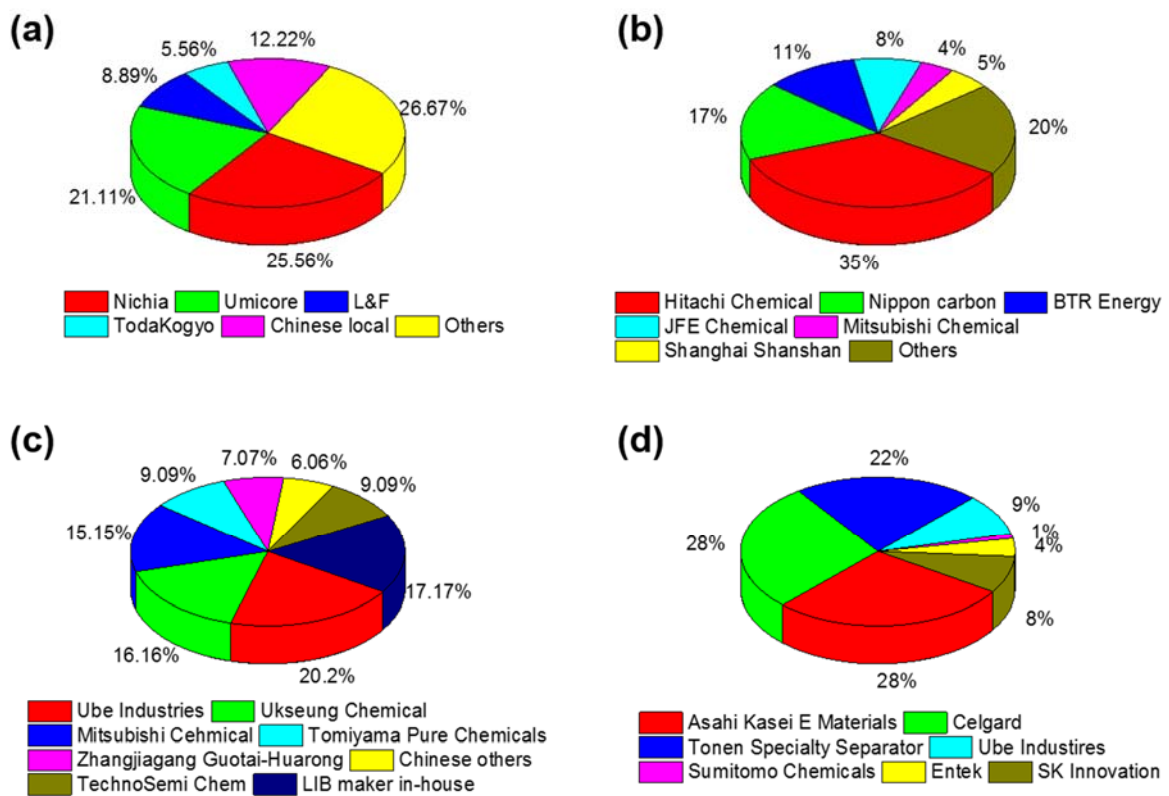


Figure 6. The market share of main companies producing (a) cathode, (b) anode, (c) electrolyte, and (d) separator in 2009.

Table 8. The classification of cathode materials

	Layered	Spinel	Olivine
Chemical composition	LiMO_2 (M = Co, Ni, Mn)	LiM_2O_4 (M = Mn, Ni)	LiMPO_4 (M = Fe, Mn, Co)
Representative	LiCoO_2 , $\text{LiNi}_x\text{Co}_y\text{Mn}_z\text{O}_2$, $\text{LiNi}_x\text{Co}_y\text{Al}_z\text{O}_2$	LiMn_2O_4	LiFePO_4
Advantages	High energy density	High power density	Low cost (Fe), high stability
Disadvantages	High cost	Short cycle-life (Mn dissolution)	Low power (low operating voltage)
Energy density	High	Medium	Low
Power	Medium	High	Low
Cycle-life	High	Low	Low
Price	High	Medium	Low
Stability	Low	Medium	High
R&D direction	Ternary (Ni, Mn, Co) composition development Co replacement for cost The content increase of Ni for capacity The content increase of Mn for stability	The Mn substitution to other transition metal	Fe substitution with Mn

Table 9. The comparison of various graphite.

	Artificial graphite	Natural graphite	Amorphous carbon
Specific capacity (mAh/g)	280~360	360~370	235~315
Surface area (m ² /g)	<1	3~8	2~5
Cycle-life	High	Low	Medium
Price (\$/kg)	25	12	15
Manufacturer	POSCO CHEMTECH Hitachi Chemical JFE Chemical	AEKYUNG PETROCHEMICAL Shanghai Shanshan BTR Energy	GS Caltex Nippon Carbon JFE Chemical

References

1. Xu, X.; Lee, S.; Jeong, S.; Kim, Y.; Cho, J., Recent progress on nanostructured 4V cathode materials for Li-ion batteries for mobile electronics. *Mater. Today* **2013**, *16* (12), 487-495.
2. Moshtev, R.; Johnson, B., State of the art of commercial Li ion batteries. *J. Power Sources* **2000**, *91* (2), 86-91.
3. Jeong, S.; Park, S.; Cho, J., High-Performance, Layered, 3D-LiCoO₂ Cathodes with a Nanoscale Co₃O₄ Coating via Chemical Etching. *Adv. Energy Mater.* **2011**, *1* (3), 368-372.
4. Tran, H. Y.; Täubert, C.; Fleischhammer, M.; Axmann, P.; Küppers, L.; Wohlfahrt-Mehrens, M., LiMn₂O₄ Spinel/LiNi_{0.8}Co_{0.15}Al_{0.05}O₂ Blends as Cathode Materials for Lithium-Ion Batteries. *J. Electrochem. Soc.* **2011**, *158* (5), A556-A561.
5. Yuan, L.-X.; Wang, Z.-H.; Zhang, W.-X.; Hu, X.-L.; Chen, J.-T.; Huang, Y.-H.; Goodenough, J. B., Development and challenges of LiFePO₄ cathode material for lithium-ion batteries. *Energ. Environ. Sci.* **2011**, *4* (2), 269-284.
6. Gozdz, A. S.; Warren, P. C., Material and method for low internal resistance LI-ion battery. Google Patents: 1996.
7. Yang, Z.; Zhang, J.; Kintner-Meyer, M. C. W.; Lu, X.; Choi, D.; Lemmon, J. P.; Liu, J., Electrochemical Energy Storage for Green Grid. *Chem. Rev.* 2011/05/11, 2011, pp 3577-3613.
8. Meritz Securities report in 2013.
9. Winter, M.; Brodd, R. J., What Are Batteries, Fuel Cells, and Supercapacitors? *Chem. Rev.* **2004**, *104* (10), 4245-4270.
10. Hwnwha Investment & Securities report in 2013.
11. Industry & Economic research in 2014.
12. http://www.newfuelist.com/link/~58rm#.U3sLhfl_suw.
13. Tesla CEO: Panasonic Likely Partner in Battery Plant. <http://online.wsj.com/article/BT-CO-20140422-702443.html>.
14. <http://www.detroitnews.com/article/20140405/AUTO0103/304050025#ixzz2y7PNIFq2>.
15. http://www.greencarreports.com/news/1089545_2014-nissan-leaf-electric-car-84-mile-range-aroundview-standard.
16. <http://www.greencarcongress.com/2012/06/models-20120621.html>.
17. Samsung Securities report in 2013.
18. Davis, P. B. *Vehicle Efficiency and Electrification*; 2011.
19. Howell, D. *Battery Status and Cost Reduction Prospects*; 2012.
20. SK Securitates report in 2013.

21. Lu, L.; Han, X.; Li, J.; Hua, J.; Ouyang, M., A review on the key issues for lithium-ion battery management in electric vehicles. *J. Power Sources* **2013**, *226* (0), 272-288.
22. Hwnwha Investment & Securities report in 2013.
23. <http://www.econovill.com/wp-print.php?id=113082>.
24. *Energy Storage System*, Mirae Asset Securities in 2013.
25. Electronic Telecommunications Research Institute report in 2013.
26. Xu, B.; Qian, D.; Wang, Z.; Meng, Y. S., Recent progress in cathode materials research for advanced lithium ion batteries. *Mat. Sci. Eng. R: Reports* **2012**, *73* (5-6), 51-65.
27. He, J.-r.; Chen, Y.-f.; Li, P.-j.; Wang, Z.-g.; Qi, F.; Liu, J.-b., Synthesis and electrochemical properties of graphene-modified $\text{LiCo}_{1/3}\text{Ni}_{1/3}\text{Mn}_{1/3}\text{O}_2$ cathodes for lithium ion batteries. *RSC Adv.* **2014**, *4* (5), 2568-2572.
28. Thackeray, M. M.; David, W. I. F.; Bruce, P. G.; Goodenough, J. B., Lithium insertion into manganese spinels. *Mater. Res. Bull.* **1983**, *18* (4), 461-472.
29. Aoshima, T.; Okahara, K.; Kiyohara, C.; Shizuka, K., Mechanisms of manganese spinels dissolution and capacity fade at high temperature. *J. Power Sources* **2001**, *97-98* (0), 377-380.
30. Wu, X.-L.; Jiang, L.-Y.; Cao, F.-F.; Guo, Y.-G.; Wan, L.-J., LiFePO_4 Nanoparticles Embedded in a Nanoporous Carbon Matrix: Superior Cathode Material for Electrochemical Energy-Storage Devices. *Adv. Mater.* **2009**, *21* (25-26), 2710-2714.
31. Wang, J.; Sun, X., Understanding and recent development of carbon coating on LiFePO_4 cathode materials for lithium-ion batteries. *Energ. Environ. Sci.* **2012**, *5* (1), 5163-5185.
32. Yang, M.-R.; Ke, W.-H., The Doping Effect on the Electrochemical Properties of $\text{LiFe}_{0.95}\text{M}_{0.05}\text{PO}_4$ ($\text{M} = \text{Mg}^{2+}$, Ni^{2+} , Al^{3+} , or V^{3+}) as Cathode Materials for Lithium-Ion Cells. *J. Electrochem. Soc.* **2008**, *155* (10), A729-A732.
33. http://magazine.hankyung.com/money/apps/news?popup=0&nid=02&nkey=2013111800102073442&mode=sub_view
34. Dedryvère, R.; Foix, D.; Franger, S.; Patoux, S.; Daniel, L.; Gonbeau, D., Electrode/Electrolyte Interface Reactivity in High-Voltage Spinel $\text{LiMn}_{1.6}\text{Ni}_{0.4}\text{O}_4/\text{Li}_4\text{Ti}_5\text{O}_{12}$ Lithium-Ion Battery. *J. Phys. Chem. C* **2010**, *114* (24), 10999-11008.
35. Wu, H. B.; Chen, J. S.; Hng, H. H.; Wen Lou, X., Nanostructured metal oxide-based materials as advanced anodes for lithium-ion batteries. *Nanoscale* **2012**, *4* (8), 2526-2542.
36. Zhang, S. S., A review on the separators of liquid electrolyte Li-ion batteries. *J. Power Sources* **2007**, *164* (1), 351-364.
37. Kang, S. M.; Ryou, M.-H.; Choi, J. W.; Lee, H., Mussel- and Diatom-Inspired Silica Coating on Separators Yields Improved Power and Safety in Li-Ion Batteries. *Chem. Mater.* **2012**, *24* (17), 3481-3485.

38. Xu, K., Nonaqueous Liquid Electrolytes for Lithium-Based Rechargeable Batteries. *Chem. Rev.* **2004**, *104* (10), 4303-4418.
39. Zhang, S. S., A review on electrolyte additives for lithium-ion batteries. *J. Power Sources* **2006**, *162* (2), 1379-1394.
40. Croce, F.; Appetecchi, G. B.; Persi, L.; Scrosati, B., Nanocomposite polymer electrolytes for lithium batteries. *Nature* **1998**, *394* (6692), 456-458.
41. Kim, G.-H.; Pesaran, A.; Spotnitz, R., A three-dimensional thermal abuse model for lithium-ion cells. *J. Power Sources* **2007**, *170* (2), 476-489.

Chapter III

High-Performance, Layered, 3D-LiCoO₂ Cathodes with a Nanoscale Co₃O₄ Coating via Chemical Etching

1. Introduction

Currently, a dominant cathode material of Li-ion battery for 3/4G smart cellular phones is surprisingly LiCoO₂ due to high capacity, low self-discharge, excellent cycle life, and high energy density (3 Wh/cc).¹⁻² LiCoO₂ has the hexagonal α -NaFeO₂ phase consisting of the layered rock-salt structure with the order of Li⁺ and Co³⁺ on alternating (111) plane in cubic structure.³⁻⁵ However, its major drawbacks are fast capacity decaying at higher rates and rapid capacity fade above 4.4V (vs. lithium metal). These problems are based on the anisotropic properties of LiCoO₂ structure showing lattice distortion by the expansion and contraction which results from the large concentration of Co⁴⁺ during cycling.⁶⁻⁷ During de-lithiation of Li_xCoO₂, the *c*-axis expands up to $\sim 2.6\%$ at $x = \sim 0.5$ (~ 4.2 V vs. Li). In addition, the phase changes at ~ 4.5 V with $\sim 3\%$ contraction. It has been suggested that the phase change at ~ 4.5 V is sufficiently large to cause mechanical stresses among the grains. This electrochemical grinding coupled with Co⁴⁺ dissolution and structural degradation by lithiation/de-lithiation results in capacity loss.⁷⁻⁹ In order to minimize Co⁴⁺ dissolution, the metal oxides, such as ZrO₂,¹⁰ TiO₂,¹⁰ B₂O₃,¹⁰ Al₂O₃,^{6, 10-12} MgO,¹¹ SnO₂,¹¹ ZnO,¹³ and AlPO₄¹⁴ have been investigated. These kinds of metal oxides play a key role of protective layer for preventing a direct interaction between the electrolyte solution and LiCoO₂, resulting in decreasing the cobalt dissolution above 4.3 V during cycling.^{7, 15-16}

In this regard, LiCoO₂ with different morphologies such as 1D, 2D, and 3D can also be considered for improving its rate performance, resulting from sufficient contact area between electrolyte and active materials.¹⁷ However, their electrochemical performances were not noticeably improved. Li et al. reported that 1D-LiCoO₂ nanotubes were fabricated by anodic aluminium oxides (AAO) and showed high discharging capacity, 185 mAh/g at 10 mA/g.¹⁸ Jiao et al. reported that 3D-mesoporous LiCoO₂ (LT-LiCoO₂) was synthesized using hard template (KIT-6) at low temperature and the cycle retention was improved, compared to normal LT-LiCoO₂.¹⁹ These nanomaterials may decrease the charging time, but conversely, decrease the electrode density due to the inherent bulky nature.

Here, we report for the first time the concurrent modification of the pristine to the layered 3D-LiCoO₂ with a nanoscale Co₃O₄ coating layer by chemical etching to minimize the capacity loss and to maximize the rate capability of the cathode without the loss of the electrode density. This simple process

is also expected to use to design other materials for improving the performance of active electrode materials in Li-ion batteries.

2. Experimental section

2.1. The layered 3D-LiCoO₂ preparation

The chemical etching process of LiCoO₂ consists of several steps: 10 g of bare LiCoO₂ powder (average particle size was ~10 μm) was added in distilled water at 50 °C, then 1 wt% PVP is mixed for coating on the surface of bare LiCoO₂ for 5 min at 400 rpm. After coating, 1 wt% silver nitrate solution (10 mM AgNO₃ aq.) was added to make a protective layer. Before etching, the resultant was collected by filtration and followed by drying. Subsequently, the powder was etched in 10 wt% HF solution for 60 min at 400 rpm, and followed by washing, with deionized water for several times. The product was completely vacuum-drying at 120 °C for overnight to remove possible water contaminant.

2.2. Analysis instrument

The morphology transformation is characterized by using a scanning electron microscope (SEM, Nanonova 230, FEI), and high resolution transmission electron microscopy (HR-TEM) (JEOL JEM-2100F), operating at 200 kV is used for analyzing the diffraction plane of each sample. Powder analysis is performed on X-ray diffractometer (XRD, D/Max2000, Rigaku). The mole of lithium of Li_xCoO₂ after chemical etching is measured by inductively coupled plasma mass spectrometry (ICP-MS, Varian, USA). X-ray photoelectron spectroscopy (XPS) analysis is performed with a Thermo Scientific Ka spectrometer (monochromatic AlKα, 1486.6 eV). The peak deconvolution of XPS data was done statistically with chi-square value which was ranged between 2 and 3. Therefore, the deconvoluted peak value can be trusted.

2.3. Coin-cell preparation

For characterization of electrochemical properties, the cathodes were made of as-etched powder, carbon black (super P), and poly(vinylidene fluoride) (PVDF) as binder (90:5:5 weight ratio) in N-methyl-2-pyrrolidone (NMP) to make a slurry. The coin-type half cells (2016R-type) consist of lithium metal as the anode, polyethylene separator, and 1.15 M LiPF₆ in ethylene carbonate/dimethyl carbonate/diethylene carbonate (EC/DMC/DEC, 3:4:3 v/v/v) as electrolyte. This process was done according to ref. 1.

3. Results and discussion

We describe a simple route for producing a 3D-LiCoO₂ structure with layered morphology and Co₃O₄ coating layer via chemical etching for improving the electrochemical performance of the pristine LiCoO₂. The process of the layered 3D-LiCoO₂ is as followings (**Figure 1, upper**): 1) In order to generate uniform protecting materials for etching toward LiCoO₂, PVP is used for capping agent to bind with Ag⁺ ions and for reducing them to Ag⁰ particles on the surface of bare LiCoO₂, 2) the obtained sample is immersed to HF-based aqueous etching solution for the optimized time to etch bare LiCoO₂ with Ag particles, 3) the etched sample is dried to remove the residual water at 120 °C for electrochemical test.

SEM images of the as-etched samples confirm the morphology transition from the pristine to the layered 3D-LiCoO₂. **Figure 1a** shows the smooth surface of bare LiCoO₂ apparently changes to layer-by-layer morphology in which each layer thickness is ~ 10 nm after chemical etching. (**Figure 1b**) (also see the low magnification images of bare and the layered 3D-LiCoO₂ in the Supporting Information, **Figure S1**). This morphology transition may be explained as follows: After Ag⁰ particles are formed on the surface of PVP-coated LiCoO₂, they prevent the Ag⁰ loaded LiCoO₂ region from being etched in HF etching solution. Since Ag⁰ nanoparticles deposited on the surface of LiCoO₂ have a strong tendency to form the interconnected alignments by aggregation with neighboring Ag⁰ particles, continuous Ag⁰ layer (**Figure S2**) was made in HF solution, in turn, which act as a protecting layer to make the layered 3D-LiCoO₂ structures.²⁰ If the continuous Ag⁰ alignments are not formed, the morphology is not the layered structure but the randomly etched one (**Figure S2**). **Figure 1c** exhibits the lattice fringe of the (101) plane with d-spacing value of 2.41 Å, corresponding to R3-m phase of LiCoO₂, while as-etched LiCoO₂ has a lattice fringe of (220) plane, corresponding to a d-spacing value of 2.83 Å of spinel Co₃O₄ (**Figure 1d**). Therefore, it is suggested that the Co₃O₄ coating layer with a few nanometer-scale thickness was presented after chemical etching process. Additional evidence for the Co₃O₄ layer formation can be observed in Fast-Fourier Transform (FFT) of the TEM image (at point 3) near the particle surface. The presence of (02-2) and (20-2) planes of the cubic spinel phase that is quite different from the FFT patterns at points 1 and 2 confirm the Co₃O₄ coating layer (**Figure S3**). This phenomenon is originated from the complete loss of lithium in the LiCoO₂ that directly exposed with the etching solution. Inductively coupled plasma-mass spectrometry (ICP-MS) of the etched sample confirmed the lithium content of $x = 0.73$ in Li_{*x*}CoO₂ and suggested the following reaction: $\text{LiCoO}_2 + 2x \text{HF} \rightarrow 2x \text{LiF} + \text{Li}_{1-2x}\text{Co}_y\text{O}_{2+\delta} (+ x \text{H}_2\text{O})$. Residual LiF phase was removed by excess of HF solution.

Powdery X-ray diffraction pattern of the pristine sample shows a presence of O3(I)-type hexagonal α -NaFeO₂ structure, where alternating planes that contain Li and Co ions are separated by closely packed oxygen layers (**Figure. 2a**). However, the layered 3D-LiCoO₂ sample shows shifted diffraction peaks to lower diffraction angles, indicating the O3(II)-type hexagonal phase formation (**Figure. 2b**).³

²¹ The values of the estimated lattice constants a and c of the bare LiCoO₂ were 2.816 Å, and 14.043 Å, respectively ($c/a = 4.986$). The a and c values represented the distance between the interlayers (one third of c -axis in the hexagonal unit cell) and the neighbors of interlayers (metal-metal distance), a -axis in the hexagonal cell. The layered sample showed that $a = 2.806$ and $c = 14.322$ ($c/a = 5.104$), indicating a very large elongation along the c -axis. It means that there was more facile lithium intercalation in the $3a$ sites.²²⁻²³ No detection of Co₃O₄ phase from the XRD indicates that the Co₃O₄ amount formed on LiCoO₂ surface is < 1 wt%, and the coating thickness is expected to be within 5 nm based upon previous coating study.²⁴ In order to increase the coating thickness of Co₃O₄, an etching time needs to be increased. However, upon increasing the etching time beyond 60 min., severe capacity loss was observed. We believe that such a degraded performance is related to deformation of structure from the enhanced loss of lithium content x in Li _{x} CoO₂ and increased formation of Co₃O₄. Accordingly, we believe that an optimized etching time was 60 min.

X-ray photoelectron spectroscopy (XPS) results suggest the mechanism of Co₃O₄ formation. Typically, Co $2p$ spectra of bare LiCoO₂ show clearly the $2p_{3/2}$ and $2p_{1/2}$ peaks at 777.5-782.5 eV and 792.5-797.5 eV, respectively.²³ If lithium ion is extracted, Co⁴⁺ peaks at 781.5, and 796.8 eV are newly developed. However, these peaks are not shown in the deconvoluted peak after chemical etching, which does not mean the oxidation from Co³⁺ to Co⁴⁺, but the presence of Co₃O₄ by the reduction from Co³⁺ to Co²⁺ state (**Figure S4**). This reduction is elucidated by the analysis of O $1s$ spectra of Co₃O₄. O $1s$ spectra of Co₃O₄ peaks suggest generally all oxygen associated with “2-” formal charge in the range of 527.7-530.5 eV (**Figure 3a**).²⁵ However, the peak at 531.9 eV indicates the ionization of oxygen ions (O²⁻ to O⁻) after chemical etching of bare LiCoO₂, resulting in the reduction of Co³⁺ to Co²⁺ (**Figure 3b**). The existence of O⁻ species is possible to form the covalent bond of Co²⁺ and oxygen. Therefore, the Co₃O₄ could be formed on the surface of LiCoO₂ by chemical etching.

Figure 4a shows the cell voltage profiles of the pristine and the layered 3D-LiCoO₂ cathodes with increasing discharge C-rates from 1 to 7C in a 2016 R-type lithium half-cell between 3 and 4.6V (1C corresponds to 150 mA g⁻¹ and charge rate was set at 0.1C). From the voltage profiles, it is evident that the capacity retention of the pristine is significantly improved by the chemical etching at higher C rates. The layered 3D-LiCoO₂ shows the discharge capacities of 183, 174, 162 and 142 mAh g⁻¹ at 1, 3, 5 and 7 C rates, respectively, and capacity retention at 7C is 78%. This cell test was conducted in an electrode density of 3.5 g/cc with containing only 5 wt% carbon black. Previous studies on nanostructured LiCoO₂ ignored the importance of the electrode density and used > 30 wt% carbon black, which is 6 times larger than the amount used in this study. For instance, the 3D desert-rose form of the LiCoO₂ particles with a size > 10 μm that was hydrothermally prepared at 200 °C showed 110 mAh g⁻¹ at a rate of 7C.²⁶ Chen et al. reported 1D plate-like LiCoO₂ nanoparticles with a size of 20-100 nm after being prepared at 600 °C. The cathode showed a first discharge capacity of 130 mAh g⁻¹ and decreased to ~100 mAh g⁻¹

after 14 cycles at a rate of 1000 mAh g⁻¹.²⁷ Under a same test condition of the layered sample, the pristine sample shows rapid capacity decaying at higher rates with 174, 140, 98 and 64 mAh g⁻¹, respectively. Note that the capacity of the layered 3D-LiCoO₂ exhibits ~2.2 times higher than that of bare LiCoO₂ at a 7 C rate. The average working voltage (the voltage corresponding to the half value of the discharge capacity) has also the same tendency to the discharging capacity. An average working is affected by the cell polarization and IR drop, which lead to working voltage decrease. The rate capability of bulk sized cathodes is generally low due to the high level of polarization at high charge/discharge rates. Therefore, nanostructured ball and flakes were introduced to overcome these shortcomings. This strategy was highly effective in greatly enhancing average working voltage of the cathode materials, as evidenced by **Figure 4**. 3D-LiCoO₂ exhibits much improved average working voltages at higher C rates, showing 3.94, 3.82, 3.68, and 3.53 V at 1, 3, 5 and 7C, respectively. However, the pristine exhibits 3.88, 3.62, 3.49, and 3.29 V (**Figure 4a. inset**). Also, note that smaller IR drops in the layered 3D-LiCoO₂ than that of the pristine which has high polarization at high discharge rate resulting from slow lithium diffusion or low electric conductivity in the active materials. These results indicate that the layer-by-layered 3D-LiCoO₂ have a larger surface contact area with the electrolytes, which can facilitate fast Li-ion transport into the structure. In addition, an increased interlayer distance between the layers that can increase the facile Li-ion transport into the structure is also important factor. **Figure 4b** exhibits a plot of the discharge capacity of the pristine and the etched samples in coin-type half cells at 21 °C under 1C rate cycling between 3 and 4.6V (charge and discharge rates are same). Note that capacity retention of the layered 3D-LiCoO₂ is significantly improved after 50 cycles, showing 62.3 %. However, the pristine sample shows only 24%. This result is indicative of showing a role of Co₃O₄ coating layer, which not only minimizes the Co⁴⁺ dissolution at higher voltages in spite of formation of highly reactive layered morphology with the electrolytes, but also Co₃O₄ prevents the side reactions with the electrolytes.²⁸

4. Conclusion

In conclusion, we developed a simple method for modifying the pristine to the 3D-LiCoO₂ cathode material with concurrent formation of nanoscale Co₃O₄ coating layer via chemical etching. After etching treatment, bare LiCoO₂ turned into 3D-LiCoO₂ consisting of layer-by-layer structures. Significantly improved electrochemical properties even at 4.6V were based on the formation of Co₃O₄ coating layer that reduced the Co⁴⁺ dissolution. The layered 3D-LiCoO₂ promotes fast Li-ion pathways for lithium ion transport and electronic conduction, thus improved rate capabilities are seen compared to the pristine.

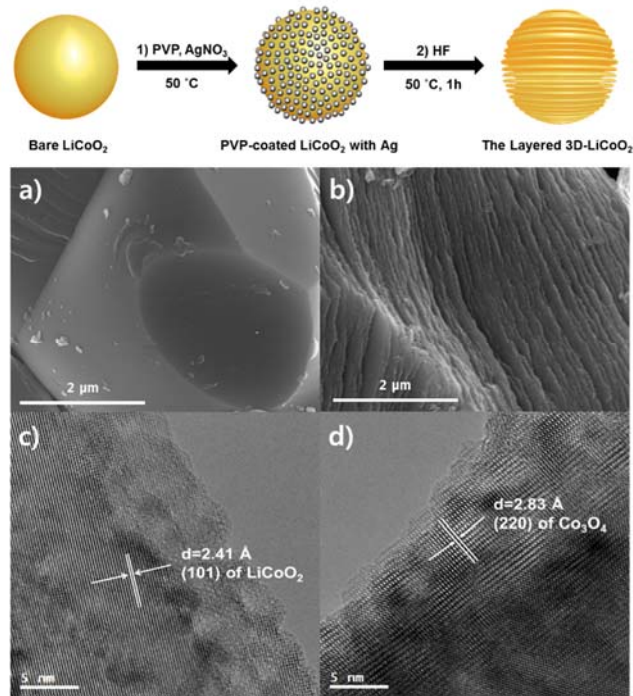


Figure 1. Upper: Schematic view of preparation of the pristine to the layered 3D-LiCoO₂ cathode material: 1) the loading Ag particle on the surface of PVP-coated LiCoO₂ by reduction from Ag⁺ ions, 2) the formation of potholes by chemical etching in HF solution. Lower: a) SEM image of bare LiCoO₂, b) SEM image of the layered 3D-LiCoO₂ and c, d) TEM images of bare LiCoO₂ and the as-etched LiCoO₂, respectively, after etching in HF solution for 1 h, followed by vacuum drying at 120 °C for overnight.

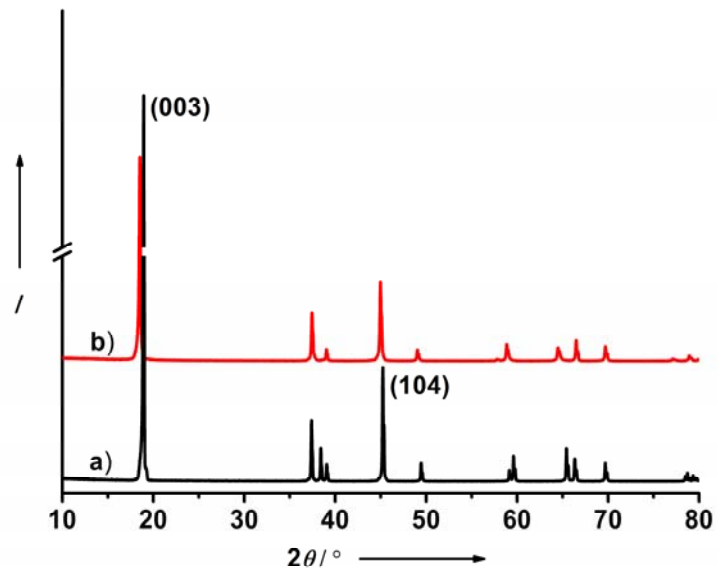


Figure 2. Powdery X-ray diffraction patterns of a) the pristine, and b) the layered 3D-LiCoO₂.

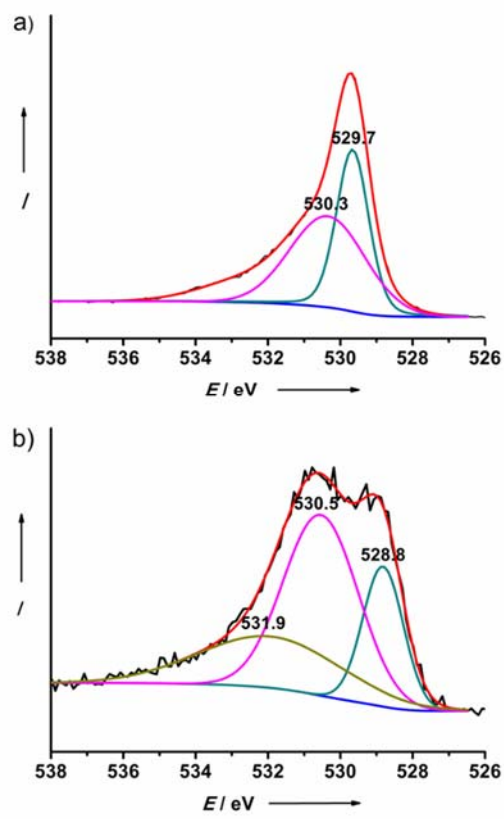


Figure 3. O1s XPS spectra of a) Co₃O₄ and b) the layered 3D-LiCoO₂.

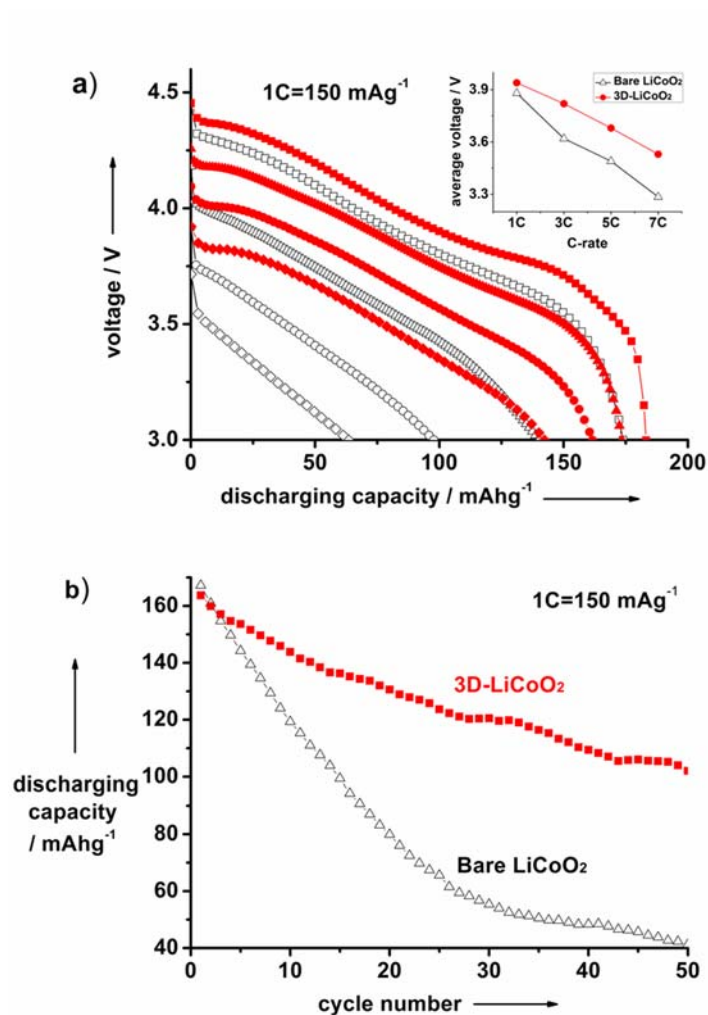


Figure 4. Electrochemical evaluation of bare LiCoO₂ (black) and the layered 3D-LiCoO₂ (red). a) voltage profiles at 1 (square), 3 (triangle), 5 (circle) and 7 C (diamond) rate between 3 and 4.6 V in coin-type lithium half cells (2016R-type) (inset: average voltage at each C-rate), b) plot of discharging capacity vs. cycle number at a rate of 1 C (triangle: bare LiCoO₂, square: the layered 3D-LiCoO₂)

Supporting Information

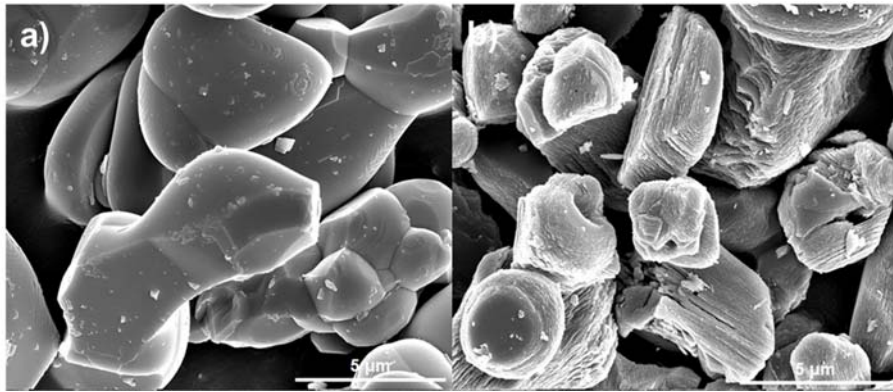


Figure S1. The low magnification SEM images of a) bare LiCoO₂ and b) as-etched 3D-LiCoO₂.

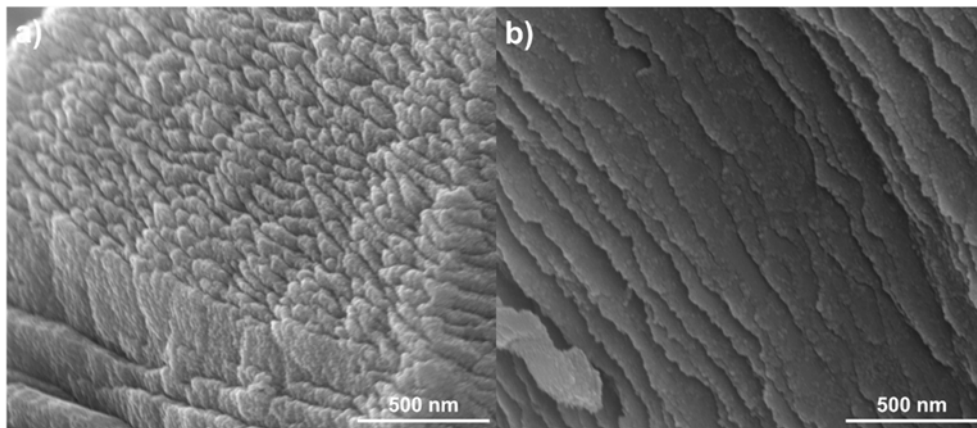


Figure S2. a) The etched LiCoO₂ without the continuous Ag⁰ alignment, b) the layered 3D-LiCoO₂ with the continuous Ag⁰ alignment.

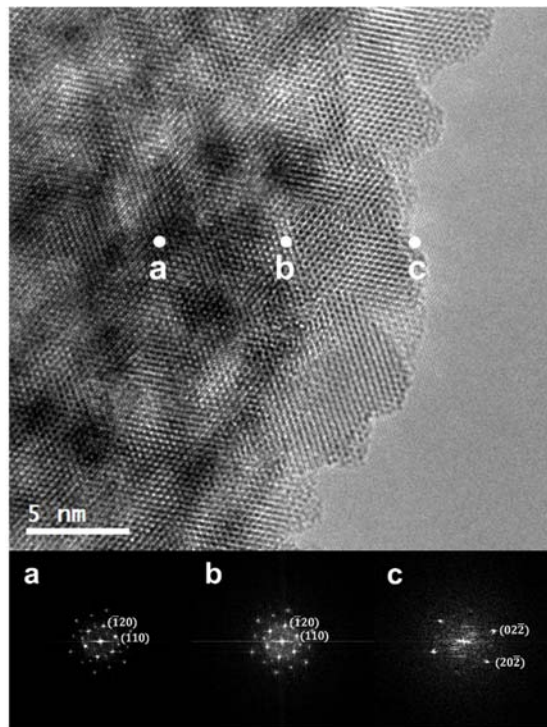


Figure S3. TEM image of as-etched LiCoO_2 and fast-fourier transform (FFT) images of a, b, and c areas.

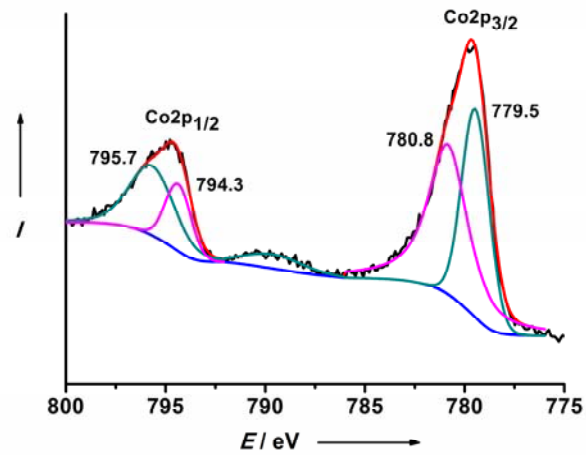


Figure S4. The deconvolution of XPS spectrum of Co_{2p} region of 2D-LiCoO₂.

References

1. Jo, M.; Jeong, S.; Cho, J., High power LiCoO₂ cathode materials with ultra energy density for Li-ion cells. *Electrochem. Commun.* **2010**, *12* (7), 992-995.
2. *LIB-related Study Program 09-10*; Institute of Information Technology: Tokyo, Japan.
3. Mizushima, K.; Jones, P. C.; Wiseman, P. J.; Goodenough, J. B., Li_xCoO₂ (0 < x ≤ 1): A new cathode material for batteries of high energy density. *Mater. Res. Bull.* **1980**, *15* (6), 783-789.
4. Jan, N. R.; Dahn, J. R., Electrochemical and In Situ X-Ray Diffraction Studies of Lithium Intercalation in Li_xCoO₂. *J. Electrochem. Soc.* **1992**, *139* (8), 2091-2097.
5. Wang, B.; Bates, J. B.; Hart, F. X.; Sales, B. C.; Zuhr, R. A.; Robertson, J. D., Characterization of Thin-Film Rechargeable Lithium Batteries with Lithium Cobalt Oxide Cathodes. *J. Electrochem. Soc.* **1996**, *143* (10), 3203-3213.
6. Cho, J.; Kim, Y. J.; Park, B., Novel LiCoO₂ Cathode Material with Al₂O₃ Coating for a Li Ion Cell. *Chem. Mater.* **2000**, *12* (12), 3788-3791.
7. Amatucci, G. G.; Tarascon, J. M.; Klein, L. C., Cobalt dissolution in LiCoO₂-based non-aqueous rechargeable batteries. *Solid State Ionics* **1996**, *83* (1-2), 167-173.
8. Kim, B.; Lee, J.-G.; Choi, M.; Cho, J.; Park, B., Correlation between local strain and cycle-life performance of AlPO₄-coated LiCoO₂ cathodes. *J. Power Sources* **2004**, *126* (1-2), 190-192.
9. Ohzuku, T.; Ueda, A., Solid-State Redox Reactions of LiCoO₂ (R-3m) for 4 Volt Secondary Lithium Cells. *J. Electrochem. Soc.* **1994**, *141* (11), 2972-2977.
10. Cho, J.; Kim, Y. J.; Kim, T.-J.; Park, B., Zero-Strain Intercalation Cathode for Rechargeable Li-Ion Cell. *Angew. Chem. Int. Ed.* **2001**, *40* (18), 3367-3369.
11. Wang, Z.; Liu, L.; Chen, L.; Huang, X., Structural and electrochemical characterizations of surface-modified LiCoO₂ cathode materials for Li-ion batteries. *Solid State Ionics* **2002**, *148* (3-4), 335-342.
12. Kim, Y. J.; Kim, H.; Kim, B.; Ahn, D.; Lee, J.-G.; Kim, T.-J.; Son, D.; Cho, J.; Kim, Y.-W.; Park, B., Electrochemical Stability of Thin-Film LiCoO₂ Cathodes by Aluminum-Oxide Coating. *Chem. Mater.* **2003**, *15* (7), 1505-1511.
13. Fang, T.; Duh, J. G.; Sheen, S. R., Improving the electrochemical performance of LiCoO₂ cathode by nanocrystalline ZnO coating. *J. Electrochem. Soc.* **2005**, *152* (9), A1701-A1706.
14. Kim, M. G.; Cho, J., Reversible and High-Capacity Nanostructured Electrode Materials for Li-Ion Batteries. *Adv. Funct. Mater.* **2009**, *19* (10), 1497-1514.
15. Fu, L. J.; Liu, H.; Li, C.; Wu, Y. P.; Rahm, E.; Holze, R.; Wu, H. Q., Surface modifications of electrode materials for lithium ion batteries. *Solid State Sciences* **2006**, *8* (2), 113-128.

16. Song, H.-K.; Lee, K. T.; Kim, M. G.; Nazar, L. F.; Cho, J., Recent Progress in Nanostructured Cathode Materials for Lithium Secondary Batteries. *Adv. Funct. Mater.* **2010**, *20* (22), 3818-3834.
17. Cheng, F.; Tao, Z.; Liang, J.; Chen, J., Template-Directed Materials for Rechargeable Lithium-Ion Batteries. *Chem. Mater.* **2007**, *20* (3), 667-681.
18. Li, X.; Cheng, F.; Guo, B.; Chen, J., Template-Synthesized LiCoO₂, LiMn₂O₄, and LiNi_{0.8}Co_{0.2}O₂ Nanotubes as the Cathode Materials of Lithium Ion Batteries. *J. Phys. Chem. B* **2005**, *109* (29), 14017-14024.
19. Jiao, F.; Shaju, K. M.; Bruce, P. G., Synthesis of Nanowire and Mesoporous Low-Temperature LiCoO₂ by a Post-Templating Reaction. *Angew. Chem. Int. Ed.* **2005**, *44* (40), 6550-6553.
20. Peng, K.; Wu, Y.; Fang, H.; Zhong, X.; Xu, Y.; Zhu, J., Uniform, Axial-Orientation Alignment of One-Dimensional Single-Crystal Silicon Nanostructure Arrays. *Angew. Chem. Int. Ed.* **2005**, *44* (18), 2737-2742.
21. Croguennec, L.; Pouillier, C.; Mansour, A. N.; Delmas, C., Structural characterisation of the highly deintercalated Li_xNi_{1.02}O₂ phases (with $x < 0.30$). *J. Mater. Chem.* **2001**, *11* (1), 131-141.
22. Lee, H.; Kim, Y.; Hong, Y.-S.; Kim, Y.; Kim, M. G.; Shin, N.-S.; Cho, J., Structural Characterization of the Surface-Modified Li_xNi_{0.9}Co_{0.1}O₂ Cathode Materials by MPO₄ Coating (M = Al, Ce, SrH, and Fe) for Li-Ion Cells. *J. Electrochem. Soc.* **2006**, *153* (4), A781-A786.
23. Dupin, J. C.; Gonbeau, D.; Martin-Litas, I.; Vinatier, P.; Levasseur, A., Lithium intercalation/deintercalation in transition metal oxides investigated by X-ray photoelectron spectroscopy. *J. Electron Spectrosc. Relat. Phenom.* **2001**, *120* (1-3), 55-65.
24. Cho, J.; Kim, Y.-W.; Kim, B.; Lee, J.-G.; Park, B., A Breakthrough in the Safety of Lithium Secondary Batteries by Coating the Cathode Material with AlPO₄ Nanoparticles. *Angew. Chem. Int. Ed.* **2003**, *42* (14), 1618-1621.
25. Dupin, J.-C.; Gonbeau, D.; Vinatier, P.; Levasseur, A., Systematic XPS studies of metal oxides, hydroxides and peroxides. *Phys. Chem. Chem. Phys.* **2000**, *2* (6), 1319-1324.
26. Chen, H.; Grey, C. P., Molten Salt Synthesis and High Rate Performance of the “Desert-Rose” form of LiCoO₂. *Adv. Mater.* **2008**, *20* (11), 2206-2210.
27. Chen, H.; Qiu, X.; Zhu, W.; Hagenmuller, P., Synthesis and high rate properties of nanoparticled lithium cobalt oxides as the cathode material for lithium-ion battery. *Electrochem. Commun.* **2002**, *4* (6), 488-491.
28. Cho, Y.; Cho, J., Significant Improvement of LiNi_{0.8}Co_{0.15}Al_{0.05}O₂ Cathodes at 60 °C by SiO₂ Dry Coating for Li-Ion Batteries. *J. Electrochem. Soc.* **2010**, *157* (6), A625-A629.

* Chapter III is reproduced in with a permission of “Jeong, S.; Park, S.; Cho, J., High-Performance, Layered, 3D-LiCoO₂ Cathodes with a Nanoscale Co₃O₄ Coating via Chemical Etching. *Advanced*

Energy Materials 2011, 1 (3), 368-372". Copyright **2011** Wiley-VCH Verlag GmbH & Co. KGaA, Weinheim.

Chapter IV

Etched Graphite with Internally Grown Si Nanowires from Pores as an Anode for High Density Li-Ion Batteries

1. Introduction

In these days, to meet the requirements for usages in hybrid electric vehicles (HEVs) and plug-in hybrid electric vehicles (PHEVs) as well as high energy storage system, the increasing energy density has been a key issue in rechargeable lithium ion batteries.¹⁻² Currently available commercial Li-ion cell (~150 Wh/kg based on mass of battery pack) consisting of LiCoO₂ and graphite as cathode and anode, respectively, cannot meet with the electrically powered applications which require higher cell operating voltage and/or capacity.³ On cathode side, for example, although the surface chemistry plays a key role of solving an intrinsic problem such as capacity fade, the available capacity of Li_xMO₂ (M = transition metal) is limited to < 200 mAh/g with a cut-off voltage of 4.3V.^{2,4}

To be concomitant with increasing the capacity of cathode materials, the alternative high capacity anode materials instead of graphite (372 mAh/g) should be considered to balance the cell. Among various kinds of anode candidates, silicon (Si) has been intensively paid attention to the alternative material to achieve high gravimetric capacity, 3579 mAh/g for Li₁₅Si₄ at room temperature (RT). However, despite of its capacity merit, it has severe drawback, i.e., large expansion and contraction during cycling ($\text{Si} + x \text{Li}^+ + x \text{e}^- \leftrightarrow \text{Li}_x\text{Si}$).⁵⁻⁸ This volume change (> 300% at RT) leads to pulverization, resulting in contact loss between current collector and carbon black and active particles. This loss eventually resulted in a significant capacity loss during cycling.

In order to circumvent this problem, various nano-engineering strategies have been proposed to minimize the volume-related problems using Si nanoparticles,⁹ yolk-shell Si nanoparticle,¹⁰ Si nanoparticles in nitrogen-doped carbon sphere,¹¹ Si nanowires,¹² carbon coated Si nanowires,¹³ Si nanotubes,¹⁴ 3D porous Si nanoparticles,¹⁵ and porous Si-C composites.¹⁶ Although these strategies exhibited very high capacity and good cycle stability, considering very low of electrode density (< 0.9 g/cm³) of Si upon fully lithiation, the composite with graphite (1.7 g/cm³) is the most efficient way to reach high energy density.

In this regard (also, as shown in Table S1), physical blending of graphite and Si has been widely considered to produce Si/graphite composites, but this method led to a capacity decrease during cycling due to the contact loss between electrode materials.¹⁷⁻¹⁸ Also, the chemically bridged Si/graphite composite with phenyl group was reported to overcome a capacity retention, but it also showed a rapid

capacity fading from 1052 mAh/g at 2nd cycle to 540 mAh/g at 50th cycle with capacity retention of 52 %.¹⁹

Herein, we report a novel architecture consisting of Si nanowires internally grown from pores in the etched graphite particles (namely, SiNWs-PG) with a high electrode density of 1.5 g/cm³. These novel composites demonstrate high volumetric capacity density of 1363 mAh/cm³ with 90% coulomb efficiency and high rate capability of 568 mAh/cm³ at 5C rate. One of the uniqueness of these composites is that porous graphite structure can offer free space to accommodate the volume change of internal embedded Si nanowires, and provide a fast electron transfer pathway between graphite and Si, resulting in the improved electrochemical performance.

2. Experimental section

2.1. The preparation of Si nanowires embedded in porous graphite

For polymer solution containing Ni ion, 1 wt% polystyrene-*b*-poly(2-vinylpyridine) (PS-*b*-P2VP, M_n PS=440 kg mol⁻¹, M_n P2VP=353 kg mol⁻¹, Polymer Source) was dissolved in tetrahydrofuran (THF)/toluene (2:8, v/v) for 24 h, followed by the addition of NiCl₂·6H₂O. Bare graphite was stirred in the prepared polymer solution for 2 h, then, the as-prepared samples were precipitated in excess hexane. The obtained powders were dried at 100 °C for 24h. To produce porous graphite, the obtained samples were annealing at 500 °C for 20 min under Ar atmosphere (100 sccm) for Ni nanoparticles formation, then etched at 1000 °C for 1 h under H₂ flow (100 sccm) for porous structure. To replace the remaining Ni nanoparticle with Au as catalyst for Si nanowires growth, the porous graphite with Ni nanoparticles was immersed in 10 ml of 0.001M HAuCl₄·3H₂O solution, followed by washing with several times and drying at 110 °C. Then, SiH₄ was introduced into the tube furnace at 550 °C for 30 min with 25 sccm (The SiC products were produced at same flow condition without catalyst exchange).

2.2. Fabrication of lithium ion half-cell

The electrode for half-cell tests was made of bare graphite, porous graphite, SiNWs-BG and SiNWs-PG as active materials, styrene butadiene rubber (SBR) and sodium carboxymethyl cellulose (CMC) as binder in a weight ratio of 85:5:10 without any conductive materials. The homogenous slurry are spread onto a copper foil, and dried at 110 °C for 1 h. The coin-type half-cells (2016R) contained active materials with 1.5 g/cm³, Li metal as counter electrode, and polyethylene separator and electrolyte solution of 1.15 M LiPF₆ in ethylene carbonate (EC): ethyl methyl carbonate (EMC): dimethyl carbonate (DMC) = 3:4:3 vol.% with 5% fluoroethylene carbonate (FEC) (Panax starlyte, Korea).

3. Results and discussion

Figure 1 shows a schematic view of the synthesis process of SiNWs-PG. First, spherical micelles bearing Ni ions on graphite (~20 μm diameter) were prepared by the selective complex formation of Ni ions and pyridine unit in a polystyrene-*b*-poly(2-vinylpyridine) (PS-*b*-P2VP) block copolymer. The micelle formation was induced by the difference in solubility between PS and Ni ion bearing P2VP in a selective solvent for PS, in which spherical micelles consisting of PS corona and P2VP core were formed in solution.²⁰ The micelles containing Ni ions were then transformed to self-assembled Ni nanoparticles after removal of polymer by heat treatment at 500 °C, followed by etching process in hydrogen atmosphere at 1000 °C for 1h.²¹ As a final step, Si nanowires were grown in 3D-interconnected pores of graphite particles via Vapour-Liquid-Solid (VLS) process after exchange of catalyst from Ni to Au. The morphology of porous graphite and internally grown SiNWs was characterized by scanning electron microscopy (SEM). The Ni ion containing micelles deposited uniformly with a size of 30~40 nm on the graphite particle surface can be observed (**Figure 1b**). The as-prepared samples were annealed at 500 °C for 20 min to form Ni nanoparticles. Note that the catalytic gasification of carbon, called etching process, is more favorable at edge plane rather than basal plane of graphene.²¹ Therefore, microcarbon microbeads (MCMB) with the lamellar structure were used as a graphite source.²² At 1000 °C, Ni nanoparticles on the graphite surface etch the edge plane via catalytic hydrogenation reaction ($\text{Ni} + \text{C}_{\text{graphite}} + 2 \text{H}_2 \rightarrow \text{Ni} + \text{CH}_4$), where carbon atoms are absorbed into the Ni nanoparticles by carbon dissociation from graphene edge, resulting in a formation of porous structures with the remaining Ni nanoparticles (**Figure 1c**). As a result of etching process, graphite loses up to 20% of its original weight and the pore sizes ranging from 200 nm to 1 μm were obtained, whereas the specific surface area was increased to 6.5 m²/g compared to bare sample (1.2 m²/g). The cross-sectioned images in **Figure S1** showed the pores developed inside MCMB prepared by hydrogenation accompanying nickel penetration. As a second step, Si NWs in a scalable manner were grown in the porous graphite via VLS process. In VLS process, the catalyst plays an important constituent to serve as a preferential site for crystal nucleation and growth. If porous graphite with residual nickel is exposed at above the Ni-Si eutectic temperature,²³ Si nanowires can be expected to grow from the inside pores by SiH₄ gas decomposition. Upon annealing at 1200°C, the nanowires were starting to grow. However, X-ray diffraction (XRD) patterns revealed that silicon carbide (SiC) was formed with Ni-Si alloy as liquid droplet on the tip of the nanowires (**Figure S2**). As a consequence, lower annealing temperatures are required to prevent SiC formation, therefore, Ni catalyst is needed to be replaced with Au because the eutectic point of Au-Si alloy can suppress SiC product. Considering the standard reduction potential between nickel and gold, Ni was dissolved in 1mM H₂AuCl₄·H₂O solution via a galvanic displacement reaction, and Au was deposited on the porous graphite at the same time. After exchanging a catalyst, porous graphite with Au was annealed at 550°C under SiH₄ flowing with 25 sccm for growing Si nanowires. As can be seen from SEM images in **Figure 1d**, Si nanowires are grown from porous

graphite. In the controlled experiment (SiH_4 flow with 15 sccm at 550 °C for 30 min) to observe the evidence for the Si NWs grown from the pores in the etched graphite (**Figure S3a and b**), it can be clearly seen that Si nanowires are well grown from the pores. TEM results revealed that the catalyst are clearly shown on the top of Si nanowires and crystalline Si nanowires in SiNWs-PG is covered with 1~2 nm amorphous SiO_2 which is naturally produced after air exposure (**Figure S3c and d**).

To understand the variation of graphite structure after hydrogenation process, it is characterized by XRD and Raman spectroscopy. **Figure 2a** shows a comparison of XRD patterns between bare and porous graphite. Note that the intensity ratio of (002) to (110) peaks at 26.4°, 77.4°, respectively, is indicative of the orientation degree of graphitic layers. Bare graphite has the value of 120.2 while the hydrogenated sample has the value of 46.5, which means that graphitic layers in porous graphite are less oriented with the more exposure of edge planes.²⁴ Also, Raman spectra (**Figure 2b**) displays two major peaks at $\sim 1350 \text{ cm}^{-1}$ and $\sim 1580 \text{ cm}^{-1}$, which are assigned to D band and G band, respectively. In general, D band is related to a breathing mode of A_{1g} symmetry and this peak is not shown in perfect graphite structure. It becomes only active if the structure has the presence of disorder. Also, G band is attributed to E_{2g} symmetry, which is associated with the in-plane bond stretching of sp^2 hybridized carbons.²⁵ I_D/I_G ratio of porous graphite is 1.69 compared to bare graphite, 0.55, indicating that the disordered structure of sp^2 carbon is well developed in porous graphite. Also, this result is consistent with SEM image (**Figure 1c**), showing that the edge planes are highly exposed with many pores. After the exchange of catalyst exchange, and followed by Si nanowires growth, the final product is predominantly composed of crystalline Si without showing Ni and SiC, as confirmed in Figure 2c. C1s region in XPS spectra is deconvoluted into three peaks at 284.1, 284.8, and 285.1 eV, which correspond to Si-C, C in graphite, and C-H bond, respectively. Considering a bonding of SiNWs-PG, XPS C1s result suggests that Si nanowires are chemically embedded in porous graphite, which is confirmed by the peak at 284.1 eV attributed to Si-C bond (**Figure 2d**).²⁶

Considering an embedding process between Si nanowires and porous graphite, the electrochemical performance of SiNWs-PG can be expected to significantly improve compared to the directly Si nanowires grown on bare graphite (SiNWs-BG) without etching process at the same condition of Si nanowires growth as shown in Figure S4. Both samples are limited to 20 wt% silicon. Figure 3a exhibits voltage profiles of bare graphite, porous graphite, SiNWs-BG and SiNWs-PG at 0.05C between the voltage range of 0.005~1.4 V in coin-type lithium half-cells (2016R) ($1C = 450 \text{ mA/cm}^3$ for bare and porous graphite, $1C = 1050 \text{ mA/cm}^3$ for SiNWs-BG and SiNWs-PG). The test was performed in comparable electrode density to commercially available electrode density of 1.5 g/cm^3 . As shown in Figure 3a (see **Figure S5** for specific capacity plot), the 1st volumetric charge capacity based on porous graphite is 497 mAh/cm^3 , of which value is slightly higher than bare graphite (441 mAh/cm^3). This higher capacity of the porous graphite than bare one is due to the facts that i) lithium ion diffusion can

be easily available through edge plane rather than basal plane of graphite after hydrogenation, and ii) the remaining Ni nanoparticles after hydrogenation efficiently improves the electron conduction correlated with charge transfer reaction.²² Also, SiNWs-PG is found to exhibit a higher capacity than SiNWs-BG. The 1st charge capacity of SiNWs-BG and SiNWs-PG shows 1005 mAh/cm³ with 81% coulomb efficiency and 1230 mAh/cm³ with 91% at 0.05C, respectively. The main reason for higher performance of SiNWs-PG, especially coulomb efficiency is that the chemically bonded structure in SiNWs-PG improves efficiently the electron transport and contact between active materials compared to SiNWs-BG that Si nanowires are separately placed on bare graphite. The volumetric charge capacity of SiNWs-PG shows 2.8 times greater than bare graphite, and the coulomb efficiency is comparable to bare graphite (94 %).

Figure 3b shows the cycle retention of each material shown in Figure 3a at 0.2C rate (also, see **Figure S6** for the voltage profiles of 10th, 30th, and 100th cycles). Until 15 cycles, the slight fluctuation for bare graphite may be caused by the internal resistance such as insufficient SEI formation, whereas porous graphite shows good stability resulting from the efficient Li ion diffusion through the more exposed edge plane. As a result, porous graphite shows 463 mAh/cm³ with the capacity retention of 93 %, comparable to bare graphite (416 mAh/cm³ with 94 %) after 100 cycles. For SiNWs-BG (60% cycle retention after 100 cycles), the charging capacity gradually decreased due to the poor connectivity between Si nanowires and bare graphite, which is related to the volume change within the high density electrode. While SiNWs-PG demonstrates little capacity fading after 100 cycles, showing a volumetric charge capacity of 1014 mAh/cm³ and 100 % coulomb efficiency after 10 cycles. The initial capacity decreases out to 10 cycles is originated from SEI formation on the exposure of the inner pore region.²⁷ Remarkably, without using conducting agent (carbon black), cycling stability of SiNWs-PG cycle is superior to chemically bridged Si/Graphite composites,¹⁹ blended SiNWs/graphite composites (15:85, w/w) including 20 wt% carbon black for electrode,²⁸ and comparable to physically bonded Si/B₄C/graphite composites with 40 wt% Si and 30 wt% conductive skeleton.²⁹

Figure 3c shows excellent rate capability of SiNWs-PG compared to SiNWs-BG from 0.1C to 5C, which was done at same C-rate for charging and discharging, respectively (1C = 1050 mA/cm³, see **Figure S5c** and **d** for rate capability and the voltage profile at the end cycle of each C-rate with specific capacity). The charge capacities of SiNWs-BG at the end of each rate of 0.1C, 0.2C, 0.5C, 1C, 3C, and 5C are 840 mAh/cm³, 648 mAh/cm³, 355 mAh/cm³, 169 mAh/cm³, 38 mAh/cm³ and 7 mAh/cm³, while the value of SiNWs-PG are 1175 mAh/cm³, 1054 mAh/cm³, 974 mAh/cm³, 841 mAh/cm³, 747 mAh/cm³, and 571 mAh/cm³, respectively. The capacity retention at 5C is 49 % capacity retention compared to the value at 0.1C. Also, the voltage profile of SiNWs-PG at the end cycle of each C-rate is shown in **Figure 3d**.

Based on the electrochemical performance of SiNWs-PG, the morphology maintenance and electrode of the product after cycling is well described to understand the reason for such excellent cycling stability and rate performance. SEM image of SiNWs-PG confirmed the confinement of internally grown Si nanowires in the pores (**Figure S7a and b**) and the volume expansion of SiNWs-PG electrode is limited to be only 65.5% calculated from the variation of electrode thickness with 19 μm (**Figure S7c and d**). These results confirmed that SiNWs-PG can maintain the interconnecting conductive network with the embedded Si nanowires without conductive carbon additives which is required to deliver high rate performance, resulting in the effective electron transport pathway, and porous graphite contributed the structural integrity of Si nanowires.

4. Conclusion

In conclusion, Si nanowires grown in pores in etched graphite was successfully demonstrated as a new strategy with high electrode density ($1.5\text{g}/\text{cm}^3$) for an increasing volumetric capacity of the graphite. This strategy involved the graphite hydrogenation by Ni nanoparticles for porous structure, followed by Si nanowires growth inside porous graphite by VLS process after catalyst exchange. Especially, porous graphite as a template for Si nanowires played a key role of not only providing a free space to accommodate volume change of the internally grown Si nanowires during cycling, but also providing good electron conducting pathway.

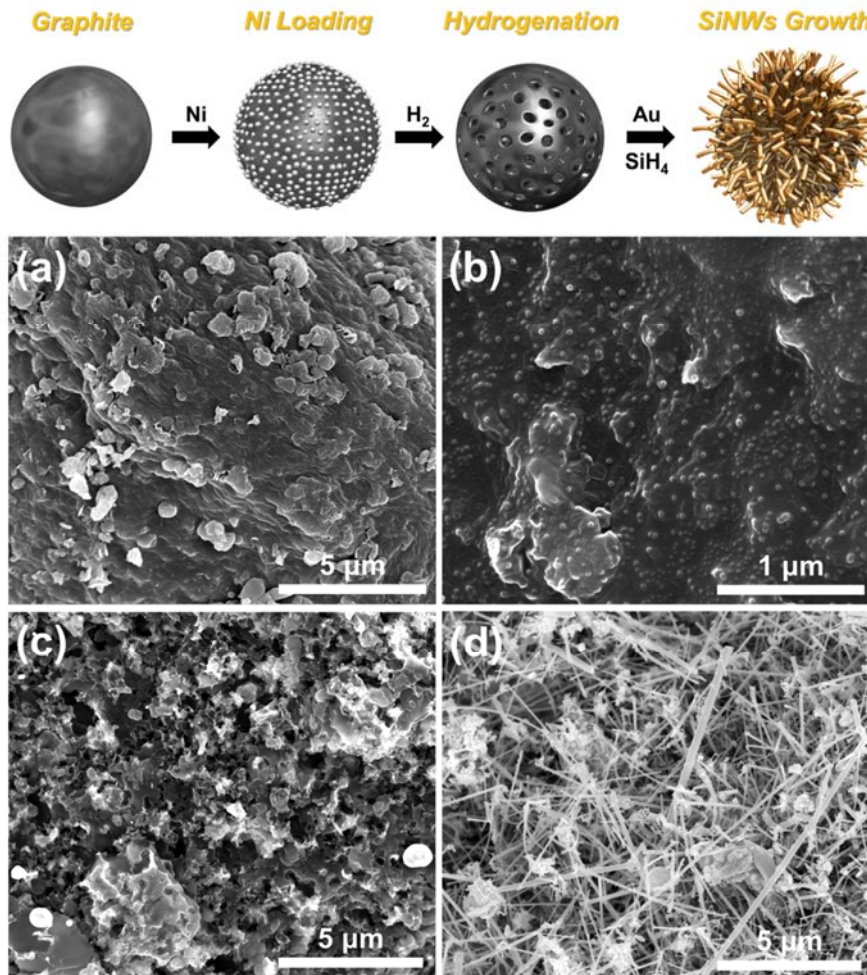


Figure 1. Top: Schematic view for the synthesis process of Si nanowires internally grown in porous graphite. Bottom: SEM images of (a) bare graphite, (b) loaded polystyrene-*b*-poly(2-vinylpyridine) micelles bearing Ni ion on graphite surface, (c) porous graphite after hydrogenation at 1000°C for 1h, and (d) Si nanowires grown from porous graphite after catalyst exchange from Ni to Au, followed by VLS process using SiH₄ at 550°C for 30 min (For low magnification images, see Figure S1).

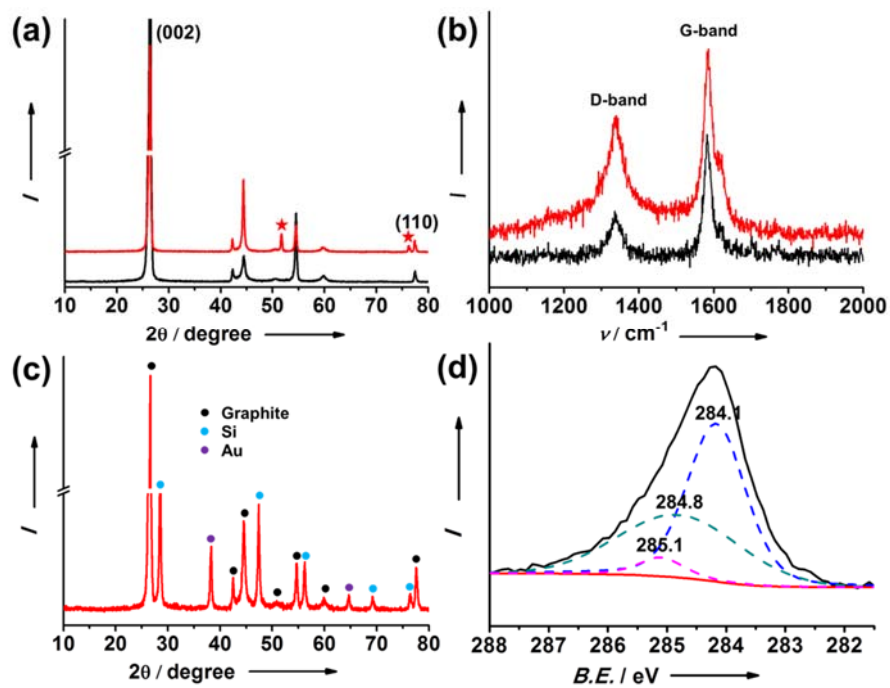


Figure 2. (a and b) XRD patterns (asterisks: Ni nanoparticles) and Raman spectra of bare graphite and porous graphite, respectively (black: bare graphite, red: porous graphite). (c and d) XRD pattern and XPS C1s spectra of SiNWs-PG. In the XPS analysis, the deconvoluted peaks at 284.1, 284.8, and 285.1 eV indicates Si-C, C in graphite, and C-H bonding, respectively.

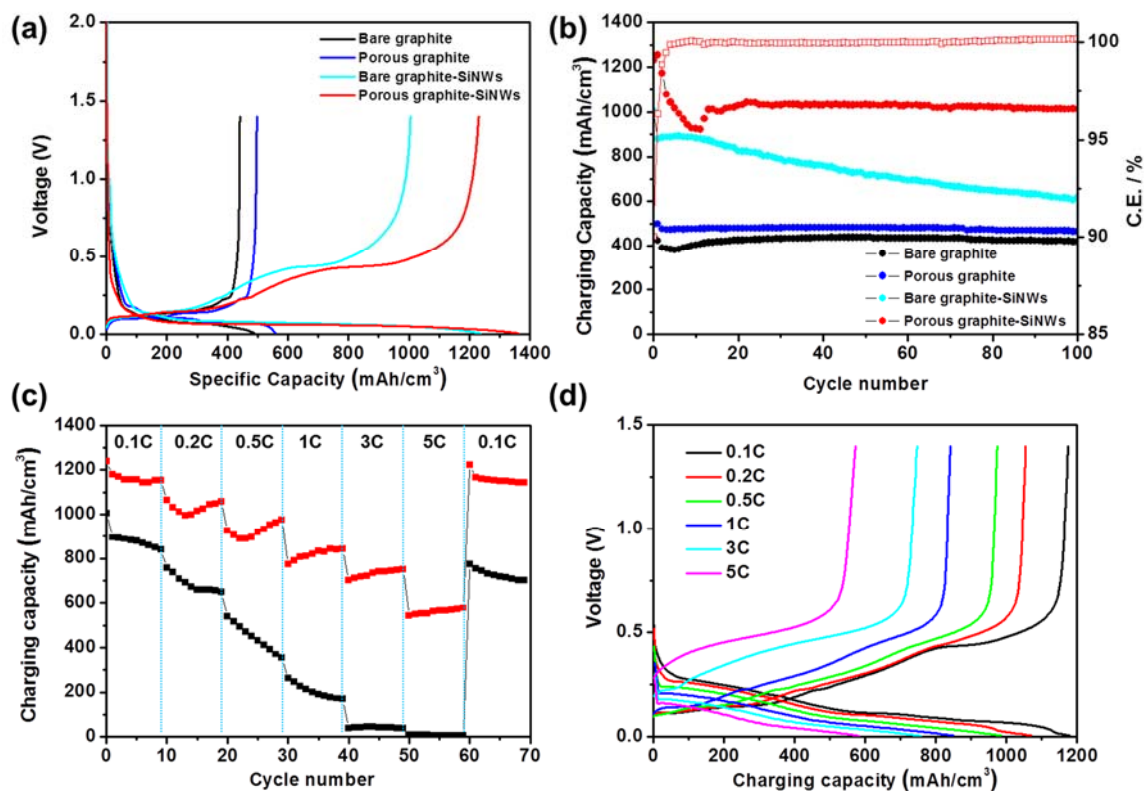


Figure 3. (a) Voltage profiles of bare graphite, porous graphite, SiNWs-BG and SiNWs-PG at 0.05C rate and (b) plot of volumetric charge (delithiation) capacity as a function of cycle number and coulomb efficiency at 0.2C rate between 0.005 and 1.4V in coin-type half-cell at 24 °C (1C = 450 mAh/cm³ for bare graphite and porous graphite, 1C = 1050 mAh/cm³ for SiNWs-BG and SiNWs-PG) (c) Rate capability of SiNWs-BG and SiNWs-PG with increasing C rate from 0.1 to 5C rate between 0.005 and 1.4V in coin-type half-cell at 24 °C and (d) voltage profiles of (c) at each C rate (charge and discharge rates were same).

Supporting Information

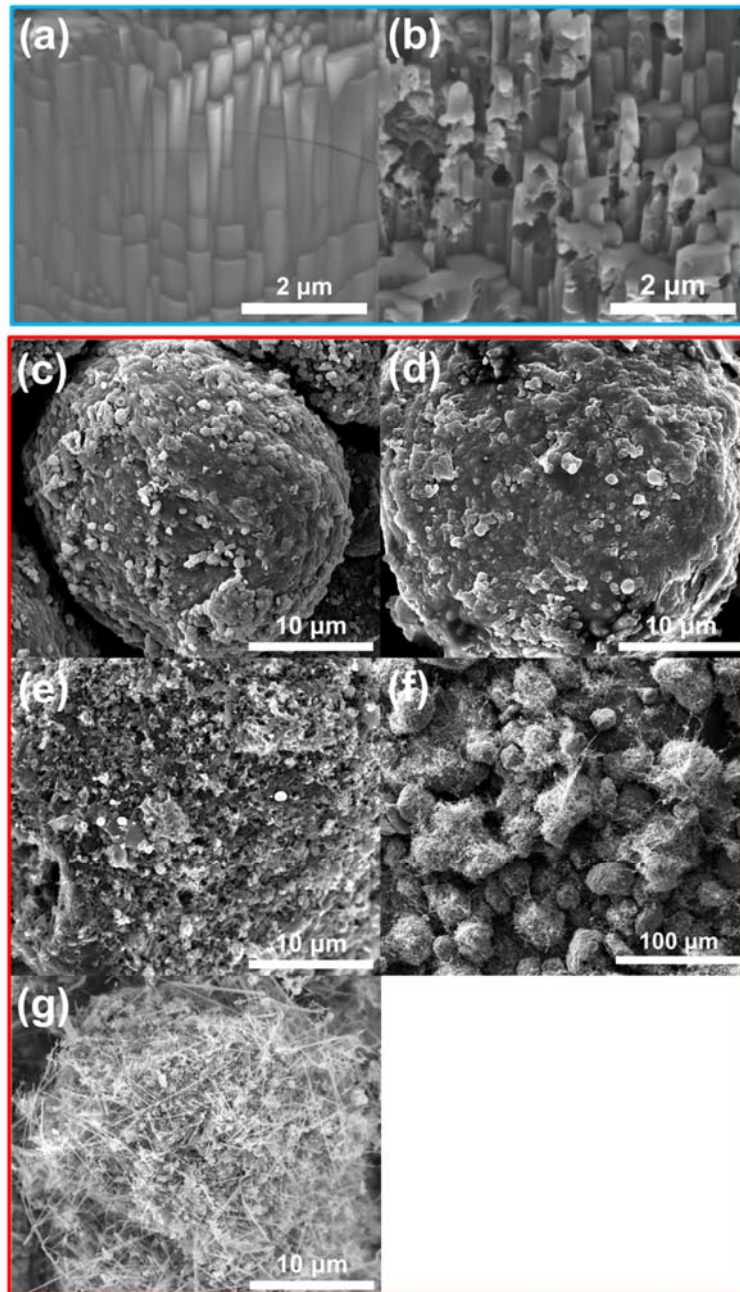


Figure S1. Cross-sectioned SEM images of (a) bare MCMB and (b) etched MCMB, and low magnified SEM images of (c) bare graphite, (d) loaded polystyrene-*b*-poly(2-vinylpyridine) micelles bearing Ni ion on graphite surface, (e) porous graphite after hydrogenation at 1000 °C for 1h, and (f and g) Si nanowires grown from porous graphite after catalyst exchange from Ni to Au, followed by VLS process using SiH₄ at 550 °C for 30 min (g is expanded image of (f)).

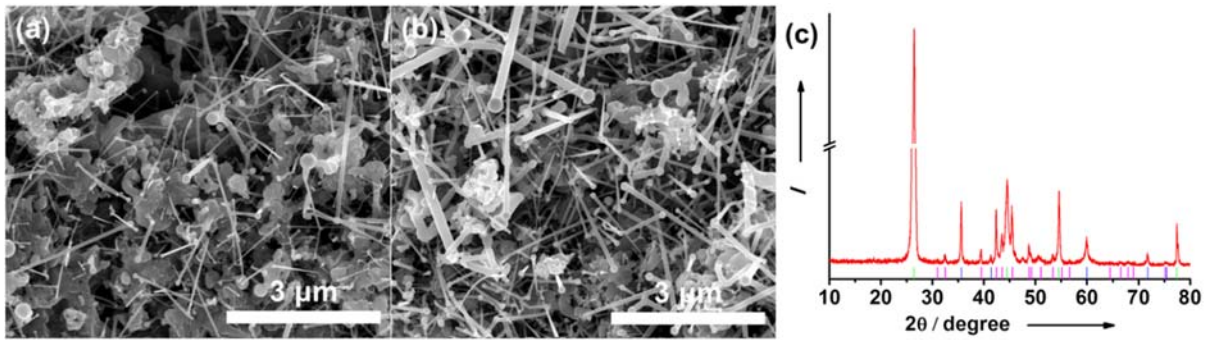


Figure S2. SEM images of SiC nanowires on porous graphite by VLS process with silane decomposition at (a) 1200 °C, (b) 1300 °C, and (c) XRD pattern of (a) sample. The peak positions corresponding to graphite (green), SiC (pink) and Ni₂Si (blue) are shown.

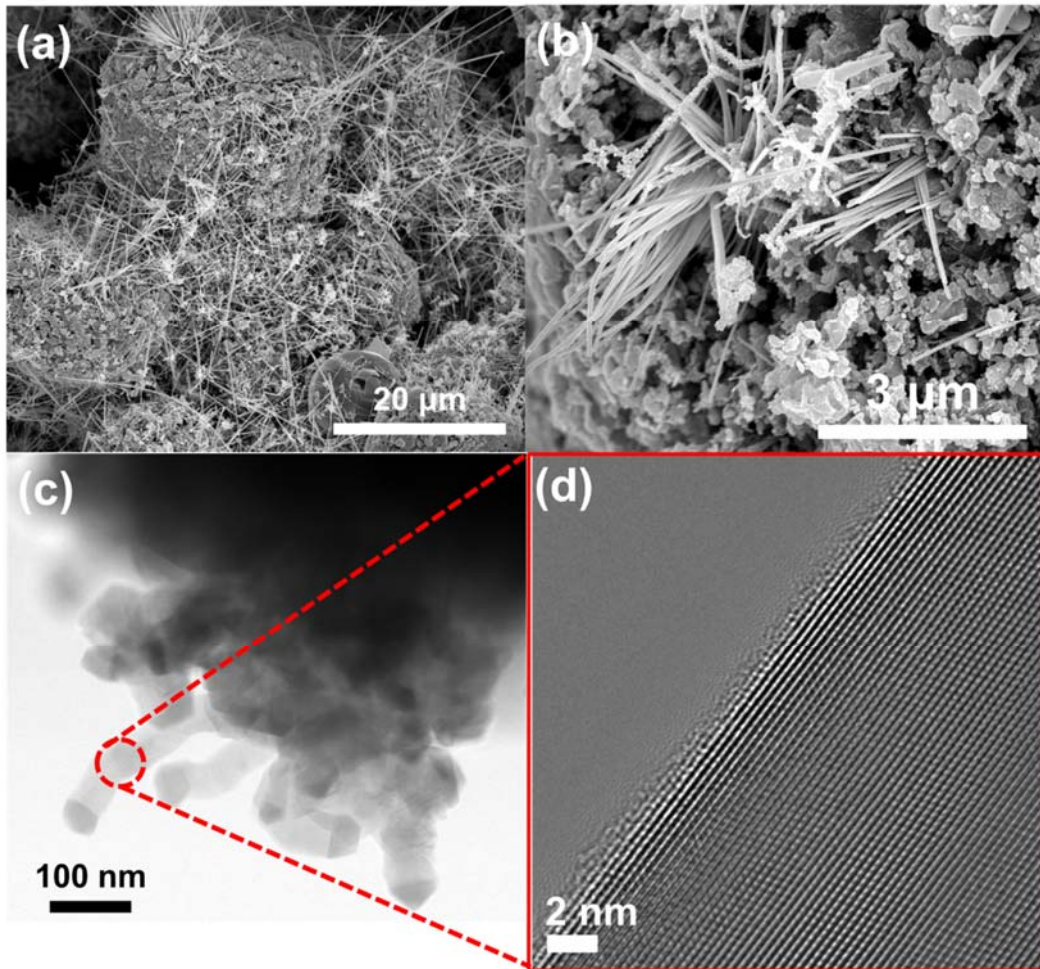


Figure S3. (a and b) SEM images of Si nanowires from the pores in the controlled experiment with SiH₄ flow with 15 sccm at 550 °C for 30 min and (c) bright-field TEM image of Si nanowires grown in porous graphite. The dark region on the top of Si nanowires indicates the alloy catalyst after VLS process. (c) highly magnified TEM image of the circled region in (b), and crystalline Si nanowire with an amorphous SiO₂ layer is shown.

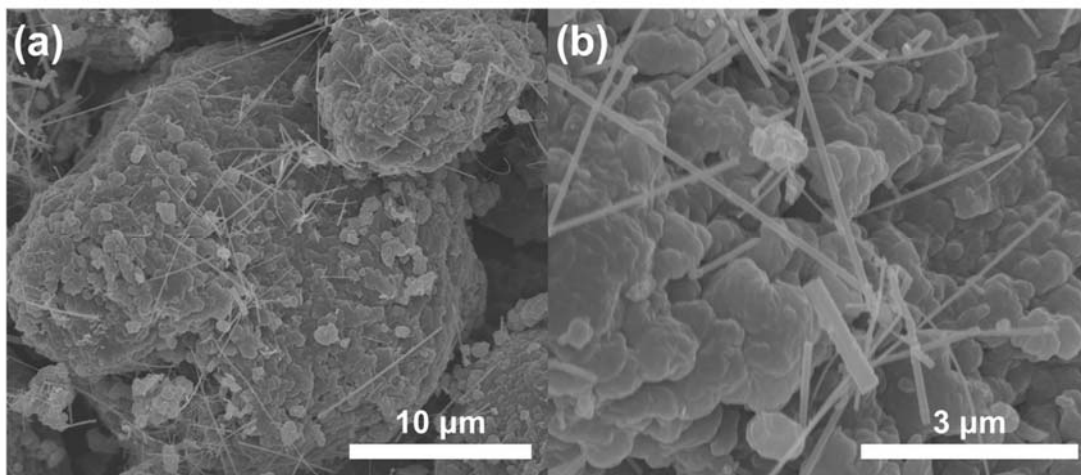


Figure S4. (a and b) the low and high magnified SEM images of the directly Si nanowires grown on bare graphite without etching process at the same condition for Si nanowire growth (SiH_4 flow with 25 sccm at 550°C for 30 min)

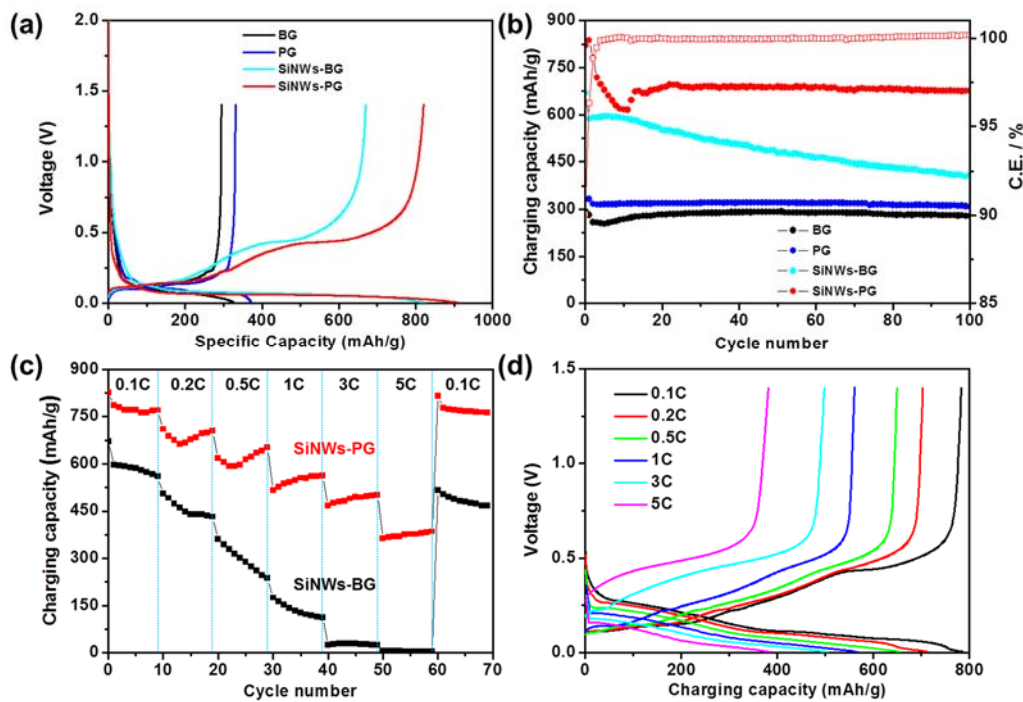


Figure S5. (a) Voltage profile of bare graphite, porous graphite, and SiNWs-PG at 0.05C rate, (b) plot of volumetric charge (delithiation) capacity as a function of cycle number and coulomb efficiency at 0.2C rate between 0.005 and 1.4V in coin-type half-cell at 24 °C (1C = 300 mA/g for bare graphite and porous graphite, 1C = 700 mAh/g for SiNWs-BG and SiNWs-PG), (c) Rate capability of SiNWs-BG (black) and SiNWs-PG (red) with increasing C rate from 0.1 to 5C rate between 0.005 and 1.4V in coin-type half-cell at 24 °C, and (d) voltage profiles of (c) at the end cycle of each C rate (charge and discharge rates were same).

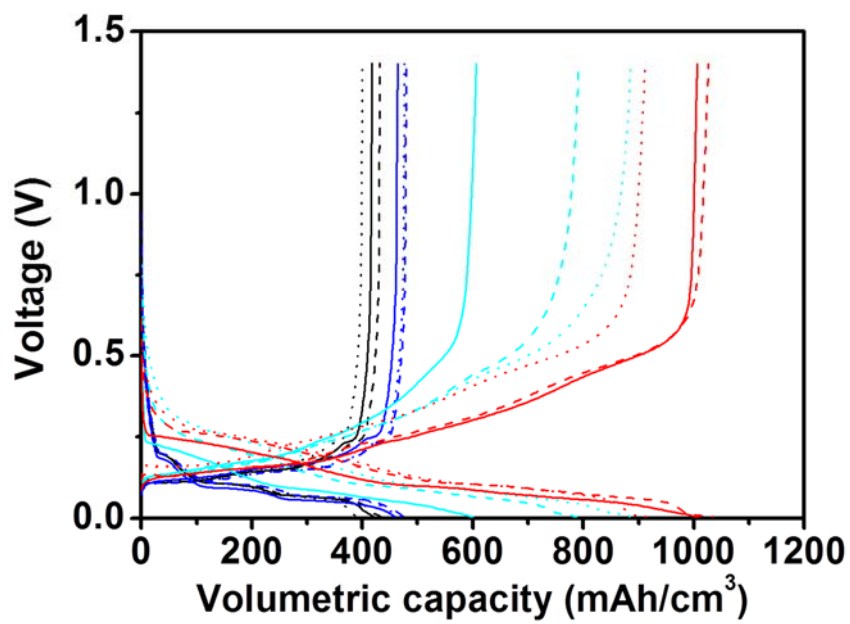


Figure S6. Voltage profiles of bare graphite (black line), etched graphite (blue line), SiNWs-BG (cyan line) and SiNWs-PG (red line) after 10th (dot), 30th (dash), and 100th (solid) cycle.

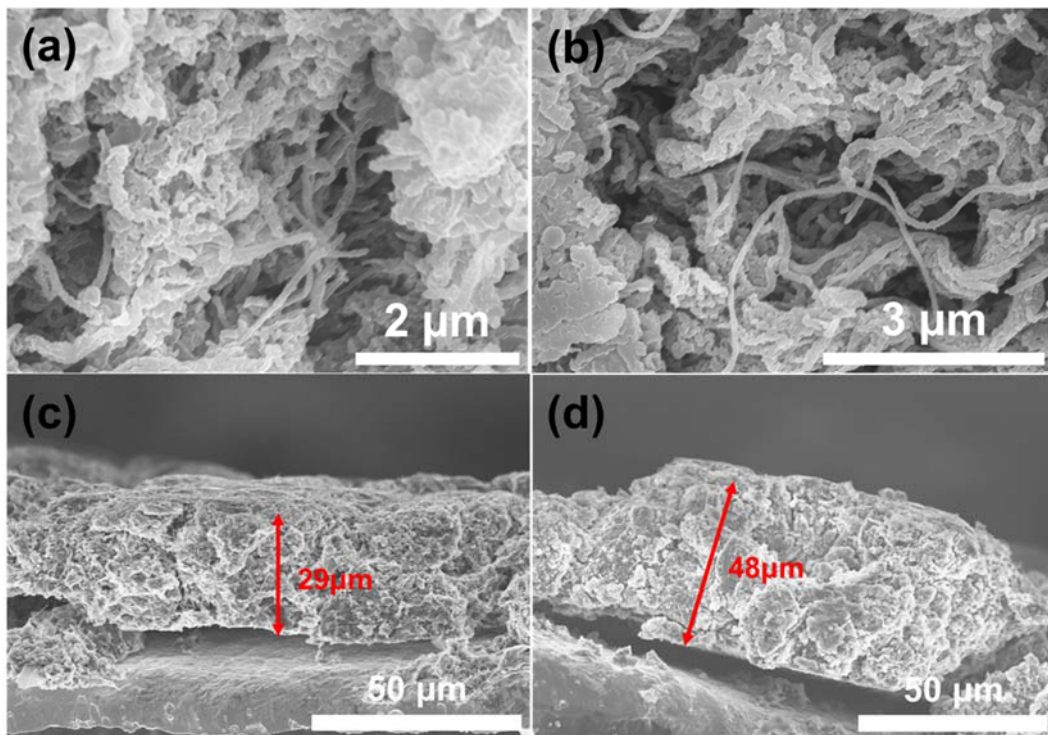


Figure S7. (a and b) SEM images of Si nanowires grown from porous graphite at different position, and cross-sectional SEM images of SiNWs-PG electrode before (c) and after (d) 100 cycling.

Table. S1. The specification and electrochemical performance of silicon/graphite composites in previous works.

Synthesis	Silicon morphology	Si contents	Loading level	Electrode density	Electrolyte	Test condition	1 st lithiation	1 st de-lithiation	C.E.	Cycle retention	Ref.
		%	mg/cm ²	g/cm ³			mAh/g	mAh/g	%		
Mechanical milling	Particles	25	6-8	-	1M LiPF ₆ in EC/DEC (1:1, w/w)	0.005-1.5V	~1050	~900	85.7	Decreasing / 33 cycles	1 ³⁰
						0.2mA/cm ² for 1 st three cycles, 0.5mA/cm ² for following cycles					
Sol-gel + ball milling	Particles	19.2	3-4	-	1M LiPF ₆ in EC/DEC (50:50, v/v)	0-1.5V at 0.21mA/cm ²	1033.7	832.2	80.5	Decreasing / 25 cycles	2 ³¹
Milling + heating	Particles	-	-	-	1M LiPF ₆ in EC/DEC (1:1, v/v)	0-1.2V at 0.2mA/cm ²	~650	~510	78.5	Stable / 40 cycles	3 ³²
Milling + heating	Particles	15	-	-	LiClO ₄ in EC+DMC (1:1, v/v)	0.02-1.5 V at 0.18mA/cm ²	~1210	~810	67	Slightly decreasing / 22cycles	4 ³³
Ball milling	Particles (on MCMB)	20	-	-	1M LiPF ₆ in EC/DMC (1:1, v/v)	0.01-3V at 0.05 mA/cm ²	1175	1066	90.7	Slightly decreasing / 25 cycles	5 ³⁴

CVD	Particles	0.050 at.% (EDX)	-	-	1M LiPF ₆ in EC/DMC (1:1, v/v)	0.035-2.0V at 40 mA/g	821	367	44.7	Stable / 30 cycles	6 ³⁵
CVD	Particles	7.1	3.5-4	-	1M LiPF ₆ in EC/DMC + 2%VC	0.005-1.0V at 50mA/g	690	520	75.4	Slightly decreasing / 140 cycles	7 ³⁶
Mechanical milling	Particle (alloy)	40	-	-	1M LiPF ₆ in EC/DEC (1:1, v/v)	0.005-1.5V at 0.1C	1160	830	71.6	Stable / 50 cycles	8 ³⁷
Milling	Particles	< 30	3.3	-	-	0.04-1.5V at 2mA/cm ²	~600	~580	96	Slightly decreasing / 40 cycles	9 ³⁸
Thermal process	Particles	20	-	-	1M LiPF ₆ in EC/DMC (1:1, v/v)	0.02-1.5V at 0.2mA/cm ²	-	-	-	Slightly decreasing / 50 cycles	10 ³⁹
Spray + thermal process	Particles (on MCMB)	10	-	-	1M LiPF ₆ in EC/EMC/D MC (1:1:1)	0-1.2V at various rate	868.1	630.9	62	Decreasing / 10 cycles	11 ⁴⁰
PECVD	Particles	2.88	-	-	1M LiPF ₆ in EC/EMC/D MC (1:1:1, v/v)	0-2V at 0.01C	-	-	78	Decreasing / 30 cycles	12 ⁴¹
Mechanoche mical milling	Particles	-	-	-	1M LiPF ₆ in EC/DEC (1:1, v/v)	0.005-1.5V	1430	1130	79	Decreasing / 50 cycles	13 ⁴²

Milling + thermal process	Particles	15	-	-	1M LiPF ₆ in EC/EMC (3:7, v/v)	0-1.5V at 0.3mA/cm ²	849	721	85	Decreasing / 15 cycles	14 ⁴³
Milling + thermal process	Particles	20	-	-	1M LiPF ₆ in EC/DMC (1:1, w/w)	0.1-1C at 0.4mA/mg	~1300	~1100	84.6	Stable / 30 cycles	15 ⁴⁴
Milling	Particles (on MCMB)	50	-	-	1M LiPF ₆ in EC/DMC (3:7, v/v)	-	~500	~310	62	Stable / 400 cycles	16 ⁴⁵
Milling	Particles	33	-	-	1M LiPF ₆ in EC/DEC (1:1, v/v)	0.01-3V at 35mA/g	~2250	~1900	84.4	Decreasing / 20 cycles	17 ⁴⁶
Ball milling	Particles	20	-	-	1M LiPF ₆ in EC/DEC/E MC (1:1:1, v/v)	0.01-1.5V at 0.15 mA/cm ²	~500	~350	70	Decreasing / 40 cycles	18 ⁴⁷
LPCVD	Particles	~10.7	-	-	1M LiPF ₆ in EC/DEC	-	-	-	-	Decreasing / 11 cycles	19 ⁴⁸
Milling + thermal process	Particles	24.4	-	-	1M LiPF ₆ in EC/DEC (1:2, v/v)	0.02-1.2V at 160mA/g	-	~833	-	Stable / 30 cycles	20 ⁴⁹
Silicon precursor decomposition	Particles	9.2	6-12	1.4-1.6	1M LiPF ₆ in EC/DMC (1:1, v/v)	0.01-1.5V at 30mA/g	705	590	83.7	Decreasing / 11 cycles	21 ⁵⁰

Ball milling	Particles	30.1	2.25	-	1.3M LiPF ₆ in EC/DEC (3:7, v/v)	0.001-1.5V at 100mA/g	~1420	~1000	70.4	Decreasing / 30 cycles	22 ⁵¹
Ball milling	Particles (alloy)	-	-	-	1M LiPF ₆ in EC/DMC	0.02-1.2V at 250μA/cm ²	1693	704	41.6	Slightly decreasing / 30 cycles	23 ⁵²
Coating + thermal process	Particles	10	12.7	-	1M LiPF ₆ in DEC/EC/D MC (1:1:1, v/v)	0.01-2.0V at 0.2mA/cm ²	890	567	63.7	Stable / 20 cycles	24 ⁵³
Ball milling	Particles (alloy)	-	-	-	1M LiPF ₆ in EC/DEC/E MC (1:1:1, v/v)	0.01-1.5 at 0.15mA/cm ²	646.2	420	65	Slightly decreasing / 40 cycles	25 ⁵⁴
Ball milling	Particles	9	-	-	1M LiPF ₆ in EC/DMC (1:1, w/w)	0.005-3V at 1/30C	718	533	74	Decreasing / 10 cycles	26 ⁵⁵
Mixing with specific binder	Particles	20	-	-	1M LiPF ₆ in EC/DEC (3:7,v/v)	0.024-1.5V at 0.1, 0.2 and 0.5C	-	-	-	Decreasing / 50 cycles	27 ⁵⁶
Mixing + thermal process	Particles	10	-	-	1M LiPF ₆ in EC/DMC/E MC (1:1:1, v/v)	0.005-1V 0.25mA/cm ²	750	660	88	Stable / 14 cycles	28 ⁵⁷

Mixing + thermal process	Particles	20	-	-	1M LiPF ₆ in EC/DEC (1:1, v/v)	0.02-1.5V with CC-CV	814	700	86	Stable / 50 cycles	29 ⁵⁸
Milling + thermal process	Particles	29.1	-	-	0.13M LiBOB + 0.84M LiPF ₆ in EC/DMC/E MC (1:1:1, v/v) + 2wt% VC	0.02-1.5V at 50mA/g and 168mA/g	850	640	75.3	Variation, decreasing / 200 cycles	30 ⁵⁹
Chemical synthesis	Particles	15.5	-	-	1M LiPF ₆ in EC/DEC (1:1, w/w)	0.01-1V at 25mA/g	1503	1056	70.2	Decreasing / 50 cycles	31 ¹⁹
Mechanical milling + pyrolysis	Particles (alloy)	-	-	-	1M LiPF ₆ in EC/DMC (1:1, w/w)	0.02-1.5V at 0.1mA/cm ²	1450.3	956.4	66	Decreasing / 50 cycles	32 ⁶⁰
Milling	Particles	-	-	-	1.3M LiPF ₆ in EC/DEC/FE C (2:6:2, v/v)	0.001-1.5V at 100mA/g	~1500	~1100	73.3	Decreasing / 50cycles	33 ⁶¹
Milling	Particles	~20	7	1	1M LiPF ₆ in EC/EMC	0.008-1.5V with CC-CV	657	568	86.4	Decreasing / 30 cycles	34 ¹⁷

					(1:2, v/v) + 1wt% VC						
Mixing	Nanowires	15	-	-	1M LiPF ₆ in EC/DMC (1:1, v/v)	0.01-1.5V at 0.1mA/cm ²	~811	~610	75.2	Decreasing / 15 cycles	35 ²⁸
Thermal process	Particles	33	-	-	1M LiPF ₆ in EC/DEC (3:7, v/v) + 2wt% VC	0.005-1.5V at 0.5C	-	-	-	Stable / 100 cycles	36 ⁶²
Mixing with specific binder	Particles	20	-	-	1 or 0.5M Li-TFSA in BMP-TFSA	0-2V at 50 mA/g	~1250	~750	60	Decreasing / 50 cycles	37 ⁶³
Milling + thermal process	Particles	60	-	1.4	1.12 LiPF ₆ in EC/EMC (1:1, v/v) + 2wt% VC	0.005-1.5V at 0.2C	761	655	92	Slightly decreasing / 300 cycles	38 ⁶⁴
Milling	Particles	40	-	-	1M LiPF ₆ in EC/DMC (1:2, v/v) + 10wt% FEC	0-1.5V at 0.63A/g	868.8	714.4	82.3	Decreasing / 200 cycles	39 ²⁹
Milling	Particles	30	0.30	-	1M LiPF ₆ in EC/DMC (1:1, v/v) + 2vol% FEC	0-2V with CC- CV mode	~2000	~1300	65	Stable / 140 cycles	40 ⁶⁵

Spray + pyrolysis	Particles	22	-	-	1M LiPF ₆ in EC/EMC/D MC (1:1:1, v/v)	0.02-1.5V with CC-CV mode	864.6	602.7	69.7	Stable / 20 cycles	41 ⁶⁶
Thermal process	Particles	22	-	-	1M LiPF ₆ in EC/DMC (1:1, v/v)	0.01-2V at 50 mA/g	690	520	75.3	Stable / 20 cycles	42 ⁶⁷

References

1. Park, O. K.; Cho, Y.; Lee, S.; Yoo, H.-C.; Song, H.-K.; Cho, J., Who will drive electric vehicles, olivine or spinel? *Energy Environ. Sci.* **2011**, *4* (5), 1621-1633.
2. Choi, N.-S.; Chen, Z.; Freunberger, S. A.; Ji, X.; Sun, Y.-K.; Amine, K.; Yushin, G.; Nazar, L. F.; Cho, J.; Bruce, P. G., Challenges Facing Lithium Batteries and Electrical Double-Layer Capacitors. *Angew. Chem. Int. Ed.* **2012**, *51* (40), 9994-10024.
3. Note: Energy density (E) = $V \times It$ (Wh/kg), where V = the cell operating voltage (V), and It = the electrochemical capacity (Ah/kg) of the cell.
4. Goodenough, J. B.; Kim, Y., Challenges for Rechargeable Li Batteries. *Chem. Mater.* **2009**, *22* (3), 587-603.
5. Lee, K. T.; Jeong, S.; Cho, J., Roles of Surface Chemistry on Safety and Electrochemistry in Lithium Ion Batteries. *Acc. Chem. Res.* **2013**, *46*.
6. Liu, X. H.; Zhang, L. Q.; Zhong, L.; Liu, Y.; Zheng, H.; Wang, J. W.; Cho, J. H.; Dayeh, S. A.; Picraux, S. T.; Sullivan, J. P.; Mao, S. X.; Ye, Z. Z.; Huang, J. Y., Ultrafast Electrochemical Lithiation of Individual Si Nanowire Anodes. *Nano Lett.* **2011**, *11* (6), 2251-2258.
7. Liu, X. H.; Zheng, H.; Zhong, L.; Huan, S.; Karki, K.; Zhang, L. Q.; Liu, Y.; Kushima, A.; Liang, W. T.; Wang, J. W.; Cho, J. H.; Epstein, E.; Dayeh, S. A.; Picraux, S. T.; Zhu, T.; Li, J.; Sullivan, J. P.; Cumings, J.; Wang, C. S.; Mao, S. X.; Ye, Z. Z.; Zhang, S. L.; Huang, J. Y., Anisotropic Swelling and Fracture of Silicon Nanowires during Lithiation. *Nano Lett.* **2011**, *11* (8), 3312-3318.
8. Liu, X. H.; Zhong, L.; Huang, S.; Mao, S. X.; Zhu, T.; Huang, J. Y., Size-Dependent Fracture of Silicon Nanoparticles During Lithiation. *Acs Nano* **2012**.
9. Kim, H.; Seo, M.; Park, M. H.; Cho, J., A Critical Size of Silicon Nano-Anodes for Lithium Rechargeable Batteries. *Angew. Chem. Int. Ed.* **2010**, *49* (12), 2146-2149.
10. Liu, N.; Wu, H.; McDowell, M. T.; Yao, Y.; Wang, C.; Cui, Y., A Yolk-Shell Design for Stabilized and Scalable Li-Ion Battery Alloy Anodes. *Nano Lett.* **2012**.
11. Jeong, H. M.; Lee, S. Y.; Shin, W. H.; Kwon, J. H.; Shakoor, A.; Hwang, T. H.; Kim, S. Y.; Kong, B.-S.; Seo, J.-S.; Lee, Y. M.; Kang, J. K.; Choi, J. W., Silicon@porous nitrogen-doped carbon spheres through a bottom-up approach are highly robust lithium-ion battery anodes. *RSC Adv.* **2012**, *2* (10), 4311-4317.
12. Chan, C. K.; Peng, H. L.; Liu, G.; McIlwrath, K.; Zhang, X. F.; Huggins, R. A.; Cui, Y., High-performance lithium battery anodes using silicon nanowires. *Nat. Nanotechnol.* **2008**, *3* (1), 31-35.
13. Cui, L. F.; Yang, Y.; Hsu, C. M.; Cui, Y., Carbon-Silicon Core-Shell Nanowires as High Capacity Electrode for Lithium Ion Batteries. *Nano Lett.* **2009**, *9* (9), 3370-3374.

14. Park, M. H.; Kim, M. G.; Joo, J.; Kim, K.; Kim, J.; Ahn, S.; Cui, Y.; Cho, J., Silicon Nanotube Battery Anodes. *Nano Lett.* **2009**, *9* (11), 3844-3847.
15. Kim, H.; Han, B.; Choo, J.; Cho, J., Three-Dimensional Porous Silicon Particles for Use in High-Performance Lithium Secondary Batteries. *Angew. Chem. Int. Ed.* **2008**, *47* (52), 10151-10154.
16. Magasinski, A.; Dixon, P.; Hertzberg, B.; Kvit, A.; Ayala, J.; Yushin, G., High-performance lithium-ion anodes using a hierarchical bottom-up approach. *Nat. Mater.* **2010**, *9* (4), 353-358.
17. Jo, Y. N.; Kim, Y.; Kim, J. S.; Song, J. H.; Kim, K. J.; Kwag, C. Y.; Lee, D. J.; Park, C. W.; Kim, Y. J., Si-graphite composites as anode materials for lithium secondary batteries. *J. Power Sources* **2010**, *195* (18), 6031-6036.
18. Kasavajjula, U.; Wang, C.; Appleby, A. J., Nano- and bulk-silicon-based insertion anodes for lithium-ion secondary cells. *J. Power Sources* **2007**, *163* (2), 1003-1039.
19. Martin, C.; Alias, M.; Christien, F.; Crosnier, O.; Bélanger, D.; Brousse, T., Graphite-Grafted Silicon Nanocomposite as a Negative Electrode for Lithium-Ion Batteries. *Adv. Mater.* **2009**, *21* (46), 4735-4741.
20. Lu, J. Q.; Yi, S. S., Uniformly sized gold nanoparticles derived from PS-b-P2VP block copolymer templates for the controllable synthesis of Si nanowires. *Langmuir* **2006**, *22* (9), 3951-3954.
21. Campos, L. C.; Manfrinato, V. R.; Sanchez-Yamagishi, J. D.; Kong, J.; Jarillo-Herrero, P., Anisotropic Etching and Nanoribbon Formation in Single-Layer Graphene. *Nano Lett.* **2009**, *9* (7), 2600-2604.
22. Walter van Schalkwijk, B. S., *Advances in Lithium-Ion Batteries*. Kluwer academic publishers: New York, Boston, Dordrecht, London, Moscow, **2002**.
23. ASM International Alloy Phase Diagram and the Handbook Committees. *ASM Handbook – Alloy Phase Diagrams*, Vol. 3; ASM International: Novelty, OH, **1992**; p. 1233
24. Yoshio, M.; Wang, H.; Fukuda, K., Spherical Carbon-Coated Natural Graphite as a Lithium-Ion Battery-Anode Material. *Angew. Chem. Int. Ed.* **2003**, *42* (35), 4203-4206.
25. Ferrari, A. C.; Robertson, J., Interpretation of Raman spectra of disordered and amorphous carbon. *Phys. Rev. B* **2000**, *61* (20), 14095-14107.
26. Liu, H.; Hamers, R. J., An X-ray photoelectron spectroscopy study of the bonding of unsaturated organic molecules to the Si(001) surface. *Surf. Sci.* **1998**, *416* (3), 354-362.
27. Deng, J.; Ji, H.; Yan, C.; Zhang, J.; Si, W.; Baunack, S.; Oswald, S.; Mei, Y.; Schmidt, O. G., Naturally Rolled-Up C/Si/C Trilayer Nanomembranes as Stable Anodes for Lithium-Ion Batteries with Remarkable Cycling Performance. *Angew. Chem. Int. Ed.* **2013**, *52* (8), 2326-2330.
28. Xu, W. L.; Flake, J. C., Composite Silicon Nanowire Anodes for Secondary Lithium-Ion Cells. *J. Electrochem. Soc.* **2010**, *157* (1), A41-A45.

29. Chen, X.; Li, X.; Ding, F.; Xu, W.; Xiao, J.; Cao, Y.; Meduri, P.; Liu, J.; Graff, G. L.; Zhang, J.-G., Conductive Rigid Skeleton Supported Silicon as High-Performance Li-Ion Battery Anodes. *Nano Lett.* **2012**.
30. Ng, S. B.; Lee, J. Y.; Liu, Z. L., Si-O network encapsulated graphite-silicon mixtures as negative electrodes for lithium-ion batteries. *J. Power Sources* **2001**, *94* (1), 63-67.
31. Niu, J. J.; Lee, J. Y., Improvement of usable capacity and cyclability of silicon-based anode materials for lithium batteries by sol-gel graphite matrix. *Electrochem. Solid State Lett.* **2002**, *5* (6), A107-A110.
32. Lee, H. Y.; Lee, S. M., Carbon-coated nano-Si dispersed oxides/graphite composites as anode material for lithium ion batteries. *Electrochem. Commun.* **2004**, *6* (5), 465-469.
33. Liu, Y.; Hanai, K.; Matsumura, T.; Imanishi, N.; Hirano, A.; Takeda, Y., Novel Composites Based on Ultrafine Silicon, Carbonaceous Matrix, and the Introduced Co-Milling Components as Anode Host Materials for Li-Ion Batteries. *Electrochem. Solid-State Lett.* **2004**, *7* (12), A492-A495.
34. Wang, G. X.; Yao, J.; Liu, H. K., Characterization of nanocrystalline Si-MCMB composite anode materials. *Electrochem. Solid State Lett.* **2004**, *7* (8), A250-A253.
35. Xie, J.; Cao, G. S.; Zhao, X. B., Electrochemical performances of Si-coated MCMB as anode material in lithium-ion cells. *Mater. Chem. Phys.* **2004**, *88* (2-3), 295-299.
36. Holzapfel, M.; Buqa, H.; Krumeich, F.; Novak, P.; Petrat, F. M.; Veit, C., Chemical vapor deposited silicon/graphite compound material as negative electrode for lithium-ion batteries. *Electrochem. Solid State Lett.* **2005**, *8* (10), A516-A520.
37. Park, M. S.; Lee, Y. J.; Rajendran, S.; Song, M. S.; Kim, H. S.; Lee, J. Y., Electrochemical properties of Si/Ni alloy-graphite composite as an anode material for Li-ion batteries. *Electrochim. Acta* **2005**, *50* (28), 5561-5567.
38. Yoshio, M.; Tsumura, T.; Dimov, N., Electrochemical behaviors of silicon based anode material. *J. Power Sources* **2005**, *146* (1-2), 10-14.
39. Chen, L. B.; Xie, X. H.; Xie, J. Y.; Wang, K.; Yang, J., Binder effect on cycling performance of silicon/carbon composite anodes for lithium ion batteries. *J. Appl. Electrochem.* **2006**, *36* (10), 1099-1104.
40. Jeon, B. J.; Kang, S. W.; Lee, J. K., Electrochemical characteristics of silicon coated graphite prepared by gas suspension spray method for anode material of lithium secondary batteries. *Korean J. Chem. Eng.* **2006**, *23* (5), 854-859.
41. Kim, I. C.; Byun, D.; Lee, J. K., Electrochemical characteristics of silicon-metals coated graphites for anode materials of lithium secondary batteries. *J. Electroceram.* **2006**, *17* (2-4), 661-665.
42. Park, M. S.; Rajendran, S.; Kang, Y. M.; Han, K. S.; Han, Y. S.; Lee, J. Y., Si-Ni alloy-graphite composite synthesized by arc-melting and high-energy mechanical milling for use as an anode in lithium-ion batteries. *J. Power Sources* **2006**, *158* (1), 650-653.

43. Uono, H.; Kim, B. C.; Fuse, T.; Ue, M.; Yamaki, J. I., Optimized structure of silicon/carbon/graphite composites as an anode material for Li-ion batteries. *J. Electrochem. Soc.* **2006**, *153* (9), A1708-A1713.
44. Yang, X. L.; Wen, Z. Y.; Xu, X. X.; Lin, B.; Lin, Z. X., High-performance silicon/carbon/graphite composites as anode materials for lithium ion batteries. *J. Electrochem. Soc.* **2006**, *153* (7), A1341-A1344.
45. Yoshio, M.; Tsumura, T.; Dimov, N., Silicon/graphite composites as an anode material for lithium ion batteries. *J. Power Sources* **2006**, *163* (1), 215-218.
46. Zhang, Y.; Zhang, X. G.; Zhang, H. L.; Zhao, Z. G.; Li, F.; Liu, C.; Cheng, H. M., Composite anode material of silicon/graphite/carbon nanotubes for Li-ion batteries. *Electrochim. Acta* **2006**, *51* (23), 4994-5000.
47. Zuo, P.; Yin, G.; Tong, Y., SiMn-graphite composites as anodes for lithium ion batteries. *Solid State Ionics* **2006**, *177* (37-38), 3297-3301.
48. Alias, M.; Crosnier, O.; Sandu, I.; Jestin, G.; Papadimopoulos, A.; Le Cras, F.; Schleich, D. M.; Brousse, T., Silicon/graphite nanocomposite electrodes prepared by low pressure chemical vapor deposition. *J. Power Sources* **2007**, *174* (2), 900-904.
49. Datta, M. K.; Kumta, P. N., Silicon, graphite and resin based hard carbon nanocomposite anodes for lithium ion batteries. *J. Power Sources* **2007**, *165* (1), 368-378.
50. Khomenko, V. G.; Barsukov, V. Z.; Doninger, J. E.; Barsukov, I. V., Lithium-ion batteries based on carbon-silicon-graphite composite anodes. *J. Power Sources* **2007**, *165* (2), 598-608.
51. Kim, H.; Im, D.; Doo, S. G., Electrochemical properties of Ni-based inert phases incorporated Si/graphite composite anode. *J. Power Sources* **2007**, *174* (2), 588-591.
52. Rock, N. L.; Kumta, P. N., Synthesis and characterization of electrochemically active graphite-silicon-tin composite anodes for Li-ion applications. *J. Power Sources* **2007**, *164* (2), 829-838.
53. Zhang, T.; Gao, J.; Fu, L. J.; Yang, L. C.; Wu, Y. P.; Wu, H. Q., Natural graphite coated by Si nanoparticles as anode materials for lithium ion batteries. *J. Mater. Chem.* **2007**, *17* (13), 1321-1325.
54. Zuo, P. J.; Yin, G. P.; Hao, X. F.; Yang, Z. L.; Ma, Y. L.; Gao, Z. G., Synthesis and electrochemical performance of Si/Cu and Si/Cu/graphite composite anode. *Mater. Chem. Phys.* **2007**, *104* (2-3), 444-447.
55. Cahen, S.; Janot, R.; Laffont-Dantras, L.; Tarascon, J. M., Chemical reduction of SiCl₄ for the preparation of silicon-graphite composites used as negative electrodes in lithium-ion batteries. *J. Electrochem. Soc.* **2008**, *155* (7), A512-A519.
56. Hochgatterer, N. S.; Schweiger, M. R.; Koller, S.; Raimann, P. R.; Wohrle, T.; Wurm, C.; Winter, M., Silicon/graphite composite electrodes for high-capacity anodes: Influence of binder chemistry on cycling stability. *Electrochem. Solid State Lett.* **2008**, *11* (5), A76-A80.

57. Kim, H. S.; Chung, K. Y.; Cho, L. W., Effect of Carbon-coated Silicon/Graphite Composite Anode on the Electrochemical Properties. *Bull. Korean Chem. Soc.* **2008**, *29* (10), 1965-1968.
58. Lee, J. H.; Kim, W. J.; Kim, J. Y.; Lim, S. H.; Lee, S. M., Spherical silicon/graphite/carbon composites as anode material for lithium-ion batteries. *J. Power Sources* **2008**, *176* (1), 353-358.
59. Li, M. Q.; Qu, M. Z.; He, X. Y.; Yu, Z. L., Electrochemical Performance of Si/Graphite/Carbon Composite Electrode in Mixed Electrolytes Containing LiBOB and LiPF₆. *J. Electrochem. Soc.* **2009**, *156* (4), A294-A298.
60. Wang, X.; Wen, Z.; Liu, Y.; Xu, X.; Lin, J., Preparation and characterization of a new nanosized silicon–nickel–graphite composite as anode material for lithium ion batteries. *J. Power Sources* **2009**, *189* (1), 121-126.
61. Hwang, S. S.; Cho, C. G.; Kim, H., Polymer microsphere embedded Si/graphite composite anode material for lithium rechargeable battery. *Electrochim. Acta* **2010**, *55* (9), 3236-3239.
62. Fuchsbichler, B.; Stangl, C.; Kren, H.; Uhlig, F.; Koller, S., High capacity graphite-silicon composite anode material for lithium-ion batteries. *J. Power Sources* **2011**, *196* (5), 2889-2892.
63. Yabuuchi, N.; Shimomura, K.; Shimbe, Y.; Ozeki, T.; Son, J.-Y.; Oji, H.; Katayama, Y.; Miura, T.; Komaba, S., Graphite-Silicon-Polyacrylate Negative Electrodes in Ionic Liquid Electrolyte for Safer Rechargeable Li-Ion Batteries. *Adv. Energy Mater.* **2011**, *1* (5), 759-765.
64. Yoon, Y. S.; Jee, S. H.; Lee, S. H.; Nam, S. C., Nano Si-coated graphite composite anode synthesized by semi-mass production ball milling for lithium secondary batteries. *Surf. Coat. Technol.* **2011**, *206* (2–3), 553-558.
65. Han, Z. J.; Yabuuchi, N.; Shimomura, K.; Murase, M.; Yui, H.; Komaba, S., High-capacity Si-graphite composite electrodes with a self-formed porous structure by a partially neutralized polyacrylate for Li-ion batteries. *Energy Environ. Sci.* **2012**, *5* (10), 9014-9020.
66. Lai, J.; Guo, H. J.; Wang, Z. X.; Li, X. H.; Zhang, X. P.; Wu, F. X.; Yue, P., Preparation and characterization of flake graphite/silicon/carbon spherical composite as anode materials for lithium-ion batteries. *J. Alloys Compd.* **2012**, *530*, 30-35.
67. Yu, J.; Zhan, H. H.; Wang, Y. H.; Zhang, Z. L. I.; Chen, H.; Li, H.; Zhong, Z. Y.; Su, F. B., Graphite microspheres decorated with Si particles derived from waste solid of organosilane industry as high capacity anodes for Li-ion batteries. *J. Power Sources* **2013**, *228*, 112-119.

* Chapter IV is reproduced in with a permission of “Jeong, S.; Lee, J.-P.; Ko, M.; Kim, G.; Park, S.; Cho, J., Etched Graphite with Internally Grown Si Nanowires from Pores as an Anode for High Density Li-Ion Batteries. *Nano Letters* 2013, *13* (7), 3403-3407”. Copyright **2013** American Chemical Society.

Chapter V

3D Amorphous Silicon on Nanopillar Copper Electrodes as Anodes for High-Rate Lithium-Ion Batteries

1. Introduction

Owing to the recent development of electronic devices such as personal computers and smart phones, wearable devices have become remarkably attractive as the next generation of smart devices, heralding a paradigm shift in trends from portable to wearable devices. Because wearable devices need to be more compact and lightweight, and need to retain the high performance of portable ones, Li-ion batteries play a key role in this paradigm shift. Thin-film batteries are the most suited for this application, and provide a major breakthrough in the size reduction of wearable devices while maintaining high energy density.¹⁻⁵ However, the use of carbon-based materials in a conventional system do not meet the demands owing to their low theoretical capacity (372 mAh/g).⁶

Among the various potential anode materials, Si has been intensively investigated because it imparts a high theoretical capacity to the electrodes (4200 mAh/g), which is over 10 times higher than that of graphite.⁷ Despite these superior characteristics, Si undergoes a 400% change in volume during lithiation, which results in pulverization and degradation of the electrical connection between electrodes.⁸⁻¹¹ This disadvantage is the main factor in the significant capacity loss in the system during the electrochemical reaction (i.e., $\text{Si} + x \text{Li}^+ + x \text{e}^- \leftrightarrow \text{Li}_x\text{Si}$).¹² To prevent this crack formation caused by the stress in Si during cycling, two basic principles are applied in nano-engineering of Si-based electrodes to reduce the strain as follows:¹³⁻²³ i) Empty space is incorporated into the electrode for effective accommodation of strain during cycling. There have been reports that Si nanowires,¹³ Si nanotubes²⁰ and Si nanoparticles encapsulated in hollow carbon tubes²⁴ are used for nano-engineered active materials²⁵⁻²⁹; and ii) Si thin film that is thinner than the critical thickness is deposited on the planar surface of the current collector using various deposition processes to prevent the loss of electrical connectivity between the active materials and current collector.³⁰⁻³² With respect to the two approaches, three-dimensional (3D) nanostructured electrodes have been widely considered because they significantly improve Li-ion diffusion and electron transport to overcome the low energy per unit area limitation of planar electrodes.³³⁻³⁶

Accordingly, we demonstrate a 3D nanostructured thin-film electrode consisting of Cu nanopillars fabricated using roll-to-roll hot embossing followed by Cu electroforming with the *a*-Si thin layer coated on Cu nanopillars via low-pressure chemical vapor deposition (LPCVD). As a current collector, Cu nanopillars substrate provide a high surface area for better mass accommodation of Si deposition

while the space between Cu nanopillars enhance the electrochemical reaction between the electrode and electrolyte and accommodates the volume change during cycling. In addition, because the fabrication of the Cu nanopillar substrate only involves conventional top-down processes, the nanopillars can be generated through a facile and fast process with control of the surface area and simple modulation of the nanopillar density or diameter. Remarkably, the well-patterned nanopillar substrate imparts a significantly enhanced connection between the current collector and active materials without a binder, and also provides free space to accommodate Si expansion without pulverization during cycling.

2. Experimental section

2.1. Fabrication of *a*-Si/3D-Cu electrode

The pitches and heights of the Ni metal plate stamps were 1 and 2 μm , respectively, and the diameters of the pillars were either 250 or 500 nm. The nanoscale surface protrusion pattern of a rolled Ni metal plate stamp was transferred to polyvinyl chloride (PVC) by thermal roll-to-roll processing (order production, CMP Co., Ltd.) at 100 $^{\circ}\text{C}$ under ~ 10 atm of pressure. Cu metal was then deposited over the embossed PVC film using e-beam evaporation at 60 $^{\circ}\text{C}$ and 2.7×10^{-5} atm with the rate of 3 $\text{\AA}/\text{s}$ to form a seed layer by 100 nm for the electroforming process. (EBX-1000, ULVAC Inc.) Electroformation at 0.02 A for 1 h in a Cu plating solution ($\text{CuSO}_4 \cdot 5\text{H}_2\text{O}/\text{H}_2\text{SO}_4 = 2.5:1$ with 70 ppm HCl; Americhem, Inc.) filled the cavities with Cu and formed the Cu film. Then, the Cu foil with an array of Cu nanopillars was detached from the polymer film and covered with an amorphous Si layer using LPCVD with 2% SiH_4 at 200 $^{\circ}\text{C}$ and 0.839 atm under 50 W of RF power (SJF-1000T2, Sungjin Semitech Co., Ltd.).

2.2. Fabrication of the Li-ion half-cell

A coin-shaped half-cell (2032R) was fabricated with an *a*-Si/3D-Cu working electrode (The blanket film contains 0.136 mg of Si corresponding to $0.088 \text{ mg}/\text{cm}^2$, while the *a*-Si/3D-Cu electrodes with 250 and 500 nm diameter nanopillars contain 0.142 and 0.129 mg of Si corresponding to 0.092 and $0.084 \text{ mg}/\text{cm}^2$, respectively.) and metallic Li reference electrode. The working and reference electrode were punched for the 2032R half-cell with diameters of 14 mm and separated with polypropylene separator. The electrolyte (Panax Korea) was 1.3 M LiPF_6 in a blend of ethylene carbonate (EC) and ethyl methyl carbonate (EMC) with 10 wt% fluoroethylene carbonate (FEC) additive.

2.3. Electrochemical characterization of the half-cell

For the electrochemical characterizations, the blanket film and *a*-Si/3D-Cu electrodes with 250 and 500 nm diameter nanopillars were cycled between 0.005 and 1.5 V in Li half-cells (2032R, 1 C = 2000 mA/g, Wonatech Co., Ltd.) at 24 °C.

2.4. Morphology characterization of the *a*-Si/3D-Cu nanopillar electrode

The electrode configuration of the blanket film and *a*-Si/3D-Cu electrodes with 250 and 500 nm diameter nanopillars were characterized by high-resolution transmission electron microscopy (HR-TEM, JEM-2100F, JEOL Inc.), energy-dispersive spectroscopy (EDS, JEM-2100, JEOL Inc.) elemental mapping, and field emission (FE)-SEM (EX-200, Horiba Inc.). The TEM sample was fabricated using a focused-ion-beam instrument (FIB; Quanta 3D FEG, FEI Inc.). The presence of *a*-Si was confirmed via fast Fourier transform (FFT; JEM-2100, JEOL Inc.) analysis and the crystallization of Cu was confirmed by X-ray diffraction (XRD; Rigaku) analysis.

3. Results and discussion

Figure 1 shows a schematic of the fabrication of the electrode comprising amorphous Si deposited on a 3D Cu nanopillar substrate (*a*-Si/3D-Cu nanopillar electrode). First, Ni metal plate stamps with pitches of 1 μm, heights of 2 μm, and diameters of either 250 or 500 nm were fabricated. In the fabrication process of Ni stamp, the height of 2 μm was optimized dimensions to reproduce the desired pattern by thermal roll to roll method. If the aspect ratio of the pillar is too high (> 9) in our experimental condition, the Ni pillars were deformed during contact to the PVC film, as shown in **Figure S1**. Then, the prepared patterned Ni stamp was transferred to polyvinyl chloride (PVC, glass transition temperature = 80 °C) at 100 °C and ~10 atm to prepare the patterned mold (**Figure 1a**). The Cu nanopillar substrate was formed by deposition of Cu onto the embossed PVC mold by e-beam evaporation at 60 °C and 2.7×10^{-5} atm to form a seed layer by 100 nm followed by electroformation at 0.02 A for 1 h in a Cu plating solution ($\text{CuSO}_4 \cdot 5\text{H}_2\text{O}/\text{H}_2\text{SO}_4 = 2.5:1$ with 70 ppm HCl) (**Figure 1b**). Finally, the well-arrayed Cu nanopillar substrate (**Figure S2**) was detached from the polymer mold and amorphous Si was deposited onto the prepared substrate by LPCVD using 2% SiH_4 at 200 °C and 0.839 atm with an RF power of 50 W (**Figure 1c**).

For comparison, the electrode configuration of a blanket film and *a*-Si/3D-Cu electrodes with 250 and 500 nm diameter nanopillars were characterized by transmission electron microscopy (TEM) and energy-dispersive X-ray (EDX) elemental mapping (**Figure 2**). The structures of the *a*-Si/3D-Cu nanopillar electrodes show clearly well-developed periodic patterns consistent with the schematic in

Figure 1, as shown in **Figures 2a, b, and c**. Each electrode contains small pores, which were expanded during sample preparation by a focused-ion-beam treatment, at the interface between the Cu formed by e-beam evaporation and electroforming process, describing as white spots in TEM results. In **Figures 2d, e, and f**, the thickness of the *a*-Si deposition layer was fixed at 200 nm for the blanket film and 130 nm for both *a*-Si/3D-Cu nanopillar electrodes, and the amorphous Si structure was confirmed via fast Fourier transform (FFT) analysis. The thickness difference caused by *a*-Si deposition via LPCVD is not relevant in this work, especially for the electrochemical test. From the energy dispersive X-ray (EDX) elemental mapping images shown in **Figure 2g, h, and i**, it was confirmed that the electrode structures spatially correspond to *a*-Si and Cu and the likelihood of producing Cu silicide during processing and X-ray diffraction (XRD) analysis is low (**Figure S3**).³⁷

For electrochemical characterization, the blanket film and *a*-Si/3D-Cu nanopillar electrodes with 250 and 500 nm diameters were cycled at 0.5 C rate between 0.005 and 1.5 V in Li half-cells (2032R, 1 C = 2000 mA/g). The first cycle voltage profiles of each electrode are shown in **Figure 3a**; all electrodes exhibit no plateau below 0.1 V after lithiation, which is the typical *a*-Si electrochemical behavior. The discharge capacities of the blanket film and *a*-Si/3D-Cu electrodes with 250 and 500 nm diameter nanopillars during the first cycle are 1947, 1982, and 1847 mAh/g with coulomb efficiencies (C.E.) of 92.2, 95.3, and 91.3 %, respectively.

Figure 3b exhibits the cycle retention of each electrode at 0.5 C rate. After 100 cycles, the *a*-Si/3D-Cu electrodes with 250 and 500 nm diameter nanopillars show 1627 and 1420 mAh/g of the discharge capacity, respectively; On the contrary, the blanket film shows 138 mAh/g of the discharge capacity with 7.1% of retention. The main reason for the better cycle retention of the *a*-Si/3D-Cu nanopillar electrodes is the morphology variation in each electrode before and after 100 cycles. As shown in **Figures 4a and d**, after 100 cycles, the blanket film electrode shows a high concentration of cracks and delamination, which is related to the strain caused by the significant mechanical stress due to the *a*-Si volume change, resulting in a loss of electrical connectivity. In contrast, both *a*-Si/3D-Cu nanopillar electrodes exhibited smooth surfaces even after 100 cycles (**Figures 4b, c, e, and f**). From **Figure S4**, it becomes evident that the adhesion between *a*-Si and Cu layer is still strong after 100th charge and discharge cycles.

These results indicate that not only do *a*-Si 3D-nanopillar electrodes have sufficient void space to accommodate volume changes during the electrochemical reaction, but the well-patterned nanopillar substrate also allows significant enhancement of the connection between the current collector and active materials without binder. The high performance of the electrodes was confirmed by dQ/dV analysis, as shown in **Figure S5**. The differential plot of the first cycle exhibits two peaks at 0.08 and 0.23 V for lithiation and 0.3 and 0.48 V for de-lithiation.³⁸ The reversibility was maintained without additional polarization even after 100 cycles. The retention results indicate that the electrode with a 500 nm

diameter nanopillar array exhibited poorer performance than the electrode with a 250 nm diameter nanopillar array, because the free space between the nanopillars was insufficient to completely accommodate the expansion of Si resulting in the slight deformation of the nanopillar array, as shown in the inset of **Figure 4f**. Also, the improved 1st C.E. and cycle retention of 250 nm diameter sample compared to 500 nm one are related to the nanopillar's resistance after volume expansion of *a*-Si. It is reported that the resistance is increased as copper strain is developed after deformation.³⁹ Therefore, more deformed 500 nm sample may be expected to build up a resistance, resulting in a decrease of electron transport for charger-transfer reaction. In addition, the structural discontinuity of the deposited film plays a key role of improving the electrochemical performance of *a*-Si/3D-Cu nanopillar electrode. Not only the discontinuity of electrode can provide the more interface region between active materials and electrolyte, but also the region where crack yields could buffer to some degree of volume expansion (**Figure. S6**).

Figure 3c demonstrates the improved rate capability of both *a*-Si/3D-Cu nanopillar electrodes from 0.5 to 20 C, and improved cycle stability, even after the rate test at 20 C rate, compared to those of the blanket film electrode under the same charge and discharge conditions (1 C = 2000 mA/g). The voltage profiles for each electrode are shown in **Figure S7**. The *a*-Si/3D-Cu electrode with 250 nm diameter nanopillars exhibits the discharge capacities of 2466, 1474, 1122, and 587 mAh/g at rates of 0.5, 3, 7, and 20 C, respectively, with a capacity retention of 23.8% at 20 C; in comparison, the blanket film electrode has a capacity retention of ~0% under the same conditions. Remarkably, after the same rate test, both *a*-Si/3D-Cu nanopillar with 250 and 500 nm diameter electrodes underwent little capacity fading after 300 cycles at 20 C rate, showing 996 and 719 mAh/g of the discharging capacities with 99.3 (± 0.3) and 99.9 (± 0.3) % of the C.E., respectively. This result is comparable to that of an electrode that is surface-treated with carbon or Al₂O₃.⁴⁰ The capacity increase at the beginning condition in the range of from 3 C to 20 C may be related to the activation of unreacted inside region in silicon, which is generally known to Si electrodes operated at high C-rate condition.⁴¹⁻⁴³ The maintenance of the morphology of the *a*-Si/3D-Cu nanopillar electrodes after cycling (**Figure S8**) is the likely cause of the excellent cycling stability and rate performance.

4. Conclusion

In conclusion, based on these results, nano-pattern technology can play a key role in enhancing the performance of various types of active materials because of the low internal resistance caused by enhanced attachment between the patterned current collector and active materials, facile charge transport due to the three-dimensional configuration, and stress relaxation as a result of the voids between the nanopillars.

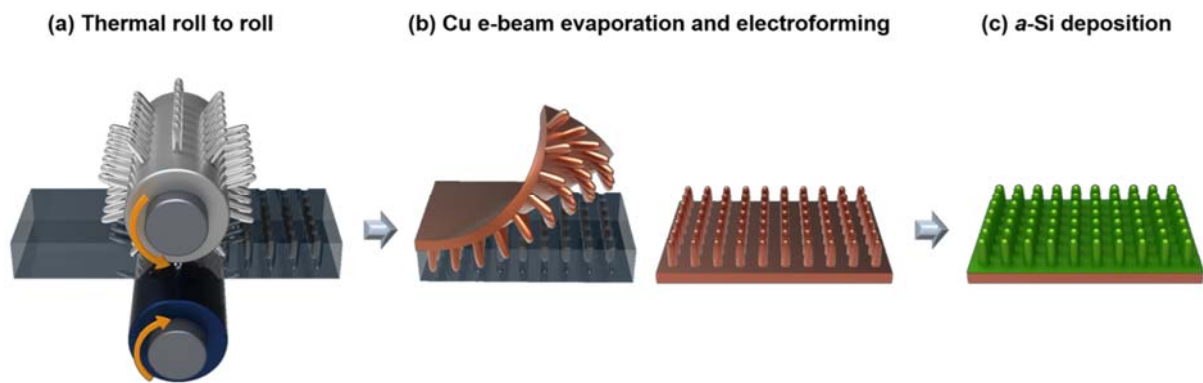


Figure 1. Schematic of the fabrication of 3D amorphous on Si nanopillar Cu electrode. (a) Patterned polyvinyl chloride (PVC) obtained from thermal roll-to-roll processing, (b) Cu nanopillar substrate applied via electroplating, (c) amorphous Si deposited on the Cu nanopillar substrate by low-pressure chemical vapor deposition (LPCVD).

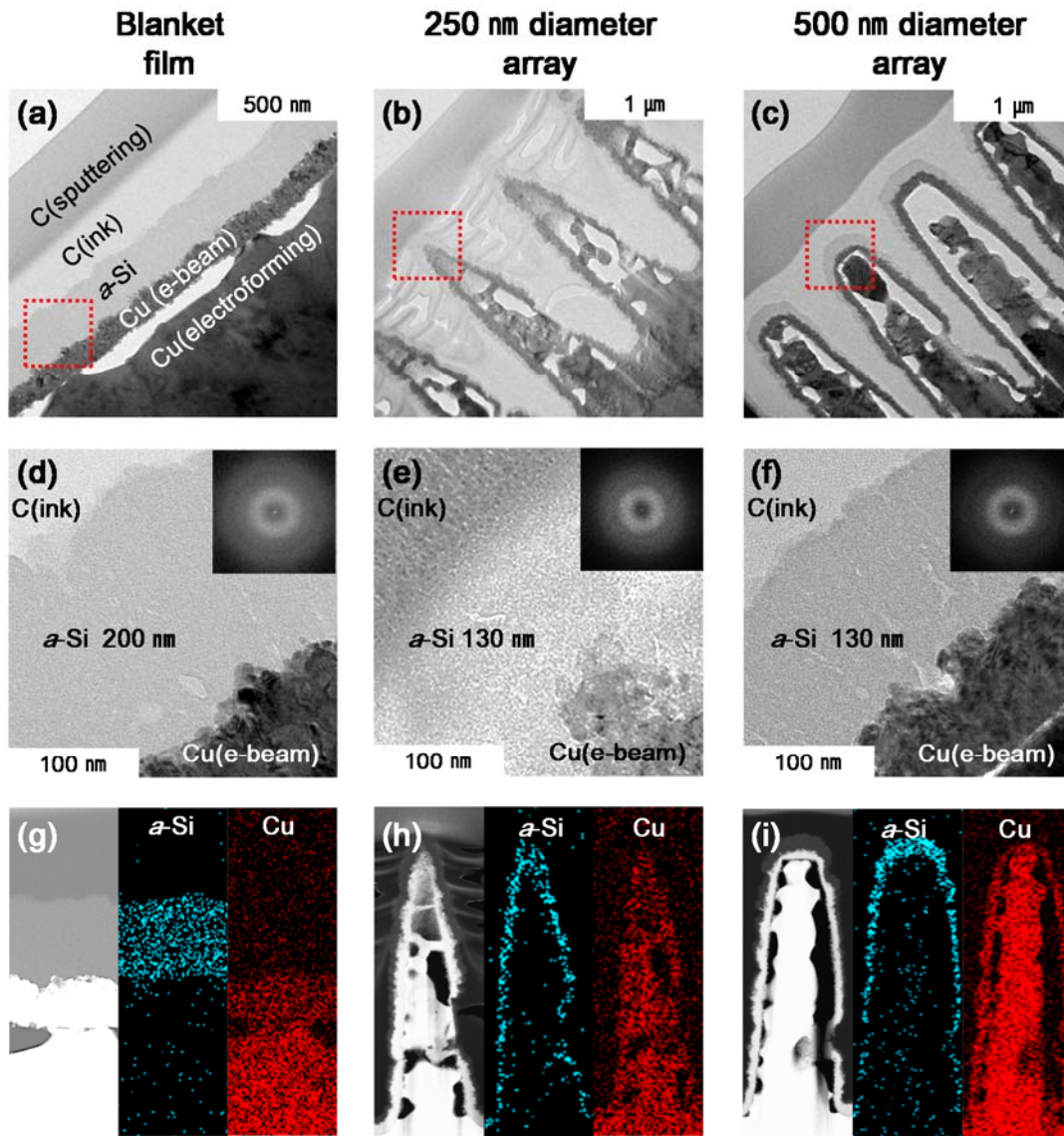


Figure 2. Electrode configuration of 3D amorphous on Si nanopillar Cu electrode by electron microscopy. Cross-sectional TEM images of the overall configuration of the (a) blanket film, (b) *a*-Si/3D-Cu electrode with 250 nm diameter nanopillars, and (c) *a*-Si/3D-Cu electrode with 500 nm diameter nanopillars. (d, e, and f) Expanded views of each structure at the interface between the Cu and *a*-Si layer (rectangular regions in a, b, and c) (inset: FFT analysis for *a*-Si). (g, h, and i) Energy dispersive X-ray (EDX) elemental mapping images of each electrode.

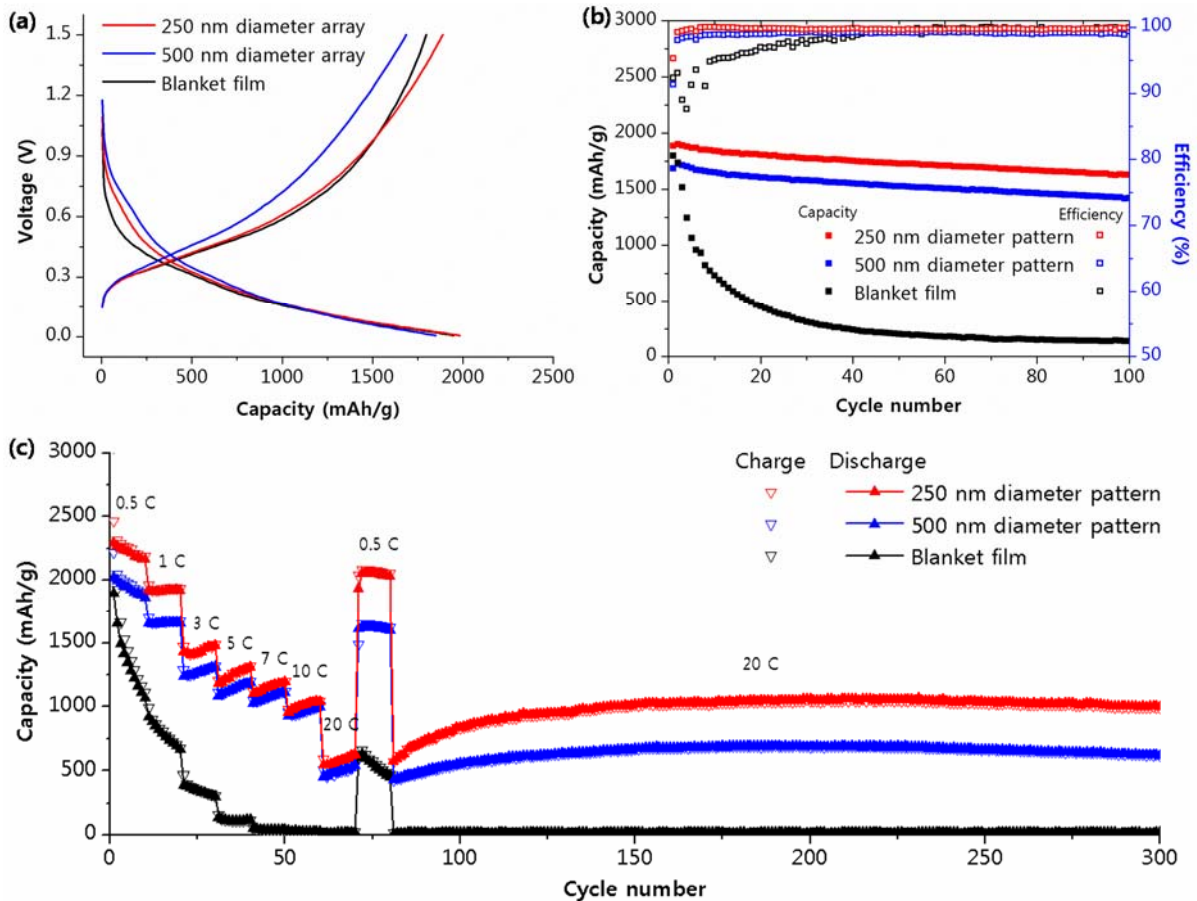


Figure 3. Electrochemical evaluation of 3D amorphous Si on nanopillar Cu electrode. (a) First cycle voltage profiles of the blanket film and *a*-Si/3D-Cu electrodes with 250 and 500 nm diameter nanopillars at 0.5 C rate, and (b) plot of the discharge capacity as a function of cycle number and coulomb efficiency at 0.5 C rate between 0.005 and 1.5 V in a 2032 coin-type half-cell (1 C = 2000 mA/g). (c) Rate capability of the blanket film and both *a*-Si/3D-Cu nanopillar electrodes from 0.5 to 20 C rate between 0.005 and 1.5 V followed by recovery at 0.5 C, and the cycle retention plot at 20 C (the charge and discharge rates were same).

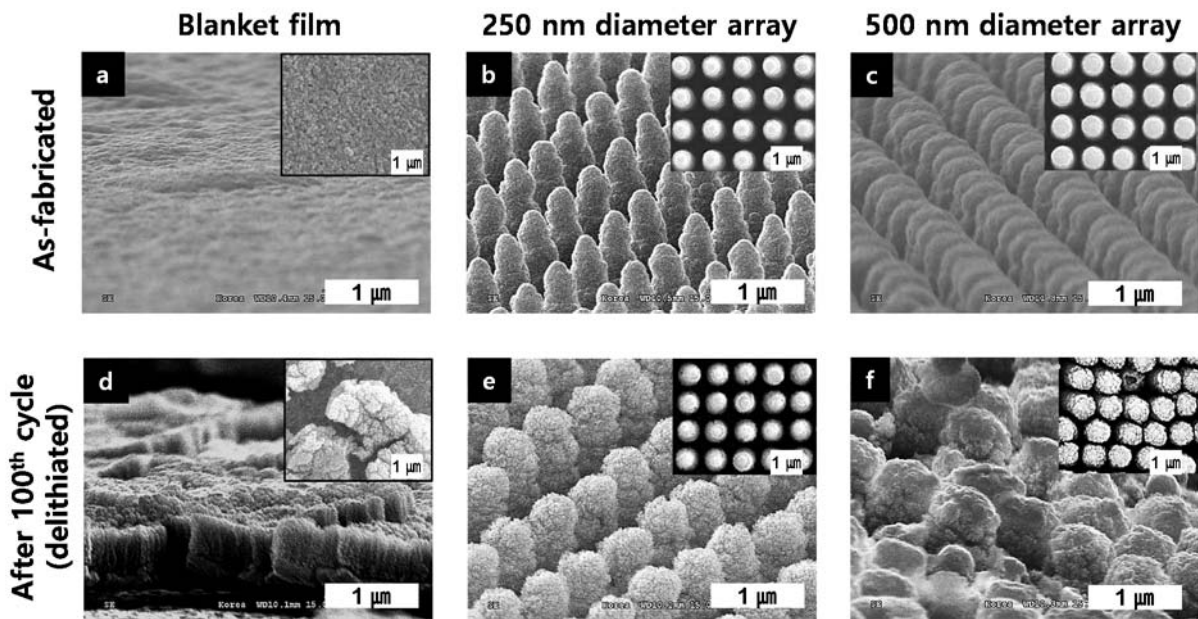


Figure 4. The morphology change before and after electrochemical test. SEM images of the as-fabricated (a) blanket film, (b) *a*-Si/3D-Cu electrode with 250 nm diameter nanopyllars, and (c) *a*-Si/3D-Cu electrode with 500 nm diameter nanopyllars, and (d, e, and f) the blanket film and *a*-Si/3D-Cu electrodes with 250 and 500 nm diameter nanopyllars after 100 cycles, respectively (inset: top view).

Supporting Information

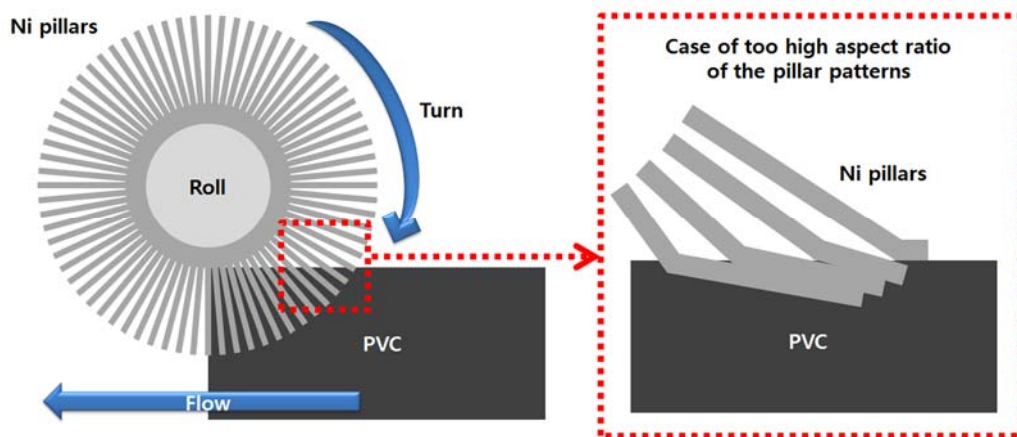


Figure S1. The description of the deformed pattern when Ni pillar stamp has the aspect ratio more than 9.

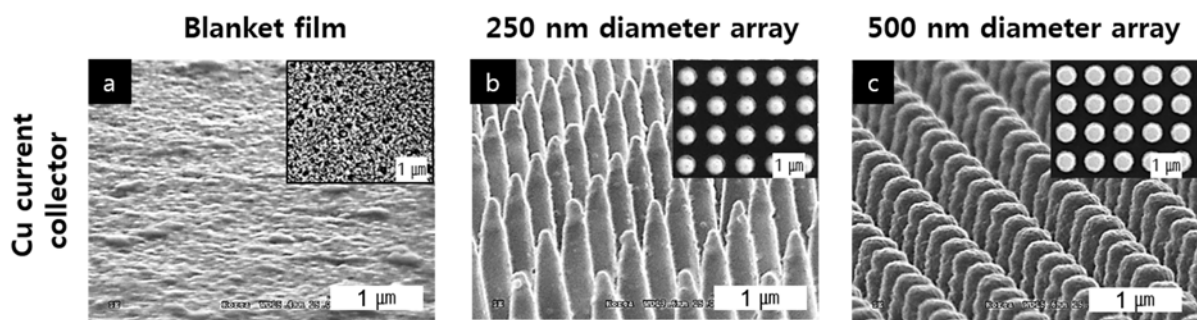


Figure S2. SEM images of (a) blanket film and (b and c) Cu nanopillar electrode with 250 and 500 nm diameter after e-beam evaporation and electroformation, respectively.

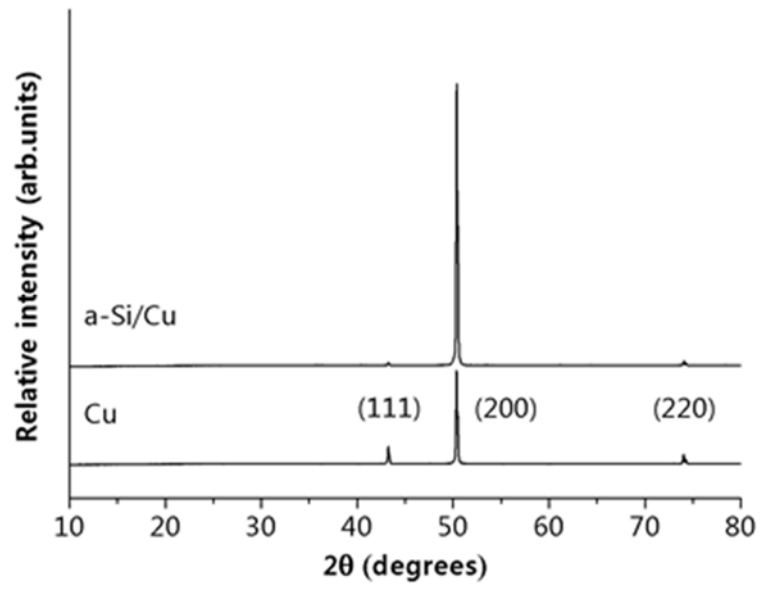


Figure S3. XRD patterns of the blanket film.

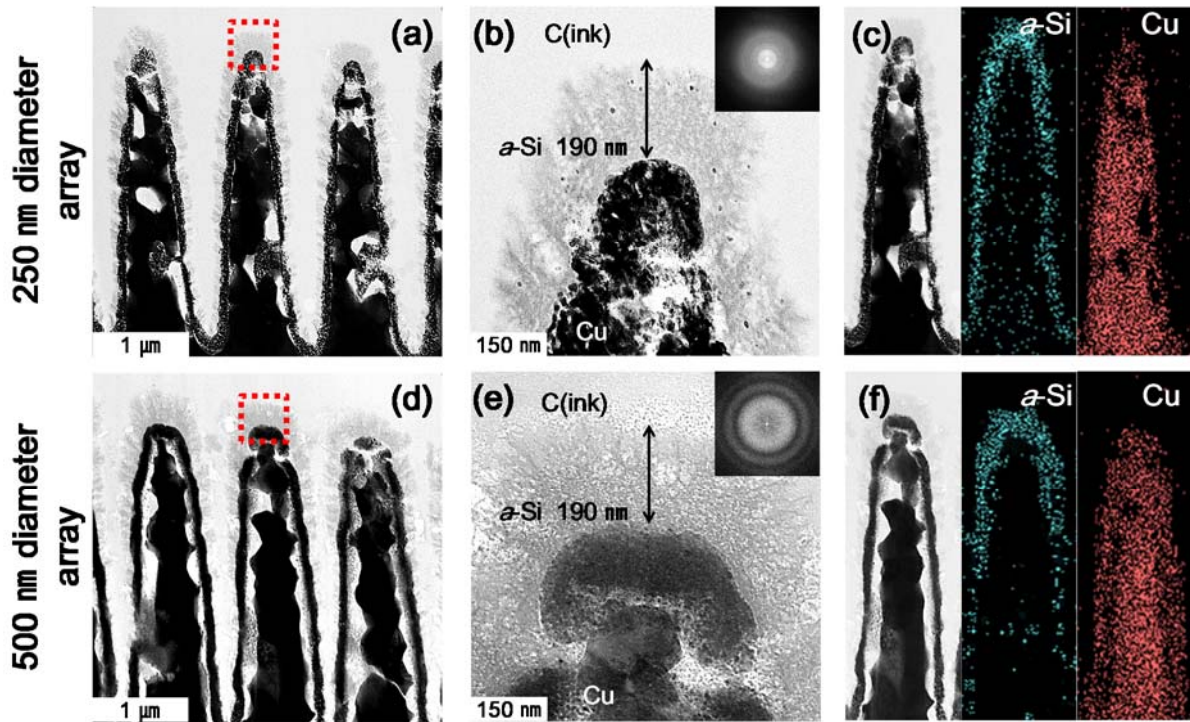


Figure S4. (a and d) Cross-sectional TEM images of the overall configuration of the *a*-Si/3D-Cu electrode with 250 and 500 nm diameter nanopillars after 100 cycles, and (b and e) Expanded views of each structure at the interface between the Cu and *a*-Si layer, respectively (rectangular regions in a and d) (inset: FFT analysis for *a*-Si). (c and f) Energy dispersive X-ray (EDX) elemental mapping images of each electrode.

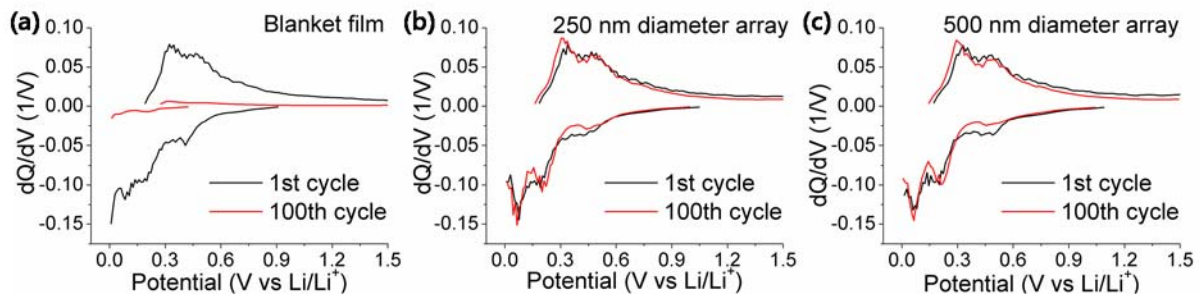


Figure S5. Differential capacity curves of (a) blanket film, (b and c) *a*-Si/3D-Cu electrode with 250 and 500 nm diameter nanopillars for 1st and 100th cycle, respectively.

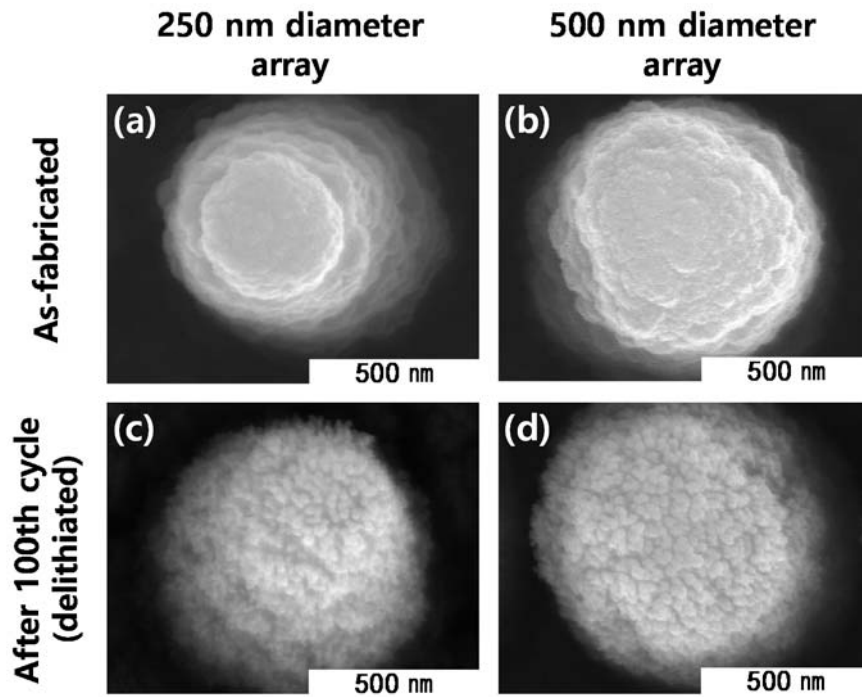


Figure S6. SEM images of the as-fabricated *a*-Si/3D-Cu electrode with 250 and 500 nm diameter nanopillars before (a and b), and after 100 cycles (c and d), respectively.

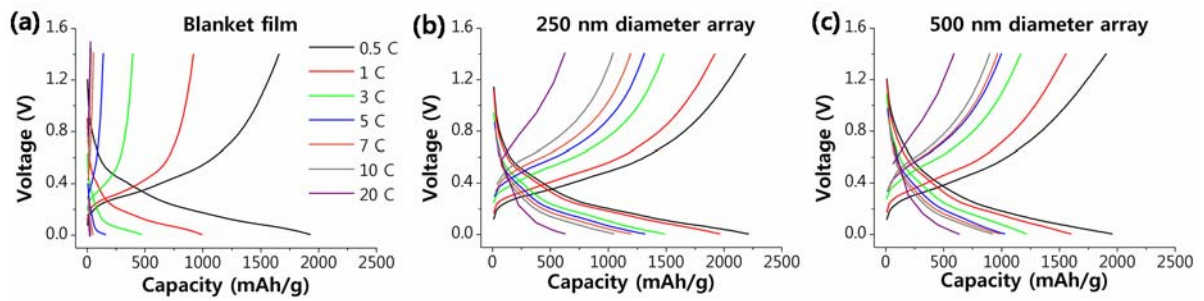


Figure S7. Voltage profiles of (a) blanket film, (b and c) *a*-Si/3D-Cu electrode with 250 and 500 nm diameter nanopillars at various C rates, respectively.

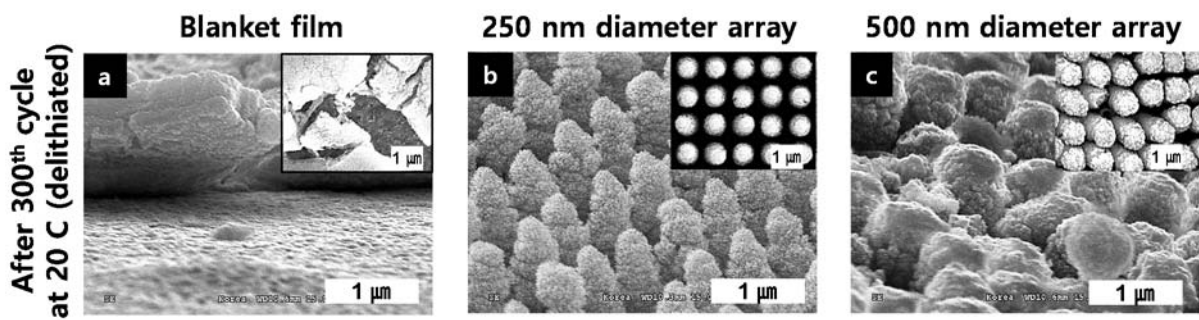


Figure S8. SEM images of the (a) blanket film, *a*-Si/3D-Cu electrode with (b) 250 and (c) 500 nm diameter nanopillars after 300 cycles at 20 C (inset: top view).

References

1. Tarascon, J. M.; Armand, M., Issues and challenges facing rechargeable lithium batteries. *Nature* **2001**, *414* (6861), 359-367.
2. Wang, J.-Z.; Zhong, C.; Chou, S.-L.; Liu, H.-K., Flexible free-standing graphene-silicon composite film for lithium-ion batteries. *Electrochem. Commun.* **2010**, *12* (11), 1467-1470.
3. Chiang, Y.-M., Building a Better Battery. *Science* **2010**, *330* (6010), 1485-1486.
4. Choi, N.-S.; Chen, Z.; Freunberger, S. A.; Ji, X.; Sun, Y.-K.; Amine, K.; Yushin, G.; Nazar, L. F.; Cho, J.; Bruce, P. G., Challenges Facing Lithium Batteries and Electrical Double-Layer Capacitors. *Angew. Chem. Int. Ed.* **2012**, *51* (40), 9994-10024.
5. Nazri, G.-A.; Pistoia, G. *Lithium Batteries: Science and Technology*; Kluwer Academic/Plenum: Boston, **2004**; pp 120-125
6. Huggins, R. A., Lithium alloy negative electrodes. *J. Power Sources* **1999**, *81-82* (0), 13-19.
7. Munao, D.; Valvo, M.; van Erven, J.; Kelder, E. M.; Hassoun, J.; Panero, S., Silicon-based nanocomposite for advanced thin film anodes in lithium-ion batteries. *J. Mater. Chem.* **2012**, *22* (4), 1556-1561.
8. Lee, S. W.; McDowell, M. T.; Choi, J. W.; Cui, Y., Anomalous Shape Changes of Silicon Nanopillars by Electrochemical Lithiation. *Nano Lett.* **2011**, *11* (7), 3034-3039.
9. Liu, X. H.; Zhang, L. Q.; Zhong, L.; Liu, Y.; Zheng, H.; Wang, J. W.; Cho, J.-H.; Dayeh, S. A.; Picraux, S. T.; Sullivan, J. P.; Mao, S. X.; Ye, Z. Z.; Huang, J. Y., Ultrafast Electrochemical Lithiation of Individual Si Nanowire Anodes. *Nano Lett.* **2011**, *11* (6), 2251-2258.
10. Liu, X. H.; Zheng, H.; Zhong, L.; Huang, S.; Karki, K.; Zhang, L. Q.; Liu, Y.; Kushima, A.; Liang, W. T.; Wang, J. W.; Cho, J.-H.; Epstein, E.; Dayeh, S. A.; Picraux, S. T.; Zhu, T.; Li, J.; Sullivan, J. P.; Cumings, J.; Wang, C.; Mao, S. X.; Ye, Z. Z.; Zhang, S.; Huang, J. Y., Anisotropic Swelling and Fracture of Silicon Nanowires during Lithiation. *Nano Lett.* **2011**, *11* (8), 3312-3318.
11. Liu, X. H.; Zhong, L.; Huang, S.; Mao, S. X.; Zhu, T.; Huang, J. Y., Size-Dependent Fracture of Silicon Nanoparticles During Lithiation. *ACS Nano* **2012**, *6* (2), 1522-1531.
12. Kang, B.; Ceder, G., Battery materials for ultrafast charging and discharging. *Nature* **2009**, *458* (7235), 190-193.
13. Chan, C. K.; Peng, H.; Liu, G.; McIlwrath, K.; Zhang, X. F.; Huggins, R. A.; Cui, Y., High-performance lithium battery anodes using silicon nanowires. *Nat. Nanotechnol.* **2008**, *3* (1), 31-35.
14. Cui, L.-F.; Yang, Y.; Hsu, C.-M.; Cui, Y., Carbon-Silicon Core-Shell Nanowires as High Capacity Electrode for Lithium Ion Batteries. *Nano Lett.* **2009**, *9* (9), 3370-3374.

15. Deng, J.; Ji, H.; Yan, C.; Zhang, J.; Si, W.; Baunack, S.; Oswald, S.; Mei, Y.; Schmidt, O. G., Naturally Rolled-Up C/Si/C Trilayer Nanomembranes as Stable Anodes for Lithium-Ion Batteries with Remarkable Cycling Performance. *Angew. Chem. Int. Ed.* **2013**, *52* (8), 2326-2330.
16. Kim, H.; Han, B.; Choo, J.; Cho, J., Three-Dimensional Porous Silicon Particles for Use in High-Performance Lithium Secondary Batteries. *Angew. Chem. Int. Ed.* **2008**, *47* (52), 10151-10154.
17. Kim, H.; Seo, M.; Park, M.-H.; Cho, J., A Critical Size of Silicon Nano-Anodes for Lithium Rechargeable Batteries. *Angew. Chem. Int. Ed.* **2010**, *49* (12), 2146-2149.
18. Liu, N.; Wu, H.; McDowell, M. T.; Yao, Y.; Wang, C.; Cui, Y., A Yolk-Shell Design for Stabilized and Scalable Li-Ion Battery Alloy Anodes. *Nano Lett.* **2012**, *12* (6), 3315-3321.
19. Magasinski, A.; Dixon, P.; Hertzberg, B.; Kvit, A.; Ayala, J.; Yushin, G., High-performance lithium-ion anodes using a hierarchical bottom-up approach. *Nat. Mater.* **2010**, *9* (4), 353-358.
20. Park, M.-H.; Kim, M. G.; Joo, J.; Kim, K.; Kim, J.; Ahn, S.; Cui, Y.; Cho, J., Silicon Nanotube Battery Anodes. *Nano Lett.* **2009**, *9* (11), 3844-3847.
21. Kasavajjula, U.; Wang, C.; Appleby, A. J., Nano- and bulk-silicon-based insertion anodes for lithium-ion secondary cells. *J. Power Sources* **2007**, *163* (2), 1003-1039.
22. Li, H.; Wang, Z.; Chen, L.; Huang, X., Research on Advanced Materials for Li-ion Batteries. *Adv. Mater.* **2009**, *21* (45), 4593-4607.
23. Larcher, D.; Beattie, S.; Morcrette, M.; Edstrom, K.; Jumas, J.-C.; Tarascon, J.-M., Recent findings and prospects in the field of pure metals as negative electrodes for Li-ion batteries. *J. Mater. Chem.* **2007**, *17* (36), 3759-3772.
24. Wu, H.; Zheng, G.; Liu, N.; Carney, T. J.; Yang, Y.; Cui, Y., Engineering Empty Space between Si Nanoparticles for Lithium-Ion Battery Anodes. *Nano Lett.* **2012**, *12* (2), 904-909.
25. Li, H.; Huang, X.; Chen, L.; Wu, Z.; Liang, Y., A High Capacity Nano - Si Composite Anode Material for Lithium Rechargeable Batteries. *Electrochem. Solid-State Lett.* **1999**, *2* (11), 547-549.
26. Li, H.; Huang, X.; Chen, L.; Zhou, G.; Zhang, Z.; Yu, D.; Jun Mo, Y.; Pei, N., The crystal structural evolution of nano-Si anode caused by lithium insertion and extraction at room temperature. *Solid State Ionics* **2000**, *135* (1-4), 181-191.
27. Chou, S.-L.; Wang, J.-Z.; Choucair, M.; Liu, H.-K.; Stride, J. A.; Dou, S.-X., Enhanced reversible lithium storage in a nanosize silicon/graphene composite. *Electrochem. Commun.* **2010**, *12* (2), 303-306.
28. Peng, K.; Jie, J.; Zhang, W.; Lee, S.-T., Silicon nanowires for rechargeable lithium-ion battery anodes. *Appl. Phys. Lett.* **2008**, *93* (3), -.
29. Hertzberg, B.; Alexeev, A.; Yushin, G., Deformations in Si-Li Anodes Upon Electrochemical Alloying in Nano-Confined Space. *J. Am. Chem. Soc.* **2010**, *132* (25), 8548-8549.

30. Takamura, T.; Ohara, S.; Uehara, M.; Suzuki, J.; Sekine, K., A vacuum deposited Si film having a Li extraction capacity over 2000 mAh/g with a long cycle life. *J. Power Sources* **2004**, *129* (1), 96-100.
31. Maranchi, J. P.; Hepp, A. F.; Kumta, P. N., High Capacity, Reversible Silicon Thin-Film Anodes for Lithium-Ion Batteries. *Electrochem. Solid-State Lett.* **2003**, *6* (9), A198-A201.
32. Yu, C.; Li, X.; Ma, T.; Rong, J.; Zhang, R.; Shaffer, J.; An, Y.; Liu, Q.; Wei, B.; Jiang, H., Silicon Thin Films as Anodes for High-Performance Lithium-Ion Batteries with Effective Stress Relaxation. *Adv. Energy Mater.* **2012**, *2* (1), 68-73.
33. Nam, S. H.; Kim, K. S.; Shim, H.-S.; Lee, S. H.; Jung, G. Y.; Kim, W. B., Probing the Lithium Ion Storage Properties of Positively and Negatively Carved Silicon. *Nano Lett.* **2011**, *11* (9), 3656-3662.
34. Gowda, S. R.; Leela Mohana Reddy, A.; Zhan, X.; Jafry, H. R.; Ajayan, P. M., 3D Nanoporous Nanowire Current Collectors for Thin Film Microbatteries. *Nano Lett.* **2012**, *12* (3), 1198-1202.
35. He, Y.; Yu, X.; Wang, Y.; Li, H.; Huang, X., Alumina-Coated Patterned Amorphous Silicon as the Anode for a Lithium-Ion Battery with High Coulombic Efficiency. *Adv. Mater.* **2011**, *23* (42), 4938-4941.
36. Szczech, J. R.; Jin, S., Nanostructured silicon for high capacity lithium battery anodes. *Energy Environ. Sci.* **2011**, *4* (1), 56-72.
37. Cho, J.-H.; Li, X.; Picraux, S. T., The effect of metal silicide formation on silicon nanowire-based lithium-ion battery anode capacity. *J. Power Sources* **2012**, *205* (0), 467-473.
38. Pollak, E.; Salitra, G.; Baranchugov, V.; Aurbach, D., In Situ Conductivity, Impedance Spectroscopy, and Ex Situ Raman Spectra of Amorphous Silicon during the Insertion/Extraction of Lithium. *J. Phys. Chem. C* **2007**, *111* (30), 11437-11444.
39. Charsley, P.; Robins, B. A., Electrical resistance changes of cyclically deformed copper. *Mater. Sci. Eng.* **1974**, *14* (2), 189-196.
40. Cao, F.-F.; Deng, J.-W.; Xin, S.; Ji, H.-X.; Schmidt, O. G.; Wan, L.-J.; Guo, Y.-G., Cu-Si Nanocable Arrays as High-Rate Anode Materials for Lithium-Ion Batteries. *Adv. Mater.* **2011**, *23* (38), 4415-4420.
41. Chang, J.; Huang, X.; Zhou, G.; Cui, S.; Hallac, P. B.; Jiang, J.; Hurley, P. T.; Chen, J., Multilayered Si Nanoparticle/Reduced Graphene Oxide Hybrid as a High-Performance Lithium-Ion Battery Anode. *Adv. Mater.* **2014**, *26* (5), 758-764.
42. Wu, H.; Chan, G.; Choi, J. W.; Ryu, I.; Yao, Y.; McDowell, M. T.; Lee, S. W.; Jackson, A.; Yang, Y.; Hu, L.; Cui, Y., Stable cycling of double-walled silicon nanotube battery anodes through solid-electrolyte interphase control. *Nat. Nanotechnol.* **2012**, *7* (5), 310-315.
43. Nguyen, H. T.; Yao, F.; Zamfir, M. R.; Biswas, C.; So, K. P.; Lee, Y. H.; Kim, S. M.; Cha, S. N.; Kim, J. M.; Pribat, D., Highly Interconnected Si Nanowires for Improved Stability Li-Ion Battery Anodes. *Adv. Energy Mater.* **2011**, *1* (6), 1154-1161.

* Chapter V is reproduced in with a permission of “Kim, G.; Jeong, S.; Shin, J.-H.; Cho, J.; Lee, H., 3D Amorphous Silicon on Nanopillar Copper Electrodes as Anodes for High-Rate Lithium-Ion Batteries. *ACS Nano* 2014, 8 (2), 1907-1912”. Copyright **2014** American Chemical Society.

Chapter VI

Lithium reaction mechanism and high rate capability of VS₄-graphene nanocomposite as an anode material for lithium batteries

1. Introduction

Recently, the number of R & D activities focused on flexible energy storage systems for wearable devices has soared and these storage systems (batteries) require a high capacity and rate performance to allow the devices to operate for a long time and charge in a short amount of time. As one of the leading candidates in flexible batteries, Li-ion batteries (LIBs) have been widely considered. The main challenge to realize these requirements is to design reliable electrodes with flexible properties and a high electrochemical performance. Graphene based composites are very promising in energy storage systems because graphene can offer a large surface area, providing more active sites for electrochemical reactions, and a highly electron conducting network with superior mechanical flexibility.¹ For example, transition metal oxides and sulphides, such as Fe₃O₄,² Co₃O₄,³ MnO₂,⁴ WS₂,⁵⁻⁷ ZrS₂,⁸ and FeS,⁹ have been incorporated into graphene sheets to prepare flexible electrodes. These exhibited a high electrochemical performance due to the graphene that plays a key role in the rapid electron transport and buffering of the volume expansion. Among them, MoS₂, with a sandwich-like layered structure, is the most investigated material owing to its outstanding electrochemical performance and easy synthesis.¹⁰ MoS₂, with different morphologies and sizes, and many kinds of MoS₂ composites, have been employed as anode materials for LIBs, exhibiting a high capacity and good rate capability.¹⁰⁻¹⁷ A comparable energy density (>100 W h kg⁻¹) was also reported for MoS₂ because of its high specific capacity which shows great potential for LIBs.¹⁸

On the other hand, only a few papers have reported studies on utilizing vanadium sulfides and their analogues for LIBs. The intercalation behaviour of Li⁺ into VS₂ was investigated by Murphy et al., and VS₂ was then tested as a cathode material.¹⁹⁻²⁰ Murugan et al. expanded the interlayer spacing of VS₂ by the in situ oxidative polymerization of 3,4-ethylenedioxythiophene (EDOT) and also tested it as a cathode material for LIBs.²¹ VSe_{2-y}S_y and Li_{0.8}VS₂ have been tested as anode materials,²²⁻²³ showing capacities lower than 200 mA h g⁻¹. However, another vanadium sulfide, VS₄, has never been reported for use in lithium storage due to its difficult synthesis method, and only its crystallographic structure has been reported so far.²⁴⁻²⁵ Recently, we succeeded in preparing a VS₄-loaded reduced graphene (rGO) composite via a simple hydrothermal process.²⁵

Herein, we investigate the Li reaction mechanism of the VS₄-reduced graphene (VS₄-rGO) nanocomposite and observe its high rate capability and cycling performance.

2. Experimental section

2.1. Synthesis of VS₄-rGO composites

The synthesis method followed for the VS₄-rGO composites was as reported in ref. 25. Graphene oxide (GO) was prepared from natural graphite powder by a modified Hummers method.²⁵⁻²⁶ To prepare the VS₄-rGO composite, 1.84 g (0.01 mol) of sodium orthovanadate (Na₃VO₄, Sigma-Aldrich, 99.98%) and 3.75 g (0.05 mol) of thioacetamide (C₂H₅NS, Sigma-Aldrich, ≥99%) were dissolved in 320 mL of DI water. Then 80 mL of GO solution (~5 mg mL⁻¹) was added. The mixture was stirred for 1 h at room temperature using a magnetic stirrer. After preparing a homogenous solution, the mixture was transferred to a 500 mL Teflon-lined stainless steel autoclave, tightly sealed and a hydrothermal reaction was carried out at 160 °C for 24 h. After cooling naturally, the product was collected by filtration and washed with DI water and dried under vacuum at 60 °C for 6 h. During the hydrothermal process, VS₄ formed on the GO and GO was transformed into rGO. Furthermore, only rGO was obtained via the hydrothermal reaction of the GO solution under the same conditions however without the addition of Na₃VO₄ and C₂H₅NS. For the synthesis of the reference VS₄-10 wt% CNT composite sample, refer to the supporting information.

2.2. Characterization of the materials

Powder X-ray diffraction (PXRD) patterns were obtained from a High Power X-ray Diffractometer (Rigaku) by using Cu-K α radiation or a Synchrotron Beamline Diffractometer (Pohang Accelerator Lab, Pohang, Korea). All of the samples were sealed in tape before the measurement to prevent oxidation. TEM and EDS mapping images were obtained by using a JEM-2100 transmission electron microscope (JEOL) operated at 200 kV. Mass spectra of the pristine and cycled samples were obtained by using a Bi⁺ beam on a TOF-SIMS spectrometer (ION TOF) at an operating pressure of 5.0×10^{-10} torr. Elemental analysis was performed on a Flash 2000 element analyzer (Thermo Scientific).

2.3. Electrochemical characterization of the materials

The anodes were made of a VS₄-rGO or VS₄-CNT composite, Ketjen Black, and a polyvinylidone fluoride (PVDF) binder (LG Chem.) in a weight ratio of 80:10:10. The coin-type half cells (2016R) were assembled in an Ar-filled glove box, using lithium metal foil as the counter electrode, microporous polyethylene as the separator, and 1.1 M LiPF₆ in ethylene carbonate–diethylene carbonate (EC–DEC, 1:1 volume ratio, Panax Starlyte, Korea) as the electrolyte. The loading amount of the electrode material was measured as >1 mg cm⁻². The coin-type full cell (2032R) was made of a LiMn₂O₄ cathode and a

VS₄-rGO anode with a N/P ratio of 1.1, and 1.1 M LiPF₆ in ethylene carbonate–ethyl methyl carbonate (EC–EMC, 3:7 volume ratio, with a 2% vinylene carbonate additive) was used as the electrolyte. The capacity of the full-cell was ~1 mA h. The cell tests were performed with a WBCS3000 automatic battery cycler system at 23 °C, and the capacity was estimated based only on the active materials (VS₄-rGO in the half-cell, or VS₄-rGO and LiMn₂O₄ in the full-cell). Cyclic voltammetry and electrochemical impedance spectroscopy (EIS) were carried out on an Ivium-n-Stat Multichannel Electrochemical Analyser (Ivium Technologies), using three-electrode cells with lithium metal as the counter and reference electrodes. The cyclic voltammogram (CV) was obtained in the voltage range of 0–3.0 V (vs. Li⁺/Li) at a scan rate of 0.5 mV s⁻¹. The Nyquist plots were recorded by applying an AC voltage with an amplitude of 5 mV in the frequency range of 0.05 Hz to 100 kHz. All electrochemical measurements were carried out at room temperature.

3. Results and discussion

The as-prepared VS₄ phase was confirmed by powder X-ray diffraction, and all the diffraction peaks can be assigned to VS₄ with a body-centered monoclinic phase (I2/c space group, $a = 6.77 \text{ \AA}$, $b = 10.42 \text{ \AA}$, $c = 12.11 \text{ \AA}$, JCPDS card no. 87-0603). VS₄ was described as V⁴⁺(S₂²⁻)₂ (**Figure S1A**). It is a linear-chain compound with alternating bonding and nonbonding contacts between the octa-coordinated vanadium centers with each S₂²⁻ unit bridging two neighboring vanadium atoms (**Figure S1B**).²⁷ No peak for rGO appeared in the XRD pattern, and elemental analysis showed that the content of rGO in this composite was only ~3 wt%. SEM and TEM images confirmed that the composite consists of rGO-attached VS₄ nanorods, with sizes of 200~300 nm in length and 80~150 nm in width (**Figure S2A and B**), which agrees with the previous result.²⁵ The presence of agglomeration is believed to be caused by the interaction between VS₄ and rGO. The HR-TEM image exhibits a typical layered structure, with an interlayer distance of 0.56 nm corresponding to the (110) plane of VS₄ (**Figure. S2C**). EDS mapping images further reveal the homogeneous distribution of vanadium and sulfur in the nanoparticles (**Figure S3**).

Figure 1A shows the representative cyclic voltammograms (CVs) of VS₄-rGO measured in the voltage range of 0–3.0 V (vs. Li⁺/Li) at a scan rate of 0.5 mV s⁻¹ during the first three cycles. Reduction peaks attributed to the lithiation process at ~1.6, ~1.4 and ~0.6 V, and oxidation peaks corresponding to the de-lithiation process at ~1.8 and 2.4 V were observed in the first cycle. Two reduction peaks at ~1.6 and ~1.4 V might be related to the lithium insertion into VS₄ phase (VS₄ → Li_xVS₄), and the peak at ~0.6 V may originate from the decomposition of Li_xVS₄ to Li₂S and elemental V, based on the previous report on MoS₂.¹⁰ The reduction peaks at ~1.6 and ~1.4 V positively shifted, while the peak at ~0.6 V disappeared in the following second and third cycles. **Figure 1B** shows the typical discharge–charge

voltage profiles of the composite within a cut-off voltage window of 0.01–3.0 V at a current rate of 0.05 C ($1\text{ C} = 1000\text{ mA g}^{-1}$) in a coin-type lithium half-cell (2016R) at 23 °C. The initial discharge and charge capacities were 1814 and 1170 mA h g^{-1} , respectively. The low Coulombic efficiency (CE) of 65% may be caused by the irreversible capacity loss, including the inevitable decomposition of the electrolyte and the formation of a solid electrolyte interface (SEI), which is common in transition metal oxides and sulfides based anode materials.^{6, 12-13, 28} The CE was greatly improved after the formation cycle, achieving 94% and 96% during the 2nd and 3rd cycles, with high charge capacities of 1161 and 1153 mA h g^{-1} , respectively. The 1st discharge profile is obviously different from the latter ones. Three potential plateaus at $\sim 1.8\text{ V}$, $\sim 1.6\text{ V}$ and $\sim 0.7\text{ V}$ are observed in the 1st discharge process, but only one potential plateau at $\sim 2.1\text{ V}$ can be seen clearly during the 2nd and 3rd discharge. All of the three charge profiles seem to be similar to each other and two potential plateaus at $\sim 1.8\text{ V}$ and $\sim 2.4\text{ V}$ are observed. Such a variation can be seen more clearly from the differential curves during the first three cycles (**Figure 1C**). The obvious difference between the CV and voltage profiles of the 1st and 2nd discharge processes indicated an irreversible phase transition during the 1st discharge–charge process. A similar phenomenon was found in other transition metal sulfides,^{5, 10, 13, 29} among which the lithium storage mechanism of MoS_2 has been studied recently.³⁰

Figure 2 shows the ex situ XRD patterns of the VS_4 -rGO anodes after discharging or charging to different voltages at 0.1 C. The pristine electrode (**Figure 2a**) showed a consistent XRD pattern with VS_4 -rGO powder. The two main peaks of VS_4 at $\sim 15.8^\circ$ and $\sim 17.0^\circ$ remained at the first voltage plateau during discharge (**Figure 2b and c**). This result is in accordance with the intercalation of 3 Li^+ ions at the first step of discharge (Li_3VS_4). Similar ternary alkali tetrathiovanadates such as $\text{Li}_3\text{VS}_4 \cdot 2\text{DMF}$ (in solution), K_3VS_4 and Na_3VS_4 , have been reported previously.³¹⁻³³ The peak at $\sim 15.8^\circ$ disappeared after discharged to 1.65 V (**Figure 2d**), indicating the decomposition of Li_3VS_4 . The peak at $\sim 17.0^\circ$ also disappeared after being further discharged to 0.5 V (**Figure 2e**) while a new peak, attributed to Li_2S (220), appeared at $\sim 44.8^\circ$. Two weak peaks at $\sim 41.2^\circ$ and $\sim 47.9^\circ$ can be indexed to the (111) and (200) planes of V, respectively. The intensity of the above peaks of Li_2S and V increased after being fully discharged to 0.01 V, and another weak peak of Li_2S (311) at 53.1° appeared (**Figure 2f**). The main peaks of VS_4 did not appear again when finally charged to 3 V (**Figure 2g**), demonstrating the irreversible phase transition during the initial discharge–charge process. The broad peak between 14 and 26° appeared due to the tape.

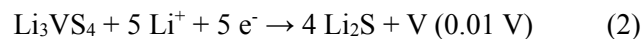
TEM and EDS mapping were adopted to analyse the fully discharged and charged VS_4 -rGO electrodes for further understanding of the mechanism of lithium storage. Two different kinds of particles were seen in the fully discharged electrode (**Figure 3A**), and EDS mapping clearly revealed that elemental V and S were distributed in different particles. The solid and dense particle included only V, which is attributed to nanosized metallic vanadium. The other S-rich particle, with a porous nature,

should be Li_2S , the most common fully discharged product of transition metal sulfides. The HR-TEM image of the fully discharged product also showed d-spacing of 0.333 nm and 0.208 nm, which corresponded to the (111) and (220) planes of Li_2S , respectively (**Figure 3A inset**). The re-formation of VS_4 did not occur after charging to 3 V. The nanosized metallic vanadium still existed in the fully charged VS_4 -rGO electrode (**Figure 3B**), indicating its inert nature during the charge process. The porous Li_2S nanoparticle was converted to sulfur, which was uniformly distributed across the whole area owing to the interaction between rGO and S. The HR-TEM image of the S-rich region showed an amorphous state (**Figure 3B inset**), which is consistent with the absence of sulfur's peaks in the XRD patterns.

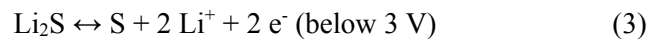
The intrinsic electronic conductivity of the cells could be improved owing to the generation of metallic vanadium during cycling. The electrochemical impedance of the VS_4 -rGO based coin-type lithium cell was measured before and after cycling (**Figure 4A**). The Nyquist plot shows a semicircle with a large diameter at high frequencies before the discharge-charge process, indicating high resistance at the interface. The depressed semicircle with a reduced diameter at high frequencies suggests a decreased impedance after cycling, because of the presence of vanadium metal. A similar result has also been reported in an MoS_2 based electrode.¹³ Time-of-flight secondary ion mass spectrometry (TOF-SIMS) was also employed to analyse the composition of the electrode after discharge and charge. The mass spectra of the pristine electrode show the peaks of VS^+ and VS^{4+} cations (**Figure 4B and C**). However, these peaks disappear after discharging to 0.01 V and charging to 3 V, which also denies the re-formation of VS_4 .

In consequence, we propose a possible lithium storage mechanism of the VS_4 -rGO composite as follows:

An initial discharge:



Followed by



Intercalation of 3 Li^+ ions occurred first in the initial discharge, followed by the decomposition of Li_3VS_4 to Li_2S and V after further discharging to 0.01 V. Then, Li_2S was converted to S after charging to 3 V, while metallic vanadium remained inert. This is quite different from most transition metal oxides, and might be due to the weaker oxidation capability of sulfur than that of oxygen.³⁰ After that, the electrochemical reaction occurred between S and Li_2S during the next cycles. There should be 8 Li^+ ions involved for each VS_4 based on the above mechanism, and a much higher theoretical capacity can

be achieved from VS₄ in comparison to MoS₂ and other transition metal sulfides. The theoretical capacity of VS₄ could be calculated as 1196 mA h g⁻¹, which is very close to the first charge capacity of 1170 mA h g⁻¹ at 0.05 C. On the other hand, the conversion mechanism of VS₄ has not been fully verified owing to the difficulty in characterization, and further studies are still needed to explain it in more detail.

The cycling performance of the VS₄-rGO composite at a high current rate of 4 C (=4 A g⁻¹) between 0.01 and 3.0 V was tested after an initial formation cycle at 0.1 C (**Figure 5**). The composite electrode delivered a high charge capacity of 820 mA h g⁻¹ with a high CE of 96%. The reversible capacity remained at 727 mA h g⁻¹ after 50 cycles, which is 89% of the initial capacity. Such a high capacity-retention of transition metal sulfides or their composites at high current rates is only reported by a few researchers, although good cycling stability was achieved at much lower current densities from MoS₂, ZrS₂, WS₂, etc.^{7-8, 11-12, 15, 34} Furthermore, the CE was maintained at 99% after the 5th cycle. The capacity contribution of rGO was also evaluated, and the specific capacity of rGO was found to be lower than 160 mA h g⁻¹ at the same current rate (**Figure S4**). Therefore, its contribution to the total capacity could be negligible as there was only 3 wt% of rGO in the composite.

To compare the lithium storage capability of VS₄-rGO, VS₄-10 wt% carbon nanotube (VS₄-10CNT) was synthesized (**Figure S5**) and its electrochemical performance was evaluated. The electrochemical performance is highly related to the dispersion of the active materials on the electron conduction matrix. In contrast to VS₄-10CNT (**Figure S2**), CNTs in CNT-VS₄ composites do not provide sufficient coverage of VS₄, resulting in a decrease in the effective electron transport pathway between the VS₄ nanoparticles. It is therefore reasonable to conclude that the rGO-based sample showed a better performance than the CNT-based one. **Figure 6** shows the superior rate capability of the VS₄-rGO composite. VS₄-rGO and VS₄-10CNT delivered a charge capacity of 913 and 733 mA h g⁻¹ at a 2 C rate, respectively, showing a much higher capacity retention for VS₄-rGO than for VS₄-10CNT (also see **Figure S6**). Furthermore, the reversible capacity of VS₄-rGO remained as high as 630 and 314 mA h g⁻¹ when the rate was increased to 10 C (=10 A g⁻¹, or 10 mA cm⁻²) and 20 C (=20 A g⁻¹, or 20 mA cm⁻²), respectively. Such a remarkable high-rate performance is superior to that of most transition metal sulfide based electrodes that have been previously reported.^{7-9, 11-17} These results were induced by the special 2D structure of rGO, providing a large surface area and the strong interaction between the active materials and rGO.³⁵⁻³⁶ In addition, considering its application as an anode material in LIBs, the high charge-discharge voltage plateau (~2.4 V) of VS₄-rGO might be a disadvantage. However, Li₄Ti₅O₁₂ and MoS₂, which also exhibit high voltage plateaus, have been widely reported as anode materials for LIBs. VS₄ delivers a much higher capacity in comparison to Li₄Ti₅O₁₂ (1196 mA h g⁻¹ vs. 175 mA h g⁻¹) although its potential is also higher than that of Li₄Ti₅O₁₂, so a comparable energy density can still be expected for VS₄. In addition, recently there have been many R & D activities focusing on developing anode materials with a high capacity and high rate capability for LIBs in the regenerative break system

of electric vehicles (EVs). For instance, one candidate is a $\text{Li}_4\text{Ti}_5\text{O}_{12}$ anode and a LiFePO_4 cathode with a voltage plateau of <2 V.³⁷⁻³⁸ A $\text{Li}_4\text{Ti}_5\text{O}_{12}$ – LiFePO_4 battery system was also reported for its application in stationary energy storage and smart textiles.³⁹⁻⁴⁰ In this regard, opportunities may still exist to employ VS_4 –rGO as the anode if paired with a high voltage (>4 V) cathode, while considering its high capacity and especially the impressive rate capability.

To prove this point, we carried out a preliminary full-cell test consisting of a LiMn_2O_4 cathode and a VS_4 –rGO anode in a coin-type full-cell (2032R) between 4.3 and 1.0 V at 0.5 C under 23 °C (**Figure 7**). The specific capacity is estimated based on the sole amount of the active material. The first discharge capacity was 72 mA h g^{-1} , and a comparable capacity retention of 74% was achieved after 30 cycles. A better performance could be expected after further optimization of the full-cell configuration.

Such an outstanding electrochemical performance of VS_4 –rGO could be attributed to the following reasons. First, the existence of rGO improved both the conductivity and stability of the VS_4 –rGO electrode, which may cause a better cycling stability and rate capability. Second, although V did not participate in the electrochemical reaction after the initial discharge, the nanosized metallic V enhanced the electronic conductivity of the Li_2S –V or S–V composite during the following discharge–charge process. In addition, the dissolution of polysulfide, which is common in Li-sulfur batteries, could be possibly depressed owing to the absorption effect of the nanosized V with high surface energy.^{13, 30, 41-42}

4. Conclusion

In summary, we have prepared graphene-attached VS_4 nanorods by a simple hydrothermal method. This VS_4 –rGO composite exhibited a good cycling stability and impressive high-rate capability of lithium storage in a half-cell, and the full-cell test has also demonstrated the possibility of using VS_4 –rGO as an anode paired with a high-voltage cathode in LIBs despite its high lithiation voltage. In comparison to other transition metal sulfides, VS_4 is a more promising material for LIBs, owing to its much higher theoretical capacity as well as good cycling stability and excellent high-rate capability. Further studies on VS_4 may accelerate the development of transition metal sulfides for LIBs considering its outstanding performance. In addition, the mechanism of Li storage for VS_4 was also systematically studied for the first time, which would also be very useful in further research on transition metal sulfides for LIBs.

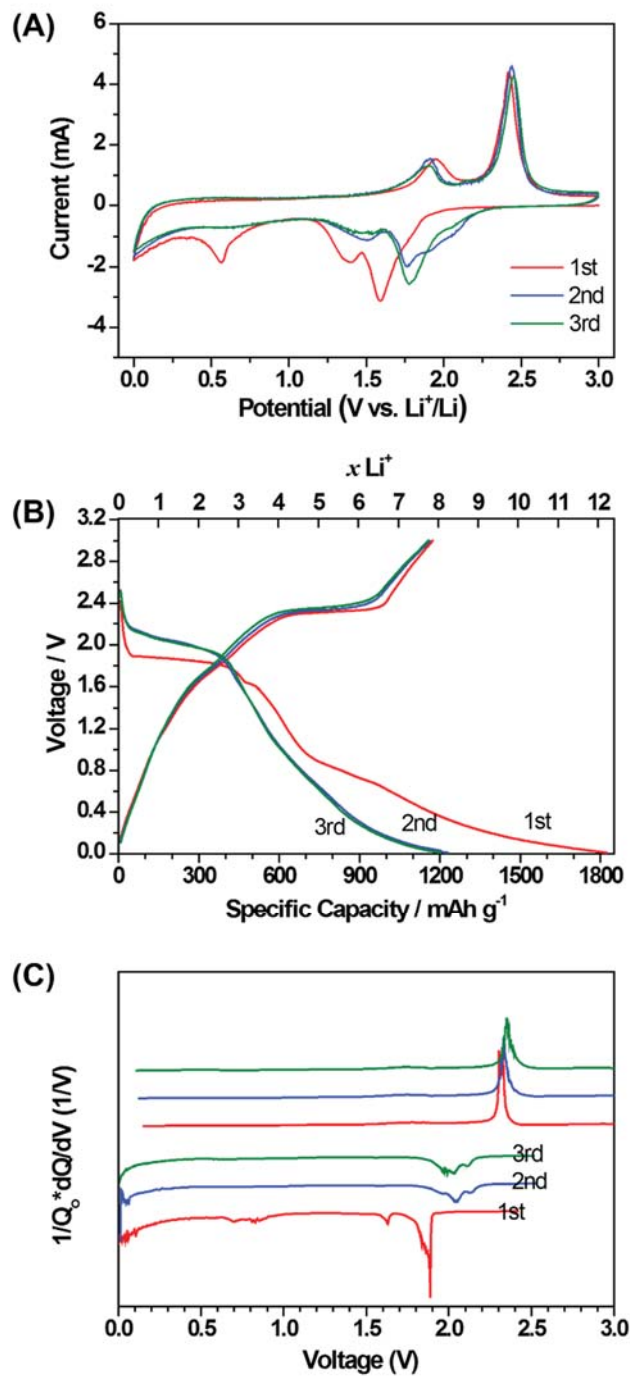


Figure 1. (A) Cyclic voltammogram of VS₄-rGO measured in the voltage range of 0-3.0 V (vs. Li⁺/Li) at a scan rate of 0.5 mV/s during the first three cycles. (B) Discharge-charge voltage profiles of VS₄-rGO at a current rate of 0.05 C in coin-type lithium cell (2016R) at 23 °C (1 C = 1000 mA g⁻¹). (C) Corresponding differential capacity curves during the first three cycles.

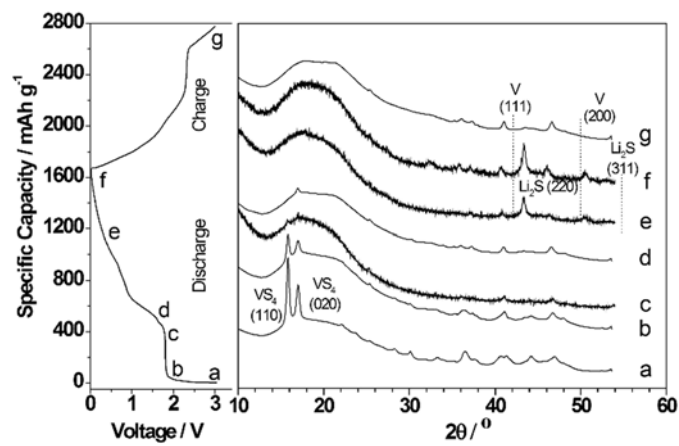


Figure 2. Ex-situ XRD patterns obtained from VS_4 -rGO anodes after discharging or charging to different voltages at 0.1 C: (a) pristine electrode (b-f) discharging to 2.00, 1.80, 1.65, 0.50 and 0.01 V (g) charging to 3 V.

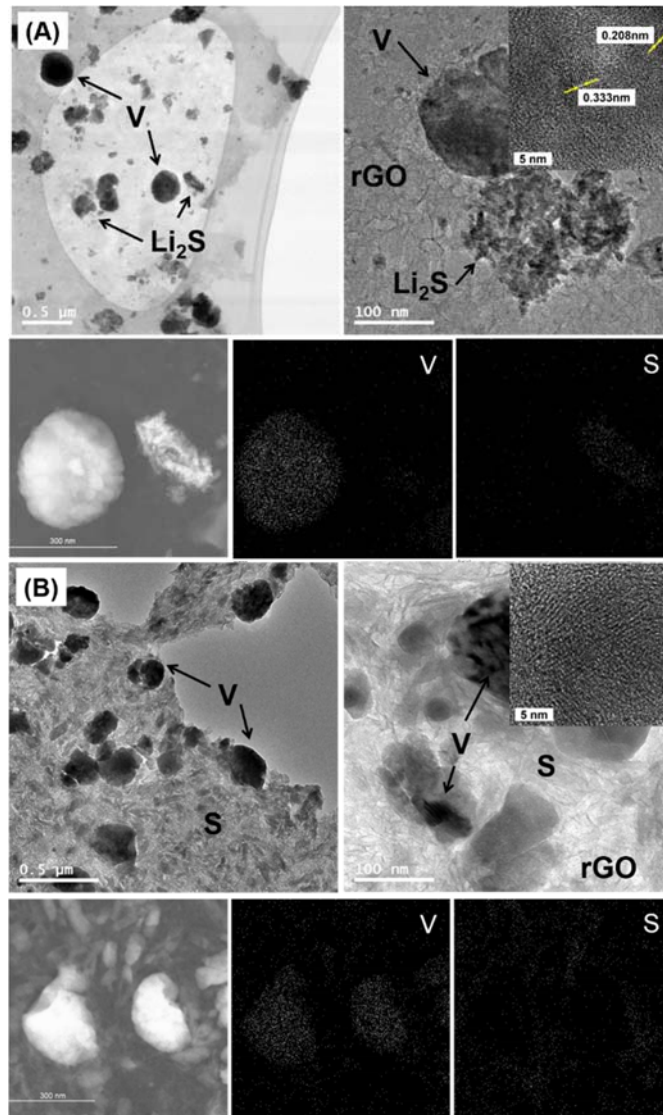


Figure 3. TEM and EDS mapping images of (A) fully discharged electrode (inset: d-spacing of 0.333 and 0.208 nm corresponding to (111) and (220) plane, separately) and (B) fully charged electrode (inset: S-rich regions with amorphous state) of $\text{VS}_4\text{-rGO}$ at 0.1 C ($1\text{ C} = 1000\text{ mA g}^{-1}$).

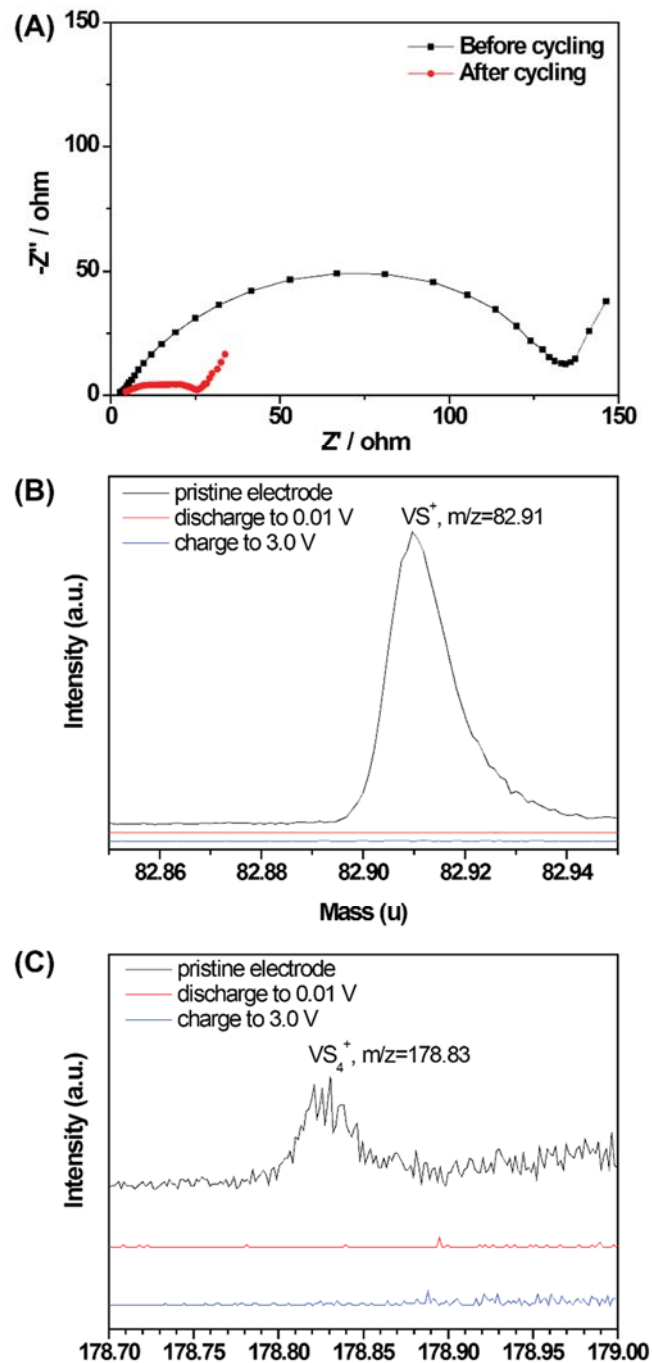


Figure 4. (A) Nyquist plot of VS₄-rGO based coin-type lithium ion cell (2016R) before and cycling. (B and C) TOF-SIMS spectra of VS₄-rGO composite electrode before and after discharge-charge.

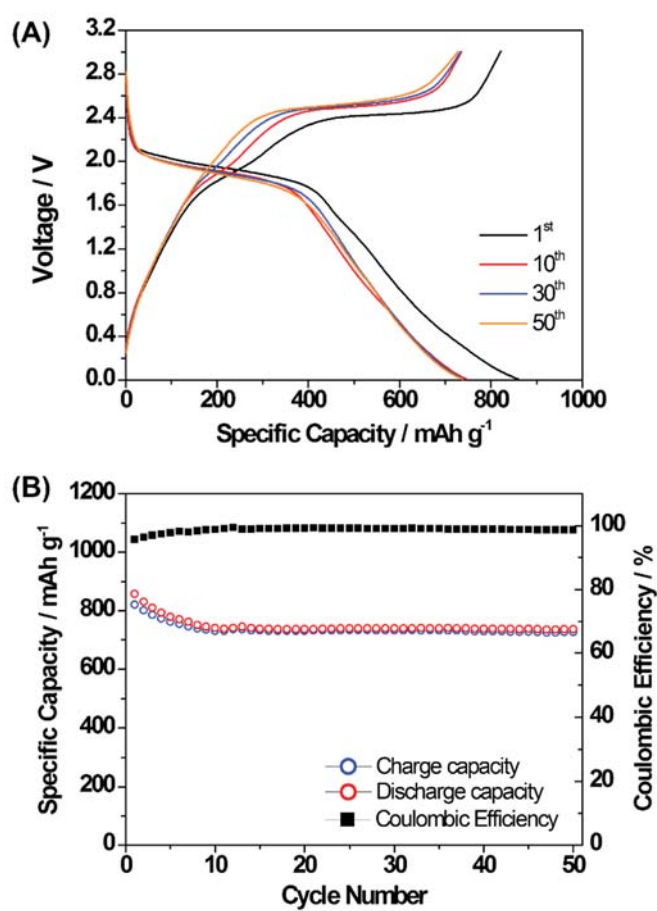


Figure 5. (A) Voltage profiles of VS₄-rGO at a current rate of 4 C in coin-type lithium cell (2016R) at 23 °C. (B) Cycling performance of VS₄-rGO at 4 C (1 C = 1000 mA g⁻¹). An initial formation cycle at a low current rate of 0.1 C was applied before the discharge-charge cycling at 4 C rate.

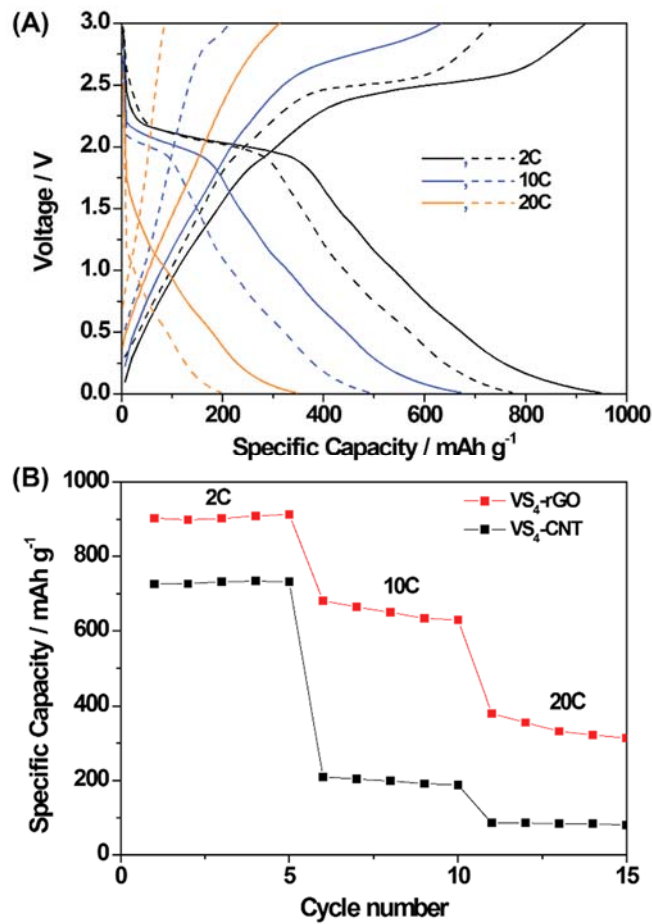


Figure 6. (A) Voltage profiles of VS₄-rGO and VS₄-10 wt% CNT at different current rates in coin-type lithium cell (2016R) at 23 °C (solid line: VS₄-rGO, dash line: VS₄-10 wt% CNT). (B) Rate performance with increasing charge rate from 2 to 20 C. The discharge rate is fixed at 0.1 C (1 C = 1000 mA g⁻¹).

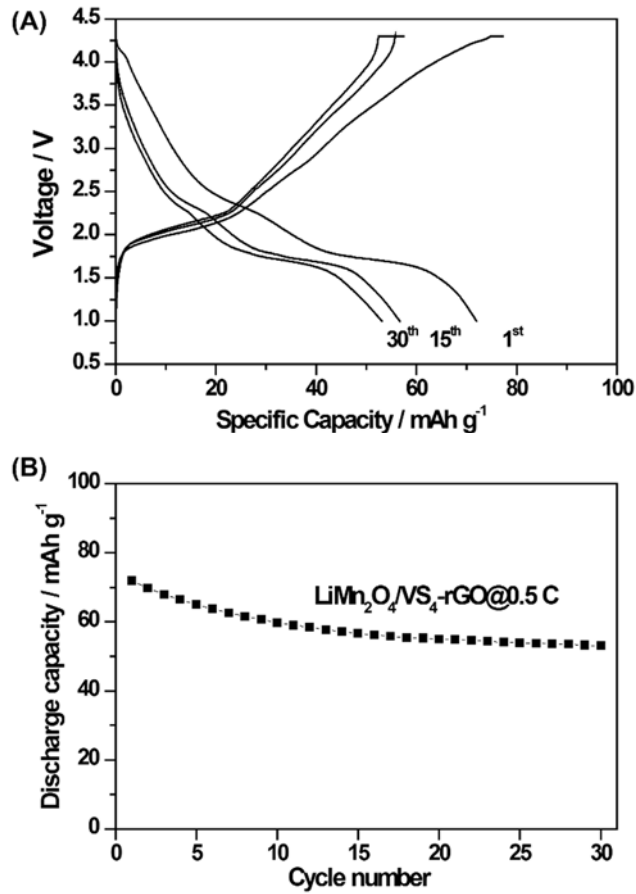


Figure 7. (A) Voltage profiles of LiMn₂O₄/VS₄-rGO in a coin-type full-cell (2032R) between 4.3 and 1.0 V at a rate of 0.5 C after the formation cycle at 0.1 C. (B) Corresponding discharge capacity as a function of cycle number.

Supporting Information

Functionalization of CNT

In the initial step, CNT (Sigma-Aldrich) was treated with a mixture of concentrated sulfuric acid and nitric acid (3:1, 95% and 60%) followed by ultrasonication at 50° C. Further, the product was diluted with water and kept for overnight. The obtained product was filtered and vacuum dried to get the functionalized CNT.

Synthesis of VS₄-10 wt% CNT composite

VS₄-10 wt% CNT composite was prepared by following the same procedure used for the synthesis of VS₄-rGO. At first, functionalized CNT solution (30 mg/mL) was prepared for the hydrothermal synthesis. Na₃VO₄ (0.552 g, 0.003 mol) and C₂H₅NS (1.125 g, 0.015 mol) were dissolved in 115 mL DI water. Then, 5 mL CNT solution was added. The mixture was stirred for 1 h at room temperature, and transferred to a 150 mL Teflon-lined stainless steel autoclave, sealed tightly and kept at 160 °C for 24 h. The carbon content of the as-prepared VS₄-CNT composite was 10 wt% according to elemental analysis.

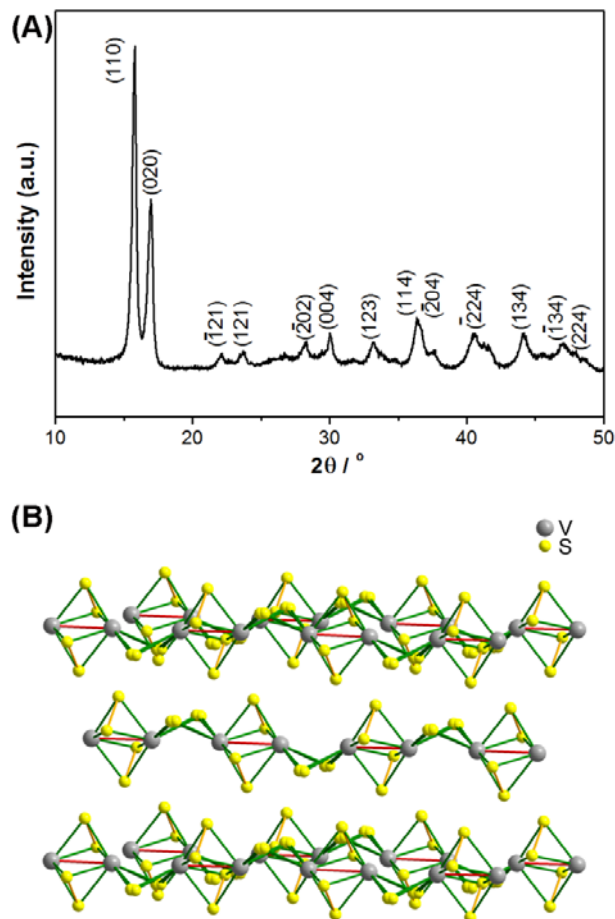


Figure S1. (A) Powder XRD pattern of the as-prepared VS_4 -rGO composite. (B) Structure of linear-chained VS_4 with alternating bonding and nonbonding contacts between the octa-coordinated vanadium centers.

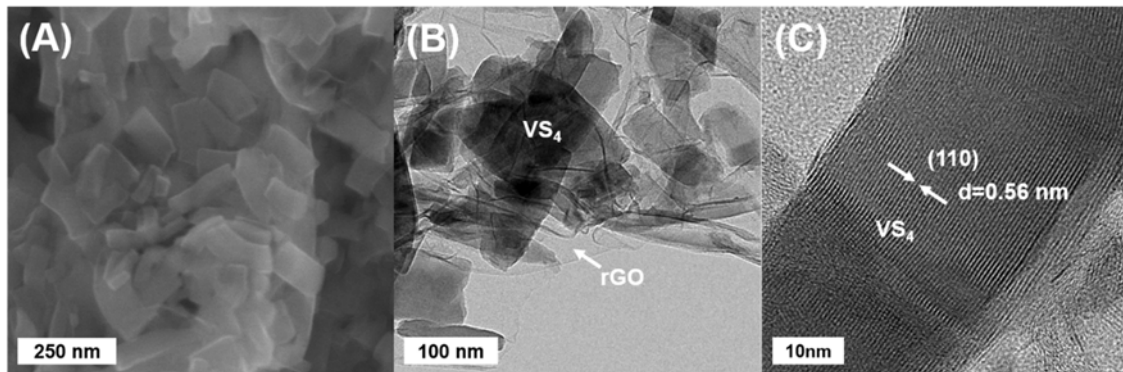


Figure S2. (A) SEM (B) TEM, and (C) HR-TEM of VS_4 in the as-prepared VS_4 -rGO composite.

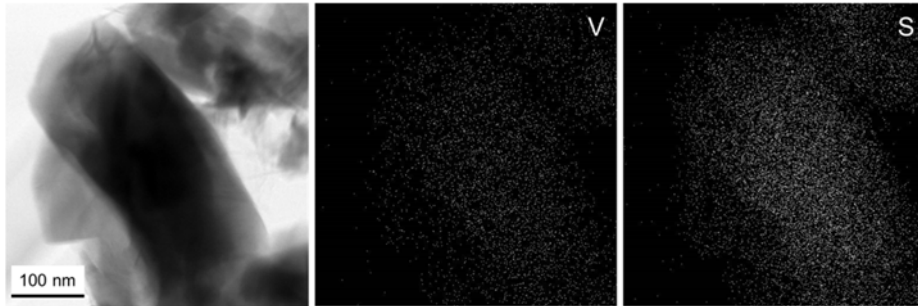


Figure S3. EDS mapping images of the VS₄-rGO composite.

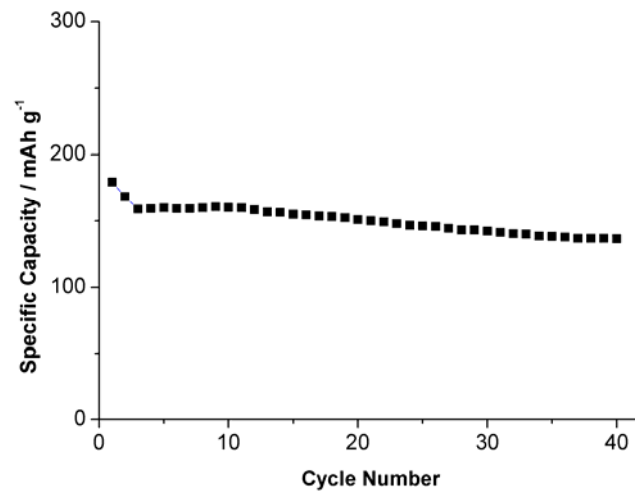


Figure S4. Capacity retention of rGO at a rate of 4 C (1 C=1000 mA g⁻¹).

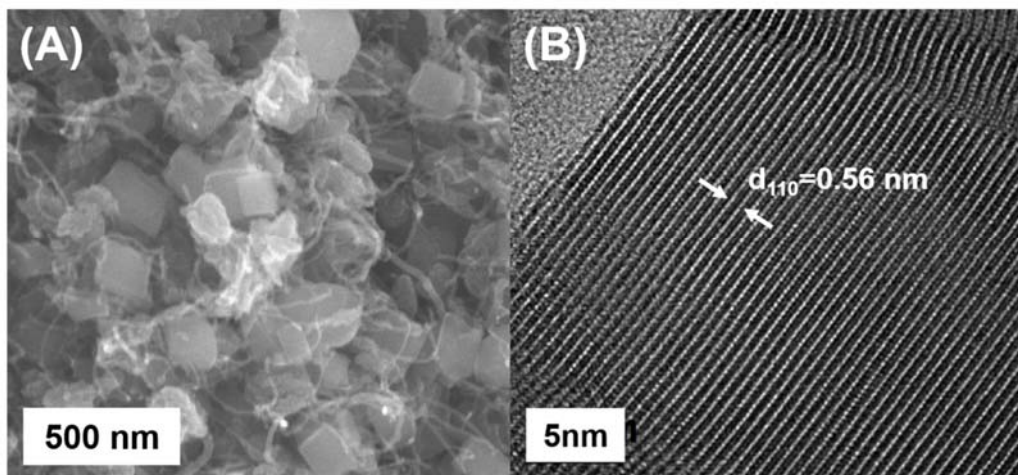


Figure S5. (A) SEM and (B) TEM images of the as-prepared VS₄-10 wt% CNT composites

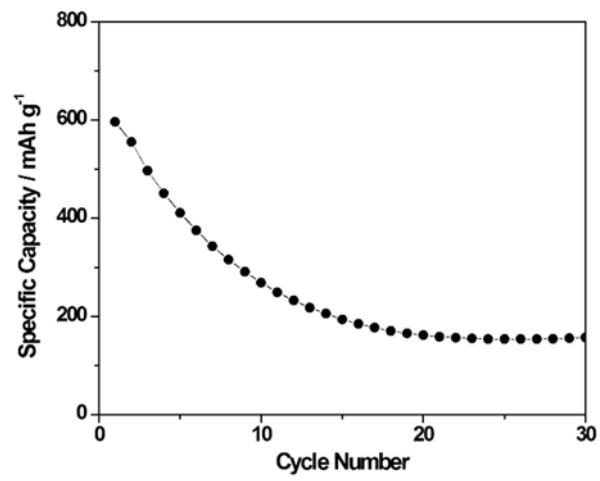


Figure S6. Cycle performance of VS₄-10 wt% CNT composites at 4C and 23 °C

References

1. Zhou, G.; Li, F.; Cheng, H.-M., Progress in flexible lithium batteries and future prospects. *Energy Environ. Sci.* **2014**, 7 (4), 1307-1338.
2. Wang, R.; Xu, C.; Sun, J.; Gao, L.; Lin, C., Flexible free-standing hollow Fe₃O₄/graphene hybrid films for lithium-ion batteries. *J. Mater. Chem. A* **2013**, 1 (5), 1794-1800.
3. Wang, R.; Xu, C.; Sun, J.; Liu, Y.; Gao, L.; Lin, C., Free-standing and binder-free lithium-ion electrodes based on robust layered assembly of graphene and Co₃O₄ nanosheets. *Nanoscale* **2013**, 5 (15), 6960-6967.
4. Yu, A.; Park, H. W.; Davies, A.; Higgins, D. C.; Chen, Z.; Xiao, X., Free-Standing Layer-By-Layer Hybrid Thin Film of Graphene-MnO₂ Nanotube as Anode for Lithium Ion Batteries. *J. Phys. Chem. Lett.* **2011**, 2 (15), 1855-1860.
5. Wang, G. X.; Bewlay, S.; Yao, J.; Liu, H. K.; Dou, S. X., Tungsten Disulfide Nanotubes for Lithium Storage. *Electrochem. Solid-State Lett.* **2004**, 7 (10), A321-A323.
6. Feng, C.; Huang, L.; Guo, Z.; Liu, H., Synthesis of tungsten disulfide (WS₂) nanoflakes for lithium ion battery application. *Electrochem. Commun.* **2007**, 9 (1), 119-122.
7. Liu, H.; Su, D.; Wang, G.; Qiao, S. Z., An ordered mesoporous WS₂ anode material with superior electrochemical performance for lithium ion batteries. *J. Mater. Chem.* **2012**, 22 (34), 17437-17440.
8. Jang, J.-t.; Jeong, S.; Seo, J.-w.; Kim, M.-C.; Sim, E.; Oh, Y.; Nam, S.; Park, B.; Cheon, J., Ultrathin Zirconium Disulfide Nanodiscs. *J. Am. Chem. Soc.* **2011**, 133 (20), 7636-7639.
9. Xu, C.; Zeng, Y.; Rui, X.; Xiao, N.; Zhu, J.; Zhang, W.; Chen, J.; Liu, W.; Tan, H.; Hng, H. H.; Yan, Q., Controlled Soft-Template Synthesis of Ultrathin C@FeS Nanosheets with High-Li-Storage Performance. *ACS Nano* **2012**, 6 (6), 4713-4721.
10. Hwang, H.; Kim, H.; Cho, J., MoS₂ Nanoplates Consisting of Disordered Graphene-like Layers for High Rate Lithium Battery Anode Materials. *Nano Lett.* **2011**, 11 (11), 4826-4830.
11. Du, G.; Guo, Z.; Wang, S.; Zeng, R.; Chen, Z.; Liu, H., Superior stability and high capacity of restacked molybdenum disulfide as anode material for lithium ion batteries. *Chem. Commun.* **2010**, 46 (7), 1106-1108.
12. Chang, K.; Chen, W., l-Cysteine-Assisted Synthesis of Layered MoS₂/Graphene Composites with Excellent Electrochemical Performances for Lithium Ion Batteries. *ACS Nano* **2011**, 5 (6), 4720-4728.
13. Xiao, J.; Wang, X.; Yang, X.-Q.; Xun, S.; Liu, G.; Koech, P. K.; Liu, J.; Lemmon, J. P., Electrochemically Induced High Capacity Displacement Reaction of PEO/MoS₂/Graphene Nanocomposites with Lithium. *Adv. Funct. Mater.* **2011**, 21 (15), 2840-2846.

14. Chang, K.; Chen, W., In situ synthesis of MoS₂/graphene nanosheet composites with extraordinarily high electrochemical performance for lithium ion batteries. *Chem. Commun.* **2011**, 47 (14), 4252-4254.
15. Liu, H.; Su, D.; Zhou, R.; Sun, B.; Wang, G.; Qiao, S. Z., Highly Ordered Mesoporous MoS₂ with Expanded Spacing of the (002) Crystal Plane for Ultrafast Lithium Ion Storage. *Adv. Energy Mater.* **2012**, 2 (8), 970-975.
16. Zhou, X.; Wan, L.-J.; Guo, Y.-G., Facile synthesis of MoS₂@CMK-3 nanocomposite as an improved anode material for lithium-ion batteries. *Nanoscale* **2012**, 4 (19), 5868-5871.
17. Wang, J.-Z.; Lu, L.; Lotya, M.; Coleman, J. N.; Chou, S.-L.; Liu, H.-K.; Minett, A. I.; Chen, J., Development of MoS₂-CNT Composite Thin Film from Layered MoS₂ for Lithium Batteries. *Adv. Energy Mater.* **2013**, 3 (6), 798-805.
18. Dominko, R.; Arčon, D.; Mrzel, A.; Zorko, A.; Cevc, P.; Venturini, P.; Gaberscek, M.; Remskar, M.; Mihailovic, D., Dichalcogenide Nanotube Electrodes for Li-Ion Batteries. *Adv. Mater.* **2002**, 14 (21), 1531-1534.
19. Murphy, D. W.; Carides, J. N.; Di Salvo, F. J.; Cros, C.; Waszczak, J. V., Cathodes for nonaqueous lithium batteries based on VS₂. *Mater. Res. Bull.* **1977**, 12 (8), 825-830.
20. Murphy, D. W.; Di Salvo, F. J.; Carides, J. N., Vanadium disulfide: Metal substitution and lithium intercalation. *J. Solid State Chem.* **1979**, 29 (3), 339-343.
21. Vadivel Murugan, A.; Quintin, M.; Delville, M.-H.; Campet, G.; Vijayamohanan, K., Entrapment of poly(3,4-ethylenedioxythiophene) between VS₂ layers to form a new organic-inorganic intercalative nanocomposite. *J. Mater. Chem.* **2005**, 15 (8), 902-909.
22. Guzman, R.; Lavela, P.; Morales, J.; Tirado, J. L., VSe_{2-y}S_y electrodes in lithium and lithium-ion cells. *J. Appl. Electrochem.* **1997**, 27 (10), 1207-1211.
23. Kim, Y.; Park, K.-s.; Song, S.-h.; Han, J.; Goodenough, J. B., Access to M³⁺ / M²⁺ Redox Couples in Layered LiMS₂ Sulfides (M = Ti, V, Cr) as Anodes for Li-Ion Battery. *J. Electrochem. Soc.* **2009**, 156 (8), A703-A708.
24. Pedersen, B., Unit Cell and Space Group of VS₄. *Acta Chem Scand* **1959**, 13, 1050.
25. Rout, C. S.; Kim, B.-H.; Xu, X.; Yang, J.; Jeong, H. Y.; Odkhuu, D.; Park, N.; Cho, J.; Shin, H. S., Synthesis and Characterization of Patronite Form of Vanadium Sulfide on Graphitic Layer. *J. Am. Chem. Soc.* **2013**, 135 (23), 8720-8725.
26. Kovtyukhova, N. I.; Ollivier, P. J.; Martin, B. R.; Mallouk, T. E.; Chizhik, S. A.; Buzaneva, E. V.; Gorchinskiy, A. D., Layer-by-Layer Assembly of Ultrathin Composite Films from Micron-Sized Graphite Oxide Sheets and Polycations. *Chem. Mater.* **1999**, 11 (3), 771-778.
27. Hibble, S. J.; Walton, R. I.; Pickup, D. M., Local structures of the amorphous chromium sulfide, CrS₃, and selenide, CrSe₃, from X-ray absorption studies. *J. Chem. Soc., Dalton Trans.* **1996**, (11), 2245-2251.

28. Cabana, J.; Monconduit, L.; Larcher, D.; Palacín, M. R., Beyond Intercalation-Based Li-Ion Batteries: The State of the Art and Challenges of Electrode Materials Reacting Through Conversion Reactions. *Adv. Mater.* **2010**, *22* (35), E170-E192.
29. Xiao, J.; Choi, D.; Cosimbescu, L.; Koech, P.; Liu, J.; Lemmon, J. P., Exfoliated MoS₂ Nanocomposite as an Anode Material for Lithium Ion Batteries. *Chem. Mater.* **2010**, *22* (16), 4522-4524.
30. Fang, X.; Guo, X.; Mao, Y.; Hua, C.; Shen, L.; Hu, Y.; Wang, Z.; Wu, F.; Chen, L., Mechanism of Lithium Storage in MoS₂ and the Feasibility of Using Li₂S/Mo Nanocomposites as Cathode Materials for Lithium–Sulfur Batteries. *Chem. – Asian J.* **2012**, *7* (5), 1013-1017.
31. Zhang, Y. P.; Holm, R. H., Li₃[VS₄]·2DMF: a solubilized form of tetrathiovanadate(V). *Inorg. Chem.* **1988**, *27* (21), 3875-3876.
32. Bensch, P. D. a. W., Synthesis and crystal structures of K₂CuVS₄ and K₃VS₄: First examples of ternary and quaternary vanadium sulfides prepared via the molten flux method. *Eur. J. Solid State Inorg. Chem.* **1996**, *33*, 309.
33. Gabl, K. O. K. a. G., *Eur. J. Solid State Inorg. Chem.* **1997**, *34*, 1143.
34. Chang, K.; Chen, W., Single-layer MoS₂/graphene dispersed in amorphous carbon: towards high electrochemical performances in rechargeable lithium ion batteries. *J. Mater. Chem.* **2011**, *21* (43), 17175-17184.
35. Wang, H.; Liang, Y.; Gong, M.; Li, Y.; Chang, W.; Mefford, T.; Zhou, J.; Wang, J.; Regier, T.; Wei, F.; Dai, H., An ultrafast nickel–iron battery from strongly coupled inorganic nanoparticle/nanocarbon hybrid materials. *Nat. Commun.* **2012**, *3*, 917.
36. Xin, S.; Guo, Y.-G.; Wan, L.-J., Nanocarbon Networks for Advanced Rechargeable Lithium Batteries. *Acc. Chem. Res.* **2012**, *45* (10), 1759-1769.
37. LG Chem. & Samsung SDI, and Hyundai Motors, private communications.
38. Jaiswal, A.; Horne, C. R.; Chang, O.; Zhang, W.; Kong, W.; Wang, E.; Chern, T.; Doeff, M. M., Nanoscale LiFePO₄ and Li₄Ti₅O₁₂ for High Rate Li-Ion Batteries. *J. Electrochem. Soc.* **2009**, *156* (12), A1041-A1046.
39. Wang, W.; Choi, D.; Yang, Z., Li-Ion Battery with LiFePO₄ Cathode and Li₄Ti₅O₁₂ Anode for Stationary Energy Storage. *Metall. Mater. Trans. A* **2013**, *44* (1), 21-25.
40. Liu, Y.; Gorgutsa, S.; Santato, C.; Skorobogatiy, M., Flexible, Solid Electrolyte-Based Lithium Battery Composed of LiFePO₄ Cathode and Li₄Ti₅O₁₂ Anode for Applications in Smart Textiles. *J. Electrochem. Soc.* **2012**, *159* (4), A349-A356.
41. Schuster, J.; He, G.; Mandlmeier, B.; Yim, T.; Lee, K. T.; Bein, T.; Nazar, L. F., Spherical Ordered Mesoporous Carbon Nanoparticles with High Porosity for Lithium–Sulfur Batteries. *Angew. Chem. Int. Ed.* **2012**, *51* (15), 3591-3595.

42. Evers, S.; Nazar, L. F., New Approaches for High Energy Density Lithium–Sulfur Battery Cathodes. *Acc. Chem. Res.* **2012**, *46* (5), 1135-1143.

* Chapter VI is reproduced in with a permission of “Xu, X.; Jeong, S.; Rout, C. S.; Oh, P.; Ko, M.; Kim, H.; Kim, M. G.; Cao, R.; Shin, H. S.; Cho, J., Lithium reaction mechanism and high rate capability of VS₄-graphene nanocomposite as an anode material for lithium batteries. *Journal of Materials Chemistry A* 2014”. Copyright **2014** The Royal Society of Chemistry

Acknowledgment

Chapter I:

This research was supported by MSIP (Ministry of Science, ICT&Future Planning), Korea, under the C-ITRC (Convergence Information Technology Research Center) support program (NIPA-2013-H0301-13-1009) supervised by the NIPA (National IT Industry Promotion Agency). Also, Finaical was supported from the BK21 Plus funded by the Ministry of Education, Korea (10Z20130011057) is greatly acknowledged.

Chapter III:

This work was supported by the Converging Research Center Program through the Ministry of Education, Science and Technology of South Korea (2010K000984).

Chapter IV:

This work was supported by the Converging Research Center Program through the Ministry of Education, Science and Technology (2012K001251) in Korea.

Chapter V:

This research was supported by the Pioneer Research Center Program through the National Research Foundation of Korea funded by the Ministry of Science, ICT & Future Planning (NRF-2013M3C1A3063597), by Nano-Material Technology Development Program through the National Research Foundation of Korea (NRF) funded by the Ministry of Education, Science and Technology (2012M3A7B4035323), and by Basic Science Research Program through the National Research Foundation of Korea funded by the Ministry of Education, Science and Technology (NRF-2012-0002363). Also, the Converging Research Center Program through the Ministry of Science, ICT, and Future Planning, Korea (2013K000210), is greatly acknowledged.

Chapter VI:

This work was supported by the Converging Research Center Program (2013K000210) and Center for Advanced Soft Electronics (Code no. 2011-0031630) under the Global Frontier Research Program through the National Research Foundation funded by MEST of Korea.

